2013-09-16

Low-Cost Sensors-Based Attitude Estimation for Pedestrian Navigation in GPS-Denied Environments

Ali, Abdelrahman

UNIVERSITY OF CALGARY

Low-Cost Sensors-Based Attitude Estimation for Pedestrian Navigation in GPS-Denied

Environments

by

Abdelrahman Saad Abdelrahman Ali

A THESIS

SUBMITTED TO THE FACULTY OF GRADUATE STUDIES

IN PARTIAL FULFILMENT OF THE REQUIREMENTS FOR THE

DEGREE OF DOCTOR OF PHILOSOPHY

DEPARTMENT OF GEOMATICS ENGINEERING

and

DEPARTMENT OF ELECTRICAL AND COMPUTER ENGINEERING

CALGARY, ALBERTA

SEPTEMBER, 2013

Abstract

Pedestrian navigation has received significant attention in the last few years due to potential development in the smartphones' technologies. Todays, most smartphones, tablets, and other handheld devices are fully packed with the required sensors that can provide navigation information such as Global Positioning System (GPS), triad gyroscope, triad accelerometer, triad magnetometer, and pressure sensors. The pedestrian dead-reckoning (PDR) technique requires traveled distance and direction in order to estimate the user position. Total distance can be determined using the step counting and step length estimation techniques using accelerometer data while, the relative attitude information can be estimated using gyroscope and accelerometer data. However, absolute heading information is required which can be provided using GPS or magnetometer.

In GPS-denied environments, a magnetometer is used as the main source of heading update. However, the EMF is experienced to severe degradation in such environments which affects the overall performance of the magnetometer. Different techniques are proposed to overcome the deficiency due to the distortion in the sensed magnetic field to improve the overall performance of the magnetometer in the cluttered environments. For that end, this research is targeted towards improving the attitude estimation for pedestrian navigation in the harsh environments by developing sensor fusion technique to utilize the gyroscope rate in complementary with accelerometer and magnetometer data. Also, several contributions for step detection and step length estimation techniques are achieved to improve the overall performance and accuracy of the Pedestrian Dead Reckoning (PDR) algorithm.

Acknowledgements

Dedication

To my parents and Beloved Family

My Lovely Wife, My Son, and My Daughter

(Thank You So Much)

List of Tables

List of Figures and Illustrations

List of Symbols, Abbreviations and Nomenclature

Symbol	Definition
q	Quaternion
Ψ	Heading or azimuth
φ	Latitude
λ	Longitude
θ	Pitch angle
ϕ	Roll angle
k	Time index (epoch)
$R(t)$	Measurement noise covariance
D	Declination angle
R	Rotation matrix
B	Raw Magnetic field
b	Sensor bias
A	Scale Factor Matrix, Acceleration Norm
g	Acceleration due to gravity
T	Tesla
H	Horizontal field
Z	Vertical field
I	Inclination angle
F	Magnetic field intensity
x_k	State vector
z_k	Measurement vector
$F(t)$	Dynamics matrix
$G(t)$	Shaping matrix
$H(t)$	Design matrix
$w(t)$	System noise
$v(t)$	Measurement noise
$\Phi_{k,k+1}$	State transition matrix
Q_k	Process noise covariance matrix

P_k	State covariance matrix
R_k	Measurement covariance matrix
K_k	Kalman gain
C_a^b	DCM from a frame to b frame
ω	Angular velocity vector
f	Acceleration vector
σ^2	Variance
τ_c	Correlation time
a	Semi-major axis of the reference ellipsoid
e	Linear eccentricity of the reference ellipsoid
h	Ellipsoidal height
R_M	Radius of curvature in meridian
R_N	Radius of curvature in prime vertical
x	x-axis
y	y-axis
z	z-axis
ε	Noise vector

Abbreviation	Definition
2D	Two Dimensional
3D	Three Dimensional
ABI	Allied Business Intelligence, Inc.
ACO	Anti-Colony Optimization
AI	Artificial Intelligence
AMR	Anisotropic Magneto Resistive
ANN	Artificial Neural Network
AV	Allan Variance
AWGN	Additive White Gaussian Noise
b-frame	Body Frame
CUPT	Coordinate Update
DCM	Direction Cosine Matrix
DMMs	Different Manoeuvring Modes
DR	Dead Reckoning
e-frame	Earth Center Earth Fixed frame
EMF	Earth's Magnetic Field
LKF	Linearized Kalman Filter
GA	Genetic Algorithms
GNSS	Global Navigation Satellite System
GPS	Global Positioning System
h-frame	Horizontal Level Frame
IAGA	International Association Geomagnetism and Aeronomy
i-frame	inertial frame
IGRF	International Geomagnetic Reference Field
IMU	Inertial Measurement Unit
INS	Inertial Navigation System
KF	Kalman Filter
KBS	Knowledge Based Systems
LBS	Location Based Services
l-frame	Local Level Frame

MEMS	Micro Electro Mechanical System
MM	Manoeuvring Mode
MPSOT	Modified PSO Technique
Navaid	Navigation aid
NED	North East Down
PDR	Pedestrian Dead Reckoning
PND	Portable Navigation Devices
PNS	Pedestrian Navigation System
POS/NAV	Positioning/Navigation
PSO	Particle Swarm Optimization
RF	Radio Frequency
RFID	Radio Frequency Identification
RIST	Region of Interest Selection Technique
SF	Scale Factor
s-frame	Sensor Frame
SI	Swarm Intelligence
SL	Step Length
SNR	Signal to Noise Ratio
UWB	Ultra-Wide Band
Wi-Fi	Wireless Fidelity
ZUPT	Zero Velocity Updates

Chapter One: Introduction

1.1 Navigation

Navigation is the art of determining the time varying positions, velocities and attitudes of a moving body. Nowadays, navigation technologies are expanding at a phenomenal rate, especially in the civilian community, with devices such as vehicle/personal navigators, smartphones, tablets, and other handheld devices. Navigation is achieved on these devices by integrating the output of a group of sensors to compute the necessary navigational information. A sensor that can measure one or more of the navigation states is referred to as a "navigation sensor" while the combination of all these sensors that can provide all of the navigation states is a "navigation system" (Syed 2009). However, a Navigation Aid is a sensor that can only provide indirect partial information and can be used as a constraint for some of the navigation states (Navaid) (El-Sheimy 2012). Positions, velocities and attitudes are called navigation states since they contain all the information required to geo-reference a rigid body at a specific moment in time.

Nowadays, GPS is the most widely used navigation system. It is available almost everywhere in the world: in air (aircraft navigation), sea (ship navigation) or land (vehicle navigation). However, with the growing demand for solutions in harsh GPS environments, such as in downtown areas, under heavily treed canopies, or in the presence of jamming, the limits of GPS signal availability are being reached. In other words, the system does not work well in urban areas due to signal blockage and/or attenuation which may deteriorate the positioning accuracy.

Inertial Navigation Systems (INS) can help provide a continuous navigation solution for harsh GPS environments. Inertia sensors are self-contained and provide the position, velocity, and attitude of a moving body by measuring its acceleration and rotation angle. However, when an inertial sensor's gyroscope and accelerometer outputs drift over time it means that standalone inertial based navigation systems have an upper bound for accuracy. Thus, various aiding sensors have been tied into inertial systems, such as GPS, velocity meters (odometer), geomagnetic sensors (magnetometer), etc. Figure 1.1 shows the error propagation of the INS standalone technique where the positional error drifts and accumulates over time in the absence of any update source.
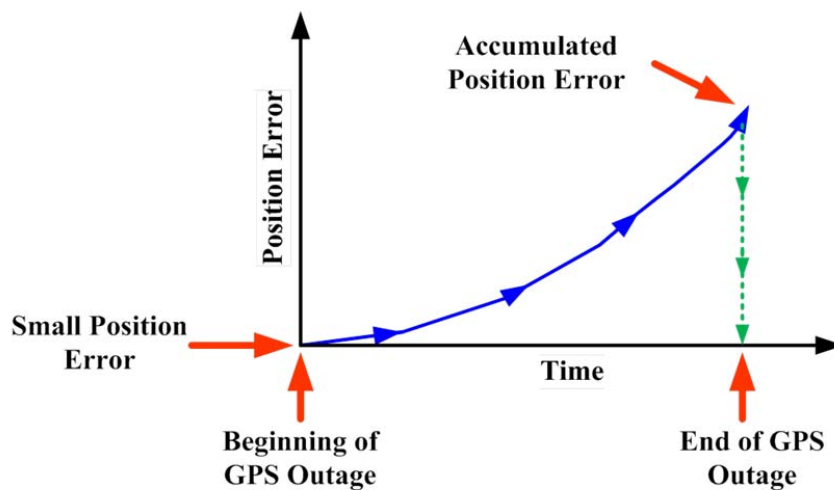
Figure 1.1: The effect of GPS outages.

Inertial sensors can be divided into two general categories according to their accuracy (El-Sheimy 2012). The first category includes navigational and tactical grade INS, which are accurate, have minimal noise interference in the signal and can be used for long periods of time without significant drifts. The second category includes low cost and compact commercial sensors such as Micro Electro Mechanical System (MEMS). These sensors have high noise and

drift rates in the output, and as such, require special algorithms to be modelled and compensated for error growing. Civilian navigation applications (such as vehicle and pedestrian navigation) are part of a huge consumer market for low-cost and compact size MEMS inertial sensors. Table 1.1 (Barbour 2004) shows the expected accuracy ranges for the different inertial grades.

Table 1.1: Inertial Sensor Application Grades.

Category	Application Grade	Gyro Performance	Accelerometer Performance
Low Accuracy	Consumer (MEMS)	>1 deg/s	>50 mg
High Accuracy	Tactical	~1 deg/h	~1 mg
	Navigation	0.01 deg/h	25 μg

1.2 Smartphones and Mobile Navigation Market

In the recent years there has been a significant increase in demand for pedestrian navigation with hand-held devices, particularly for GPS-denied environments. Portable Navigation Devices (PND) such as tablets, smartphones, and other hand-held devices are widely used and have become a large part of our daily activities. Most of these devices include GPS, low-cost MEMS sensors, accelerometers, gyroscopes, barometers, temperature sensors, and magnetometers. The integration of these sensors enables 3D sensing for any type of motion experienced by the device.

The manufacturers and developers of these navigation systems have started to pay closer attention to pedestrian navigation along with the vehicle navigation and the potential of switching between the two modes of operation. Plenty of applications have emerged, which

incorporate context-aware, adaptive, and personalized systems with smartphones. However, migrating into such applications requires the device to be fully embedded with self-contained systems that do not depend on pre-established infrastructure. Figure 1.2 shows the rapid growth of the Smartphone market and the expectations for sales by the year 2016 (Blodget et al. 2012). The figure suggests that worldwide sales of smartphones will reach 1600 million units by the year 2016.
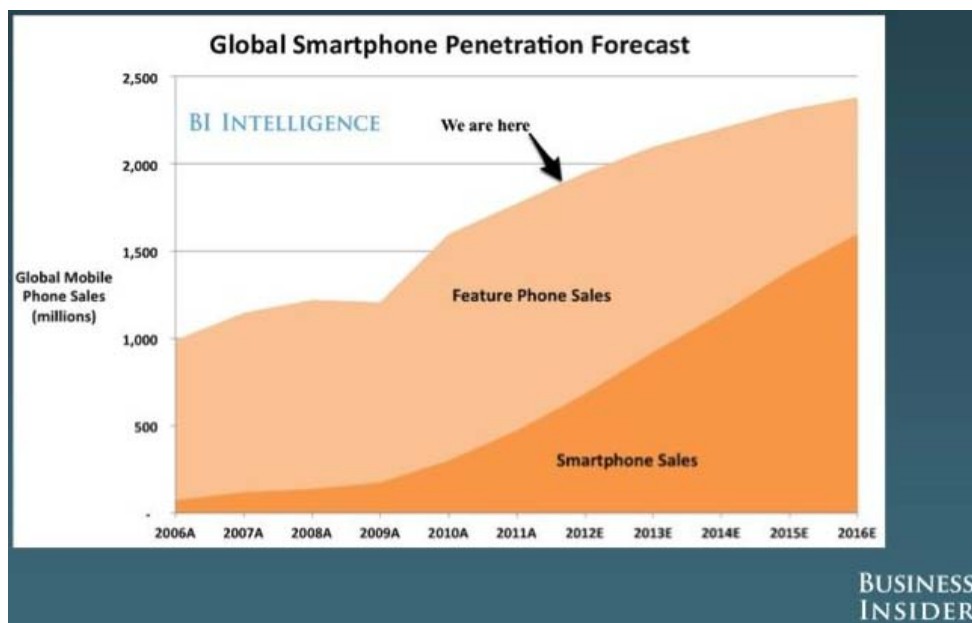
Figure 1.2: Global Smartphones sales expectation (Blodget et al. 2012).

Location Based Services (LBS) can be defined as the ability to merge location or position information with other information to provide more useful data (Schiller et al. 2004). With such a fast growing smartphone market, LBS have a variety of applications in the social networking applications, which can be accessed on the mobile device through the mobile networks. In regards to potential development of the LBS applications, *Allied Business Intelligence Inc.* (ABI) research predicts that LBS business will reach $13 billion by 2013 versus the $515 million

4

reached in 2008. A user's location can be linked to local events that match their interest by using the social networking application supported by the geo-location approaches. Figure 1.3 shows an info-graphic that highlights the use and popularity of different geo-social networking services around the world. According to the Figure, there are 5.3 billion mobile devices that use geo-social networking globally, which helps users interact relative to their current locations.
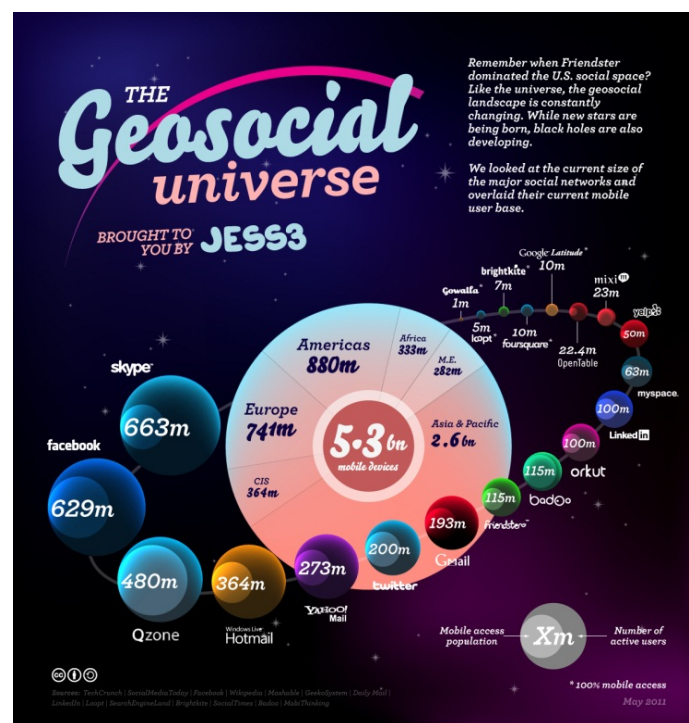
Figure 1.3: An info-graphic presenting the usage and popularity of different networking applications and services in May 2011 (courtesy of (Thomas 2011))

Friend finder, local information searches, traffic information, and crisis management applications are quickly gaining traction in the same way as personal navigation (TelecomCircle 2009). Furthermore, logistics, health care monitoring, tourism and people management are just some of the applications that can be developed with access to social networks. Therefore, the mobile

device market is pushing for the development of technologies that are able to provide significant location information, path guidance systems, and other location related services.

1.3 Problem Definition

In general, pedestrian navigation is a challenging process compared to vehicle navigation (Morrison et al. 2012). Design and cost are the most important factors for manufacturing an integrated product since navigation sensors generally are part of the mobile device carried by the pedestrian. Usually, manufacturers target devices with lightweight, small size, and power-efficient sensors. Additionally, there is a wide range of dynamics that may be produced by pedestrian motion, which may potentially occur out of the covered ranges of the used sensors (Kwakkel et al. 2008). Consequently, the selected sensors for the pedestrian navigation system should be capable of measuring the full range of the expected human motion. Also, the pedestrian is highly expected to use the navigation device in some environments with limited access to GPS such as food courts, banking machines, shopping centers, or any other places of interest. For these scenarios, the discontinuity of the GPS signal requires alternative navigation sources, such as inertial navigation, to bridge the GPS outage for seamless navigation. However, the inertial based stand-alone navigation systems suffer from error propagation in the absence of an update. Therefore, the pedestrian navigation system should have the ability to benefit from other alternative sources of navigation information. Certain technologies, including Radio Frequencies (RF) such as Wi-Fi and RFID, can be used for position updates inside the buildings. Map matching techniques can also be used to help correct the person/vehicle location.

Pedestrian navigation is the process of providing pedestrians with the necessary guidance information to reach a particular destination. One of the major challenges in pedestrian navigation is obtaining a good heading solution in different environments. Part of this challenge is that pedestrians spend most of their time in indoors; one of the most challenging environments for the PND to operate in. These challenges arise from the limitations of the information that is required to estimate the navigation parameters. Various heading resources can be exploited in pedestrian navigation for both indoors and outdoors. For shorter periods of time, the inertial sensors can be used to provide relative heading information. Furthermore, information can be retrieved from the GPS ephemeris to derive the necessary heading information which can help attitude determination with inertial sensors. The magnetic field sensor (magnetometer) can also be used to provide an absolute geomagnetic heading of the device using EMF. However, there can sometimes be a disturbance in the magnetic field due to the presence of ferrous materials around the magnetometers. In such closed environments, this can affect the estimated geomagnetic heading. The use of the magnetic field for navigation has some limitations as discussed in the literature (Afzal 2011). The magnetometer cannot be used as a standalone source for heading information in the harsh environments, particularly indoor ones (Xue et al. 2009). In addition, knowledge is required about the pre-existing magnetic anomalies resulting from man-made infrastructures (Storms & Raquet 2009). The use of magnetic field measurements in heading estimation for indoor navigation also has some limitations since the magnetic field signal may not always be strong enough. Mobile navigation devices should be kept away from any source of disturbances to avoid unwanted perturbation effects (Bachmann et al. 2004). Furthermore, devices that are used in indoor environments might experience additional

challenges since the magnetic field is not completely constant when in the presence of electronic and electrical devices.

Given the challenges of using a magnetometer on its own, it is best to combine it with other sensors to perform as an aiding source for heading estimation in harsh environments such as indoors, downtown, and parking lots. This integrated solution requires an investigation into the performance of sensors in order to improve their accuracy Magnetometer data must be calibrated in order to provide consistent magnetic field readings and reduce the impact of the perturbations on the magnetic field. In addition, a magnetometer anomaly detection technique is required to indicate the intervals of poor performance to avoid any unpredictable performance from the magnetometer.

1.4 Thesis Objectives

Ubiquitous and continuous navigation information is a basic necessity for any navigation system. An integrated GPS/INS can significantly improve the quality of navigation information for indoor and outdoor applications However, in GPS denied areas such as indoor environments and urban canyon areas; there is still a lack of suitable sources of update for the inertial sensors based solution. The primary challenge with low-cost MEMS sensors during the absence of the GPS update in PND is that they cannot operate well without proper error source modeling and source of attitude update. Different approaches have been developed for analyzing human motion in 3D space with PND such as Smartphones, tablets, and any other hand-held devices.

One of the major objectives of any mobile navigation system is to be highly convenient for the user. A common scenario in t conventional inertial-based navigation systems is to request that the user fix and align the device to his body. However, it can be quite problematic and inconvenient to force the user to keep the device in that orientation. With current advances in technology, consumer mobile devices can be used in a variety of locations: in offices, parking lots, food courts, high rises, or even entertainment hubs. Users can also hold their devices in different orientation, for example texting or reading, on a belt, or against the ear when talking. These varying device orientations and user locales make accurate sensors-based navigation very difficult to achieve.

The main objective of this thesis is to develop a pedestrian navigation algorithm capable of providing seamless navigation information. This can be achieved by developing and implementing an integrated heading estimation technique based on low cost MEMS sensors and magnetometer to improve the heading estimation strategy. The heading information received from inertial sensors and magnetometers are blended using the Kalman filter technique. In the proposed technique, the contribution of the gyroscope-based heading and the magnetometer-based heading is evaluated on the bias level of the gyroscope and the detected disturbance of the magnetic field. In order to improve the performance of the involved sensors, the effect that errors and disturbances have had on the signal must be taken into account. This integration scheme will provide heading information that can be used in a variety of environments. To achieve this objective, several important implementation and development issues must be addressed.

1. *Sensor error issues:* There is a need to investigate the possible source errors in the estimated heading from both gyroscope and magnetometer data in order to understand the factors that limit the accuracy of the derived navigation solution.

2. *Sensors calibration:* Since the pedestrian navigation system is a candidate for indoor and outdoor use, a calibration scheme that works effectively and efficiently in all environments must be determined to meet the needs of the end user. is

    o *Magnetometer calibration:* A magnetometer is an essential tool for acquiring heading information. Therefore, an effective calibration technique that can function in various environments is required. Since the movement of the device is not constrained to 2D movement for pedestrian navigation, a 3D calibration technique must be further investigated. A Swarm Intelligence (SI) based calibration technique is implemented to estimate the bias and scale factor values for the magnetometers.

    o *Low-cost MEMS calibration:* These sensors suffer errors drift regardless of the environment and usually come with manufacturer-provided calibration values, which significantly reduce the time and cost associated with calibrations. Therefore, the first issue to investigate is whether the manufacturer-provided information about the sensors calibration is sufficient for a navigation process. In this study, the first order Gauss-Markov model is used for error modeling parameters of the gyroscope bias drift estimation.

3. *Improving the magnetometer performance:* Magnetometers can perform well in outdoor areas, far away from any sources of magnetic field disturbances such as vehicles and electronic devices. However, to put the magnetometer up to the challenge of the proposed use, the magnetometer should be properly calibrated. Therefore, moving the device in the 3D

space before the navigation process starts has a large impact on the calibration process. As a result, the possible manoeuvring modes will be discussed to determine a recommended manoeuvring mode best used for the portable navigation device. In addition to this, a magnetometer anomaly detection technique is implemented to indicate how healthy the magnetometer signal is so that the recalibration process can be acquired based on the distortion that occurred to the magnetic field.

4. ***Sensor fusion technique for attitude estimation:*** To develop a robust fusing scheme for inertial based heading and geomagnetic heading, the different techniques for the integration between the gyroscope and the magnetometer heading are investigated. A proposed technique based on KF principles is implemented to fully estimate the pedestrian heading while considering different device orientations and user modes for handheld devices (smartphones, tablets, and any other handheld devices within the system constraints.)

5. ***Human activities detection:*** Recognizing different human activities that occur in motion or statically, are an important consideration for the PDR algorithm. Step detection techniques for step detection/counting are implemented with the step length estimation to achieve a total traveled distance by the user. Also, detecting static/motion periods can help in the sensors calibration process.

A complete description of the implementation of these techniques will be provided in the thesis since it represents the first step towards the development of a ubiquitous PDR that can work in different environments, under with different user modes or device orientations. All analyses and validations are done using real field datasets to provide conclusions for realistic situations.

1.5 Thesis Outline and Roadmap

This thesis explores the issues facing the development and implementation of PDR navigation applications in smartphones, tablets and other handheld devices. The thesis consists of a total of seven chapters at the beginning of which will be a brief overview. Below is an outline of chapters two through seven.

Chapter 2 introduces the necessary background for the PDR algorithm while Chapter 3 discusses the magnetometer calibration technique. One of the more important contributions of this thesis is the application of Swarm Intelligence to the magnetometer calibration presented Chapter 3. The technique starts with minimizing the data used in the calibration process. It is modified to accelerate the estimation process to fit real-time applications. A compression between the common calibration technique and the proposed technique is presented. Results of the 2D and 3D calibrations are provided at the end the chapter. In Chapter 4, the pre-processing and inline-processing of the magnetometer is presented. This chapter focuses on the various sources of error in magnetometer measurements, which affect the magnetometer signal. This describes the avoidable and unavoidable error sources. Pre-processing refers to the recommended manoeuvring modes that move the device prior to beginning the magnetometer calibration process, which allows for maximum change in the magnetic field signal levels within the 3D space. In contrast, inline-processing refers to the detection of any distortion of the magnetic field during the operation interval of the magnetometer to indicate a need for recalibration.

Chapter 5 describes the development of a heading filter applicable to pedestrian navigation. In this chapter, a seamless heading integration technique is proposed to fuse the heading estimate from both the gyroscope and magnetometer using KF.

Chapter 6 explains the test assessments conducted on the proposed techniques in different environments and under different operating conditions. The tests include a person walking in outdoor, indoor, and urban canyon testing areas. The proposed algorithm is tested against a change in the device's orientation by switching from reading/texting to belt tethering or ear talking scenarios.

Finally, Chapter 7 presents the major conclusions and contributions of this research work based on an analysis of the results. It also provides recommendations for future work. The thesis roadmap is described in Figure 1.4 below.
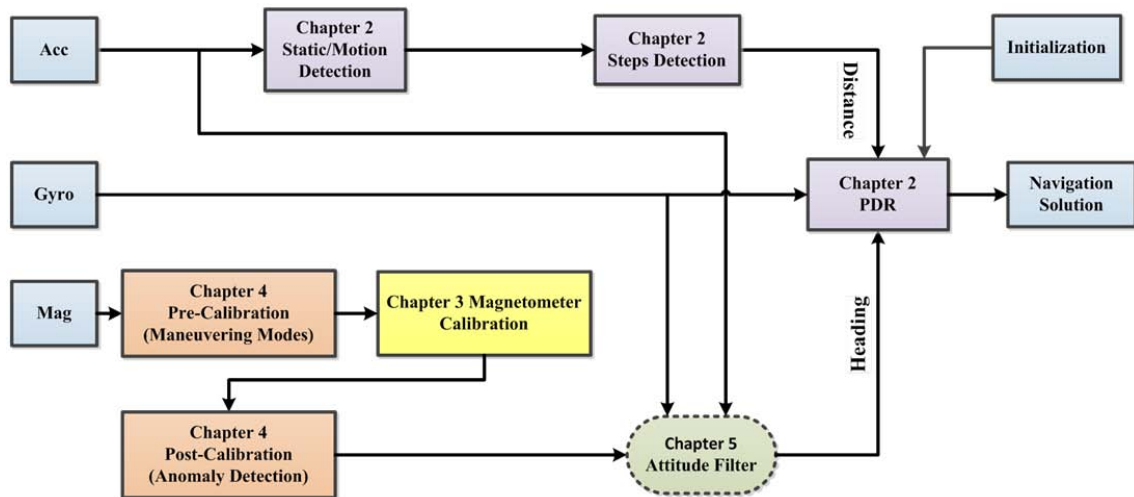
Figure 1.4: Roadmap block diagram for the thesis flow.

Chapter Two: Background

This chapter introduces the necessary background information on pedestrian navigation systems. The PDR mechanization is an effective approach to propagate user position, which is commonly used with body-fixed inertial sensors. The necessary steps required to implement a PDR algorithm are presented in this chapter including step detection/counting to evaluate the distance travelled, and the attitude representation methods for estimating the user heading. The chapter begins with the definition of various reference frames used in the implementation of a personal navigation system. The chapter then proceeds with a presentation of different techniques for personal navigation and attitude representations. Furthermore, heading estimation using the magnetometer data is explained along with the limitations of using the magnetic field in the navigation process. Finally, a brief introduction of the principles of the KF technique is given.

2.1 Coordinate Frames

This section introduces the most commonly used reference frames in pedestrian navigation.

2.1.1 The Inertial Frame

The inertial frame (i-frame) is a stationary, non-rotating, and non-accelerating reference frame with the origin at the centre of the Earth. The Cartesian coordinate system of the i-frame has its z-axis (z^i) parallel to the Earth's polar axis as shown in Figure 2.1. The x-axis (x^i) pointing

towards the mean vernal equinox and the y-axis (y^i) complete the orthogonal basis. The system's origin is located at the earth's center of mass.

- Origin: the earth's center of mass.
- x^i: towards the mean vernal equinox
- y^i: completes a right-handed system
- z^i: towards the north celestial pole

2.1.2 Earth Center Earth Fixed frame (ECEF-frame)

This frame (e-frame) has its z axis (z^e) defined in the same way as the z axis is the i-frame; however the x axis (x^e) in this case points toward the Greenwich meridian in the equatorial plane, with the y axis (y^e) at 90° east of the Greenwich meridian completing the right-handed system as shown in Figure 2.1. The origin is at the earth's center of mass.

- Origin: Earth's center of mass
- x^e: towards the mean Greenwich meridian in the equatorial plane.
- y^e: completes right-handed system
- z^e: direction of mean spin axis of the Earth

The e-frame is a non-stationary frame that rotates with respect to the i-frame at the earth's angular rate (ω_{ie}^e) of approximately 15 °/h about the polar axis.
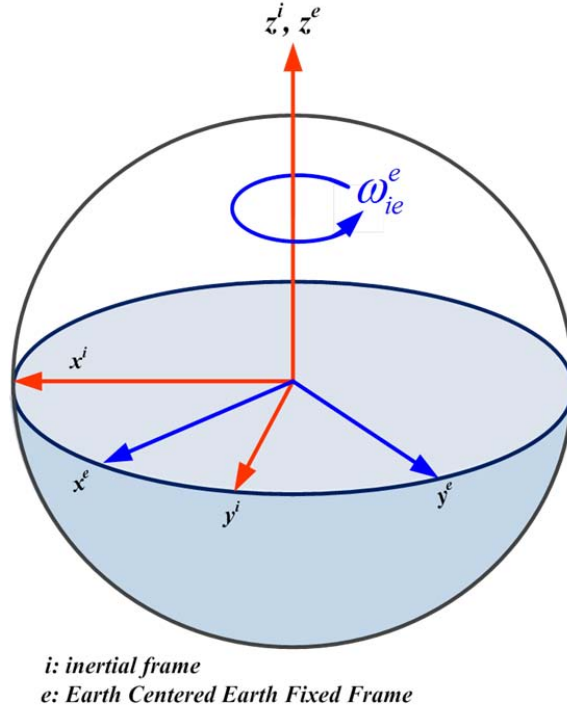
Figure 2.1: Definition of i-frame and e-frame

2.1.3 Local Level Frame (LLF)

The local level frame (l-frame), also known as the navigation frame (n-frame), is the most commonly used frame for position and attitude representation (Farrell 2008). It is defined by a plane locally tangent to the surface of the Earth at the user's position. In this research, the system-frame is the North, East, and Down (NED) axes, where Down (z^l) is the gravity vector, North (x^l) points toward the spin axis of Earth on the plane and East (y^l) completes the right handed orthogonal system as shown in Figure 2.2. The centre of NED is the origin of the navigation system.

Local-Level Frame or North-East-Down (N-E-D) Frame

- x^l: pointing towards true north

- y^l: points in the local vertical along the gravity vector.

- z^l: completes the right-handed system
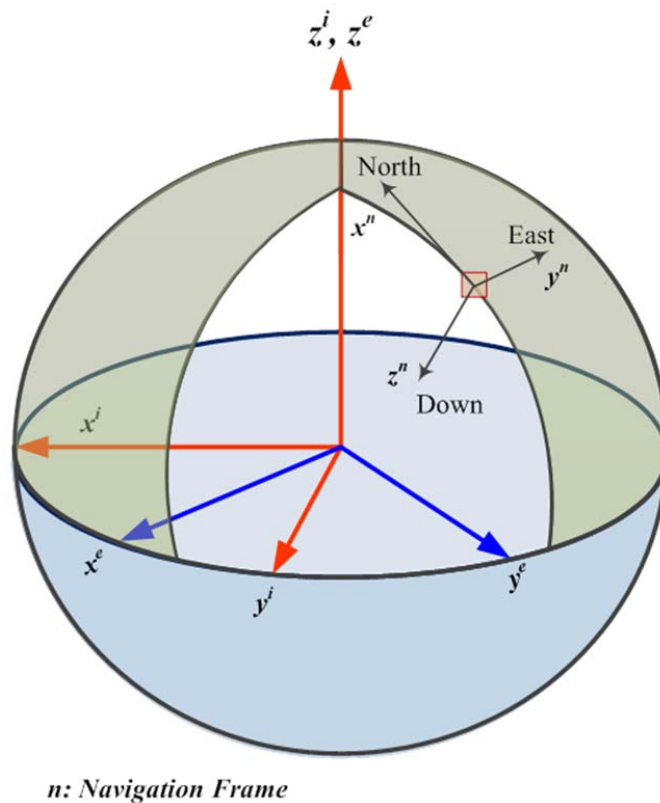
Figure 2.2: Definition of the navigation/local level frame (l-frame)

2.1.4 Body Frame

In personal navigation the main goal is to estimate the position and attitude of the user with respect to a navigation frame. The body frame (b-frame) is an orthogonal frame that is aligned with the roll, pitch and heading axes of the pedestrian. It is associated with the pedestrian and has its origin and orientation fixed. The orientation of the body frame with respect to the navigation

frame must be estimated, as the pedestrian can be oriented arbitrarily with respect to the navigation frame. In this thesis, the b-frame has an x-axis that is chosen to point toward the pedestrian's direction of motion (Forward), a y-axis that is pointed the side direction of the motion (Lateral) and z-axis is directed along the gravity vector (Down) as shown in Figure 2.3.

2.1.5 Sensor Frame

The sensor-frame (s-frame), also called the device frame, is fixed to the navigation device. It is the reference frame in which the inertial sensors operate. The device can be held in different orientation with respect to the pedestrian such as in a pocket, against an ear while talking, in a hand while texting/reading, or any other orientation. Holding the navigation device freely creates a misalignment between the sensors and body frames. The s-frame has its x-axis pointing in the same direction as the walking direction (Forward), and its z-axis pointing to the ground (Down). For this thesis, the majority of tests are conducted with zero misalignment between the sensors and body frames. For the purposes of this experiment, the device is used in texting/reading. Figure 2.3 shows the relation between the s-fame, b-frame, and n-frame.
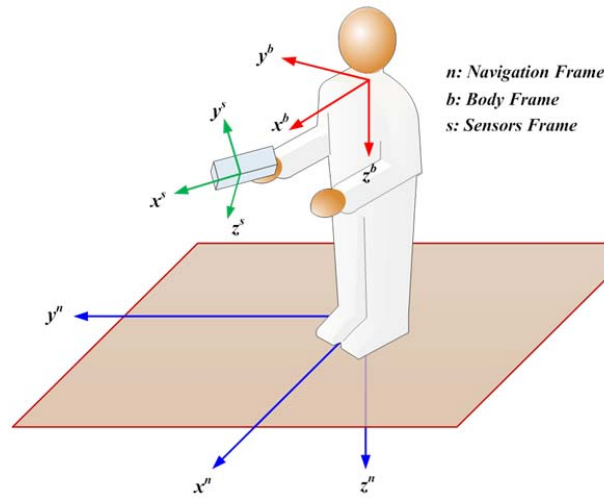
Figure 2.3: Definition of the s-frame with respect to the other frames

2.2 Pedestrian Navigation

Pedestrian navigation is a new and exciting field of mobile navigation that has a wide range of applications and a large number of potential end users. It can improve the quality of life by providing the means for navigation to aid visually impaired people in unknown environments (Wieser et al. 2007). In general, pedestrians spend most of their time indoors, the rest of the time they are moving around outside, in parking lots or going to work in urban environments. Pedestrian motion is extremely random and at a relatively low velocity. Furthermore, a person may turn suddenly at high angular velocities (Syed 2009).

Pedestrian navigation in outdoor environments is usually supported by a Global Navigation Satellite System (GNSS), which can provide long-term stable position estimates with relatively high accuracy ranging from a few meters to tens of centimeters according to the receiver technology. Generally, GPS is preferred in outdoor navigation as there is no need to know the

receiver orientation and no growth in the position error with time. The recent progress in developing high sensitivity receivers makes it possible to use GPS for navigation applications in certain harsh areas such as wooden structure buildings (Lachapelle et al. 2004; MacGougan et al. 2002). However, their weak power levels and signal reflections limit their use in many indoor settings (Zhang et al. 2010).

Estimating a person's position becomes more challenging in indoor environments or under conditions where the GPS signals are not continuously available, since there are significant shortcomings, such as:

- Loss of satellites;

- Multipath;

- Signal jamming or fading; and

- Inability to provide heading information correctly.

A major advantage to using inertial sensors is that it they are self-contained and can be packaged and sealed from the environment (Nebot & Durrant-Whyte 1999), and can therefore work as a standalone. INS has been used in land vehicle applications (El-Sheimy 1996; Lapucha et al. 1990), in aerospace vehicles (Crocker & Rabins 1970), and military applications such as ships, submarines, and missiles (Rogers 1996). The main disadvantages of standalone inertial sensors navigation systems are the unbounded growing of error over time and deciding the initial conditions. This requires an integration of inertial sensors with other sensors or referenced techniques. In order to reduce the drift for long periods of standalone inertial navigation system use, it is necessary to reset the unit while the vehicle or the person is stationary. This can be

accomplished by using the Zero Velocity Update (ZUPT) approach or landmark points with predefined coordinates, known as the Coordinate Update (CUPT). The IMU provides high frequency information to generate position estimates between GPS data and velocity fixes. Furthermore the data provided by the GPS may be faulty or may not be available for extended periods of time. During these periods the IMU provides the navigation information either in a standalone mode or in combination with any other available aiding sources. The aiding source for the IMU can be a magnetometer which is used in most Pedestrian Navigation System (PNS) as a heading sensor to estimate the direction of the device (Bekir 2007). Another aiding source can be a barometer, which measures atmospheric pressure that once converted into height information can help estimate the altitude (Tang et al. 2005). The navigation system may also use, when appropriate, constraints on the motion of the moving platform such as non-holonomic constraints. These, for example, prevent a platform from moving sideways or vertically jumping off the ground and are used according to the dynamic whether pedestrian or vehicle.

Other externally-referenced sensing techniques that can be used for positioning indoors include video movement-sensing, infrared, active/passive RFID, Ultra-Wide Band (UWB), and Wi-Fi (Kotanen et al. 2003; Wang et al. 2007). However, the complexity and cost of the hardware and the need for dense infrastructure to provide appropriate operational range are major obstacles for a mainstream adaptation of these technologies. As a result of these challenges, the use of other external information sources for estimating navigation parameters is also common. Table 2.1 (Koyuncu & Yang 2010; Retscher & Kealy 2005) shows the expected accuracy from various positioning techniques, where y, x, and z represent the 3D coordinate position.

Table 2.1: Comparisons between various positioning systems

Technique		Navigation Information	Accuracy
GNSS	GPS	x, y, z	6 - 10 m
	DGPS (Code)		1 - 4 m
	DGPS (Phase)		5 - 10 cm
WLAN	RSS	x, y	2 - 6 m
	Finger-Printing		1 - 3 m
UWB Positioning		x, y	~ 20 m
RFID Positioning (active landmarks)		x, y	6 m
Bluetooth (active landmarks)		x, y	10 m
Cellular Phone Positioning		x, y	50 - 300 m
Inertial Dead-Reckoning		x, y	20 - 50 m/km
		z	3 m

2.3 Principles of Pedestrian Dead-Reckoning (PDR)

This section introduces the concept of the PDR technique and its main components.

2.3.1 Dead Reckoning (DR) Technique

PDR is a process of determining the position of a person who is traveling on foot using the estimated traveled distance and direction. PDR techniques (Gädeke et al. 2011; Godha & Lachapelle 2008; Groves et al. 2007; Jirawimut et al. 2003; Kim et al. 2004; May et al. 2003; Ojeda & Borenstein 2007) can help bridge the GPS signal gaps in outdoor environments or be used as the main navigation technique for indoor or GPS-denied environments. It is a relative means of positioning where the initial position and heading of the user are supposed to be

22

known. PDR works for in situations where a PND is handheld or rigidly mounted on the body and the alignment and calibrations for the system have been accomplished. In a classic configuration, the inertial sensors data is integrated to provide the navigation information. However, PDR offers an interesting strategy for inertial sensors by exploiting the kinematic qualities of human gait (Beauregard 2007; Lee & Mase 2001; Stirling et al. 2003; Suh & Park 2009) and prevents the need for continuous integration processes even when the user is not moving.

In PDR, the total travelled distance can be calculated by estimating the step length and counting the number of steps. Most PDR systems use data from accelerometers to detect the occurrence of steps and provide a means for estimating the total travelled distance and direction in which the step was taken. For these systems, the position error is proportional to the number of steps. In addition to these basic objectives, the technique must be able to estimate the orientation of the device for the leveling process and minimize the errors inherent in the calculation processes. The basic concept and components of the proposed PDR algorithm are shown in Figure 2.4. Based on the information presented, there are two important parameters of the PDR technique: human motion analysis and user attitude estimation. The human motion analysis strategy includes static/motion detection, step detection/counting, and step length estimation.
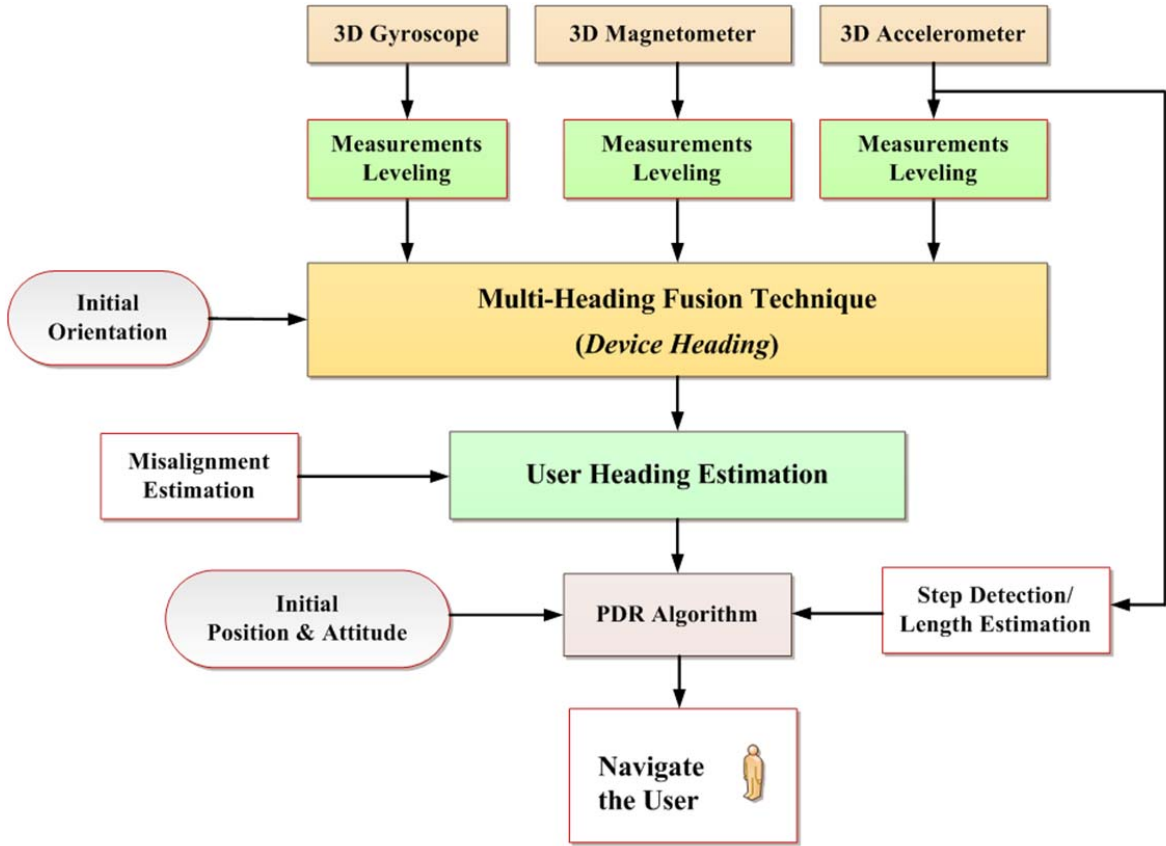
Figure 2.4: The main concept of the PDR algorithm

The process of the PDR technique begins when the walking mode is detected. The solution is initiated with the initial user position and device orientation. Once the parameters are estimated, the initial position can be propagated using Equation (2.1) and Equation (2.2) for the latitude (φ) and longitude (λ), respectively (Boulic et al. 1990):

$$\varphi\left(k^{+}\right)=\varphi\left(k^{-}\right)+\frac{\Delta r_{PDR}\cdot cos(\psi+\psi_{mis})}{R_{N}\cdot\varphi\left(k^{-}\right)+h\left(k^{-}\right)} \tag{2.1}$$

$$\lambda\left(k^{+}\right)=\lambda\left(k^{-}\right)+\frac{\Delta r_{PDR}\cdot sin(\psi+\psi_{mis})}{R_{M}\cdot\varphi\left(k^{-}\right)+h\left(k^{-}\right)\cdot cos\left(\varphi\left(k^{+}\right)\right)} \tag{2.2}$$

In the above equations, k^+ and k^- denote the current and previous steps, respectively. ψ_{mis} Ψ_{mis} is the misalignment angle between the device forward and user direction, in the event they are not aligned in the same direction. The angle ψ refers to the heading measured in the navigation frame. Step length is denoted as Δr_{PDR} Δr_{PDR}. R_N and R_M are the ellipsoidal radii of the earth, and h is the ellipsoidal height. The ellipsoidal radii are estimated by the following formulae:

$$R_N = \frac{a}{(1 - e^2 \cdot sin^2(\varphi_b))^{1/2}} \tag{2.3}$$

$$R_M = \frac{a(1 - e^2)}{(1 - e^2 \cdot sin^2(\varphi_b))^{3/2}} \tag{2.4}$$

Where a and e are the semi-major axis and linear eccentricity of the reference ellipsoid, respectively. Figure 2.5 shows a representation for the position propagation in the PDR technique.
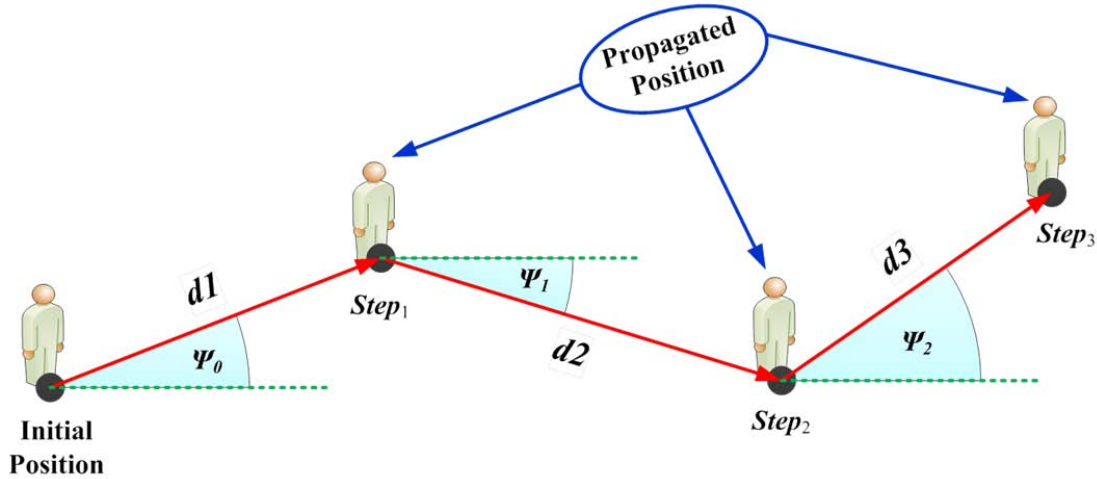
Figure 2.5: Position propagation in PDR approach

2.3.2 Static/Motion Detection

It is important to distinguish between different user activities for the navigation solution. An algorithm is described, which recognizes the walking intervals from others such as stationary or magnetometer calibration intervals. The algorithm is used to eliminate confusion about what is or is not a step, which generally creates an error in the counting. The detection of the stationary periods can help in calibrating the inertial sensors to eliminate the error drifts. Also, detecting the device manoeuvring periods helps calibrate the magnetometer measurements. To achieve the detection process and to distinguish between the different periods, a simple logic is applied using a threshold crossing for accelerometer data. The gravity is subtracted from the acceleration norm. The resulted data is compared with a known threshold (obtained by repeated tests) to conclusively detect stationary movement from walking or manoeuvring as shown in Figure 2.6. In this figure, a handheld Smartphone was moved in the 3D space followed by a stationary period and finally walking interval.

Accelerometer Data

(a) Raw accelerometer data

Static/Motion Detection
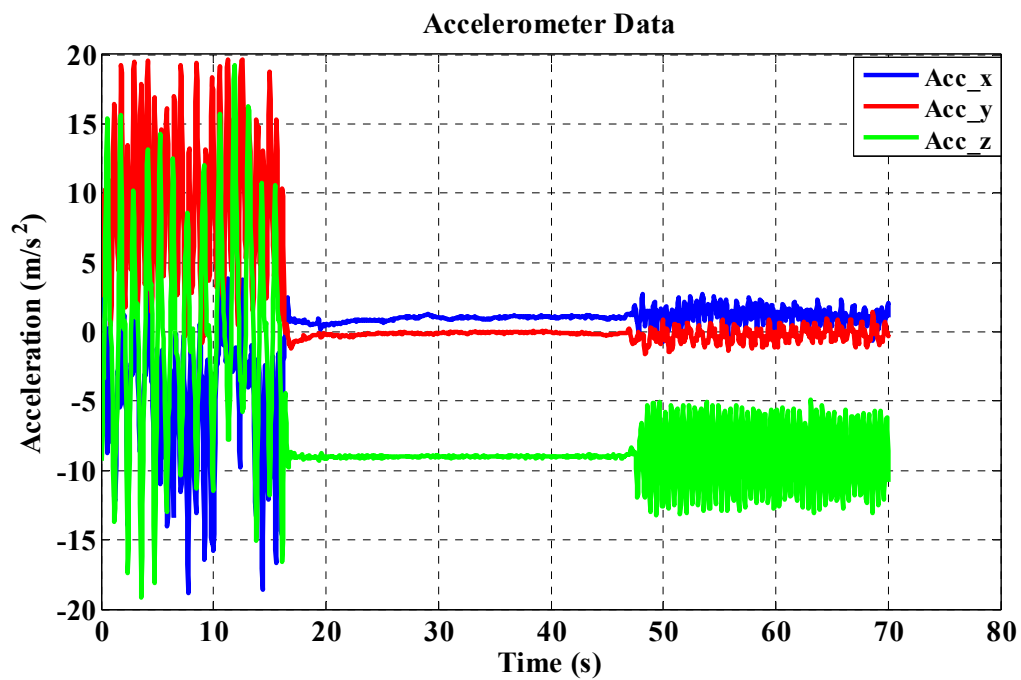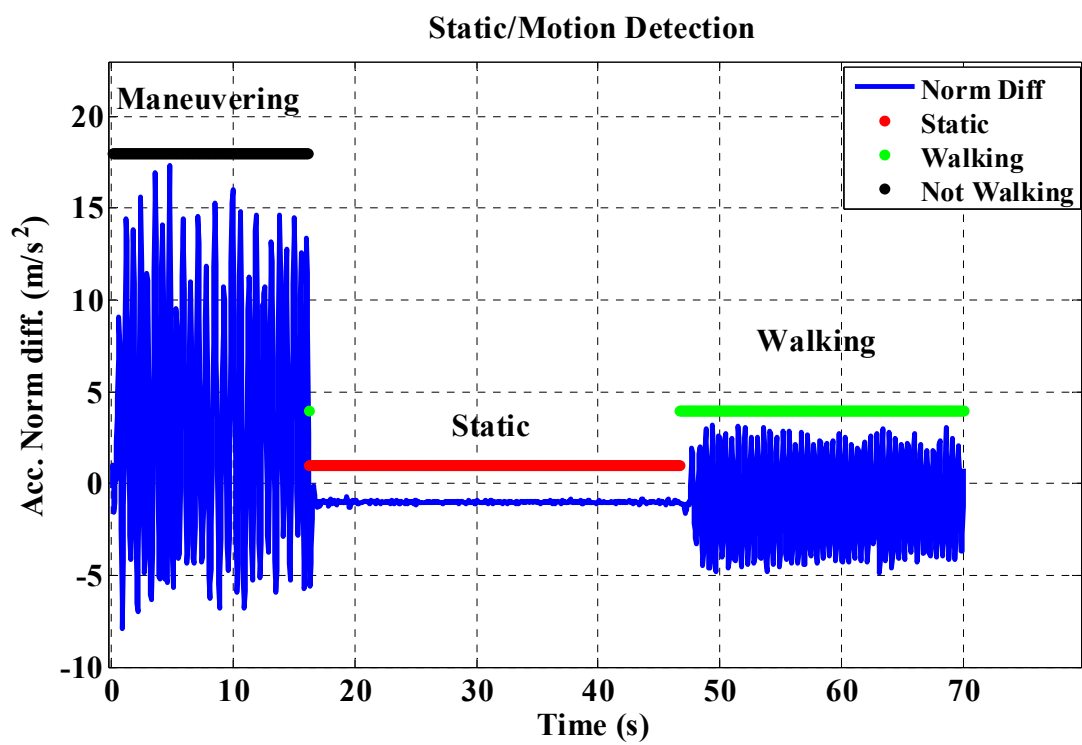
(b) Static/Walking/manoeuvring detection

Figure 2.6: Human activities recognizing

The design of detection algorithm is an important aspect in pedestrian navigation since any false step taken contributes to the position error. The technique is based on detecting the maximum variation in the acceleration within a window of data and comparing it to a certain threshold. The manoeuvring movement has the biggest variation as the device is moved in 3D space for the purpose of calibrating the magnetometer measurement. Thus, it has the biggest threshold value, meaning any value greater than 4 m/s^2. The walking activity can have threshold values anywhere between 1 and 4 m/s^2 while stationary achieves values less than 1 m/s^2.

2.3.3 Step Detection and Step Counting

Step detection is a basic step in any PDR technique. A step detection algorithm can be performed based on the different kinds of sensors. In this thesis, a step event detection scheme uses the acceleration sensed by the accelerometers. Once the step is detected, the total number of steps for a pedestrian can be counted. As a result, the total travelled distance can be estimated by multiplying the step length by the total number of steps. The norm for the three accelerometers is used as in Equation (2.5), where it is possible to clearly identify the steps by observing, for example, the signal over time. Steps are detected as peaks in the resulting norm where the step is at the highest local maximum in the norm acceleration between the current peak and the previous step peak.

$$accel\_norm = \sqrt{(f_x^2 + f_y^2 + f_z^2)} \qquad (2.5)$$

The process for step detection can be summarized as follows:

– Define the necessary parameters for the step detection process;

- o window_size: Number of samples to be searched for a step that is ½ second.

- o norm_threshold: The difference between the maximum and minimum norm values. The range of this threshold is set between 3.5 m/s^2 and 15 m/s^2 to recognize the walking activity from static or moving the device for calibration.

- o walk_freq: The walk frequency between detected steps. The range of this threshold is set to be between walk_freq_min = 1.5 m/s^2 and walk_freq_max = 6 m/s^2 to recognize the normal walking.

- o index_threshold: Minimum epochs between steps which is ⅓ second.

– Calculate the acceleration norm as in Equation (2.5).

– Signal peaks detection is performed by recognizing the local maximum and minimum values within a window of size (window_size) and comparing that with the norm_threshold.

– Estimate the user walk frequency as the time between the current candidate step and the previous detected steps and compare to the range of walk_freq_max and walk_freq_min.

$$walk\_freq_k = \left(\frac{1}{T(Step_k)} - \frac{1}{T(Step_{k-1})} \right)$$
(2.6)

– To validate the candidate step, the number of epochs between the current candidate step and the previous detected step is calculated and compared to index_threshold.

The parameters or thresholds used must be calibrated as the walking style differs from person to person (Ladetto 2000). These parameters are set based on testing different values to reach those that are most appropriate yield the best performance of the step detection algorithm. Figure 2.7

shows the result for the step detection technique. The figure shows that the algorithm was

successfully able to detect all steps correctly during the walking period of the test
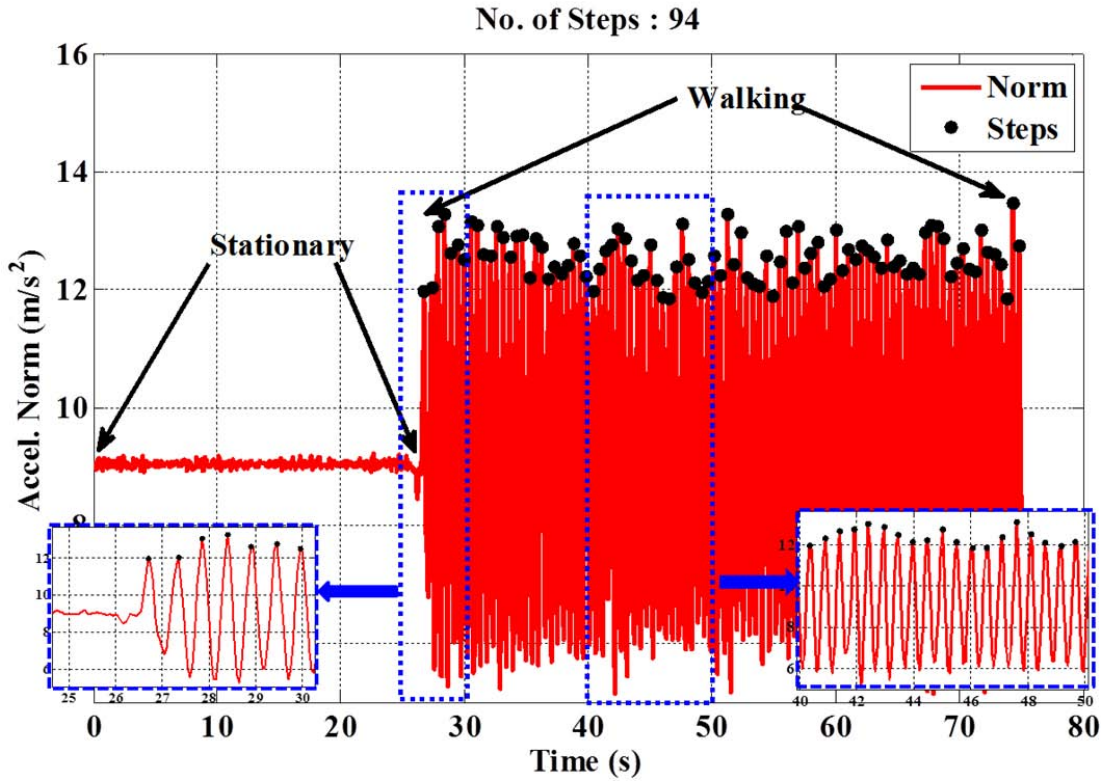
Figure 2.7: Detected steps from 3D accelerometer data

2.3.4 Step Length Estimation

Step length is an important component in PDR because in order to calculate the total travelled

distance of a person while walking, the length of every detected step must be estimated. In this

work, the device is supposed to be firmly attached to the user's body like much of the work in

the literature (Foxlin 2005; Li et al. 2010; Sabatini et al. 2005; Sagawa et al. 2000). A simple

method to estimate the total distance travelled by detecting the step and using a constant length

30

might be satisfactory for estimating energy consumption during the day but is not accurate for position estimation.

(Ladetto 2000) estimates the step length using the measured acceleration with the IMU fixed to the body. This approach assumes that the human step length varies according to a stable value in average. In order to improve the PDR accuracy, the step length should not be considered a constant since it varies significantly from step to step depending on the person, leg length, walking speed and frequency (Weinberg 2002). Another approach utilizing the ZUPT technique is presented by (Feliz Alonso et al. 2009) which does not consider any user parameters and activity patterns. The algorithm applies zero velocity updates every time a step is detected as the velocity is known to be zero to correct the linear velocities obtained after integrating the accelerometer data. As a result, the bias drift in velocity and position can be attenuated.

In this thesis, a general model is used for step length estimation (Kim et al. 2004). It is based on the relationship between the step length and the measured acceleration. The model is reliable for the change in the user speed which leads to an improved level of PDR precision. Equation (2.7) represents the relation between measured acceleration and step length.

$$SL = l \cdot \sqrt[3]{\frac{\sum_{i=1}^{N} |A_i|}{N}} \tag{2.7}$$

Where A and N are the acceleration norm after removing the gravity component and the number of samples between the current step and the previous step, respectively. The step length tuning factor l is set to be 1.25 based on conducted tests for different users.

31

2.3.5 Attitude Kinematic Equations

Gyroscopes measure the angular rates (also known as angular velocity) around their axes; the attitude of the device can be derived by integrating rigid body kinematic equations, starting from a known initial attitude at a given point in time. Attitude kinematic equations can be used to compute estimates of a moving body's attitude from measurements of the moving body's angular velocity. The formulation of these equations depends on the attitude parameterization (Bageshwar 2008). In this thesis, attitude parameterizations are used to define the Direct Cosine Matrices (DCMs) that specify the orientation of the object in the body frame relative to the navigation frame. Numerous attitude parameterizations methods are discussed and surveyed in (Shuster 1993). Among the different techniques, Direction Cosine Matrix (DCM), quaternion, and Euler angles are commonly used in the inertial navigation (Savage 2000). In this section, the relationships between the different attitude parameterizations will be discussed. For more details about the quaternion technique, readers are referred to (Altmann 1986; Kuipers 1999).

2.3.5.1 Euler Angles Representation

It is possible to completely rotate from one frame to another by performing three rotations about the three axes. This can occur when any coordinate frame is represented by three orthogonal coordinate axes. The three successive rotation angles are referred to the Euler angles, shown in Figure 2.8 and introduced by Leonhard Euler (1707-1783).
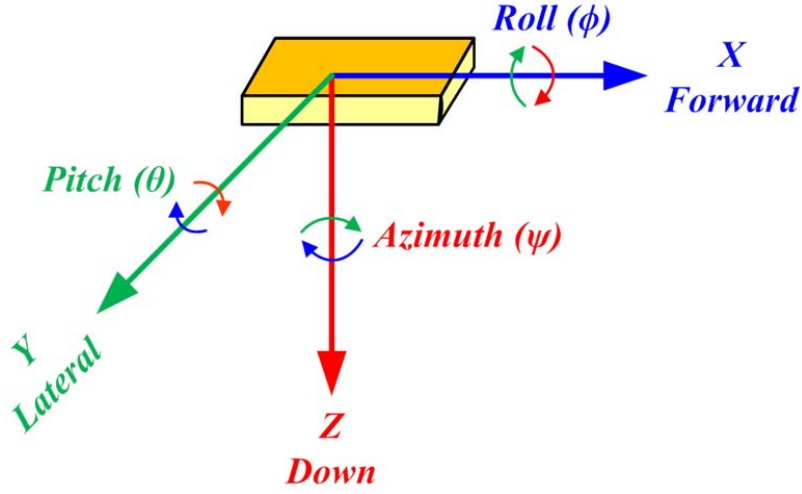
Figure 2.8: The definition of Euler angles

Equation (2.8) gives an explicit form of the primitive direction cosine matrices for right-handed rotations about the x, y and z axes, respectively.

$$R(\phi) = \begin{bmatrix} 1 & 0 & 0 \\ 0 & \cos\phi & \sin\phi \\ 0 & -\sin\phi & \cos\phi \end{bmatrix}$$

$$R(\theta) = \begin{bmatrix} \cos\theta & 0 & -\sin\theta \\ 0 & 1 & 0 \\ \sin\theta & 0 & \cos\theta \end{bmatrix} \qquad (2.8)$$

$$R(\psi) = \begin{bmatrix} \cos\psi & \sin\psi & 0 \\ -\sin\psi & \cos\psi & 0 \\ 0 & 0 & 1 \end{bmatrix}$$

Euler angles are the most common representation for describing the attitude of one coordinate frame with respect to another because it provides a direct measure of the actual angles that are formed between two different reference frames. As the sequence of rotations from one frame to the other is performed Euler angles can have a singularity at a particular orientation (Giardina et

33

al. 1981). The disadvantage however, is that Euler angles require an additional logic to avoid the conditions that cause the singularity. The attitude of a body with respect to the local-level coordinate frame is defined by the three Euler angles, namely roll *(ϕ)*, pitch *(θ)*, and azimuth *(ψ)*.

2.3.5.2 DCM Representation

DCM is a 3x3 rotation matrix consisting of nine unique elements. The columns for each element represent the rotations from the axes of one frame into the axes of another frame (Titterton & Weston 2004). For attitude determination, the rotation matrix is often referred to as the DCM and is considered the fundamental quantity specifying the orientation of a rigid body. Unlike the Euler angle parameterization, it completely describes the orientation of one coordinate frame with respect to another, without singularities. The main disadvantage of the direction cosine parameterization of attitude is that it contains nine parameters, whereas the Euler angle parameterization has only three (Schleppe 1996). The DCM is commonly represented by Equation (2.9)

$$C_a^b = \begin{bmatrix} c_{11} & c_{12} & c_{13} \\ c_{21} & c_{22} & c_{23} \\ c_{31} & c_{32} & c_{33} \end{bmatrix}$$

(2.9)

2.3.5.3 Quaternions Representation

Sir William Rowan Hamilton, an Irish mathematician (1805-1865), invented the hyper-complex numbers of rank 4 and termed them quaternions. Quaternions are a four-dimensional extension

of complex numbers. A quaternion consists of four scalar components, three of which are commonly grouped into a vector component. Quaternions use four components to parameterize a three dimensional orientation and, thus, only three of the four components are independent. Quaternions are based on Euler's theorem of rotation which states that it is possible to move from one coordinate system to another through one rotation using Euler angles. This requires a single rotation about a three dimensional vector to transform between two frames (Grubin 1970).

A quaternion q is represented in vector notation form as in Equation (2.10):

$$
\begin{aligned}
q &= q_1 + iq_2 + jq_3 + kq_4 \\
&= [q_1\ \vec{q}]
\end{aligned}
\tag{2.10}
$$

Where $\vec{q} = (q_2, q_3, q_4)$ represents vector part and the scalar part of the quaternion q is denoted by q_1. The quaternions should satisfy the following normality condition;

$$
q_1^2 + q_2^2 + q_3^2 + q_4^2 = 1
\tag{2.11}
$$

The differential equations for the quaternion parameters is given by (Schwarz & Wei 2000):

$$
\dot{q} = \frac{1}{2}
\begin{bmatrix}
0 & \omega_z & -\omega_y & \omega_x \\
-\omega_z & 0 & \omega_x & \omega_y \\
\omega_y & -\omega_x & 0 & \omega_z \\
-\omega_x & -\omega_y & -\omega_z & 0
\end{bmatrix} q
\tag{2.12}
$$

Where $\omega = (\omega_x \quad \omega_y \quad \omega_z)^T$ is the angular velocity of the moving device. The quaternion representation of the frame transformation has an advantage over other representations, such as Euler angles and DCM. The quaternion algebra is the preferred choice due to better accuracy,

more efficient implementation (less time consuming), and strong protection against gimbal lock situations that are usually associated with Euler angle implementation.

The following summarizes the advantages of quaternion algebra over other representations:

- There is no singularity when approaching a pitch angle of 90$^\text{o}$.

- The linearity of its differential equations makes it is possible to implement via digital computers.

- There is less complexity in computations compared to Euler angles and DCM representations, which improve the real time performance.

2.4 The Earth's Magnetic Field (EMF)

The Earth's Magnetic Field (EMF), as measured at any point on the Earth's surface is a combination of several magnetic contributions generated by various sources. The magnetic compass was first used in China around 200 B.C., and was transferred to Europe much later to be used as indispensable tool for maritime navigation. The geomagnetic field can be fully described by measuring the intensity and two angles or three orthogonal components (Mandea et al. 2006). The two angles are the declination and the inclination angles while the orthogonal components are X, Y, and Z for the directions towards geographic north, east and vertically down, respectively. Nowadays, with the progress in sensors technology, the EMF can be precisely measured using the magnetometer. Valuable information can be extracted from the magnetometer measurements with the proper transformation of the field components such as the geomagnetic heading.

Generally, magnetometers measure the vector components of the magnetic field. The magnetic field can be characterized by different components. These include the strength of the magnetic field (F), the vertical and horizontal components (V, H), and the inclination and declination angles (**I**, **D**). What makes these parameters important for the magnetometer operation is that their values can be considered roughly constant over a small area, which is normally covered by a walking person. These values used as a reference for the measured values by the magnetometer to be compared.
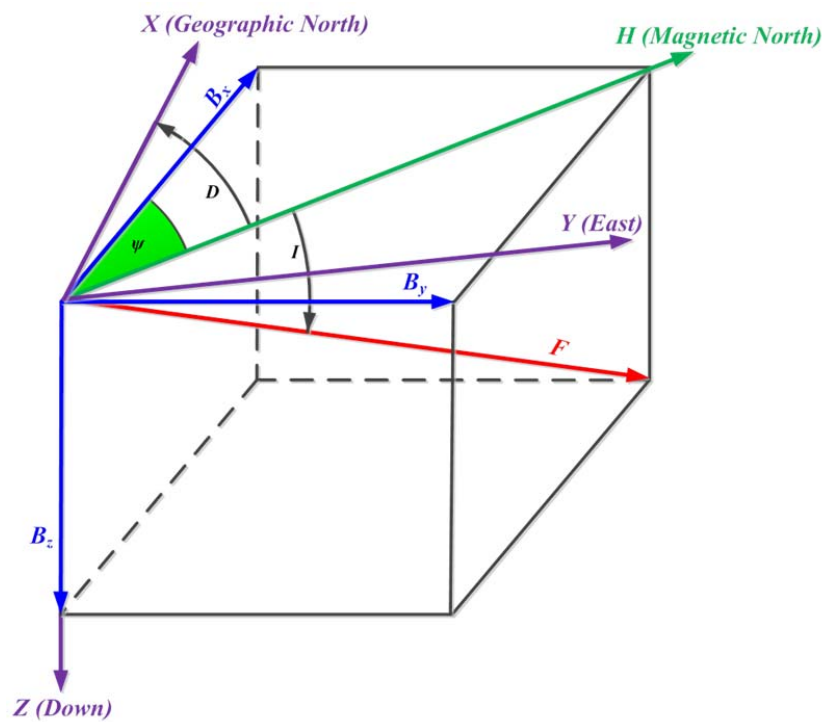
Figure 2.9: Geomagnetic field components and vectors.

Three parameters are required to describe the magnetic field at any point on the surface of the Earth which can be sensed by an orthogonal arrangement of magnetometers as shown in

Figure 2.9 where B_x, B_y, and B_z represent the measured components of the magnetic field vector. D is the declination angle referenced to true North, which indicates the difference, in degrees, between the true north and magnetic north, which ranges from 0 to 360°. The field also has a vertical contribution; the angle between the horizontal and the magnetic field direction is known as the inclination angle. Magnetic inclination varies from 90° (perpendicular to the surface) at the poles to 0° (parallel to the surface) at the equator. The magnitude of the magnetic field varies from about 650 *mGauss* at the poles to about 300 *mGauss* at the equator.

The heading with respect to true North can be estimated as:

$$\psi = \tan^{-1}(\frac{B_x}{B_y}) \pm D$$

(2-13)

Equation (2-13) implies that the estimated magnetic heading is affected by any disturbance or perturbation in the horizontal magnetic field components. Consequently, the local magnetic components controlled the magnetic heading estimation process.

The strength of the magnetic field is expressed as the norm of the measurements. Any significant deviations from the expected values for the different magnetic field components may be presented as disturbances. Unfortunately, small random variations can occur in the environment when someone is moving.

The magnetic field can be characterized by four major components:

-   ***Total Geomagnetic Field Strength:*** $F = || B_x + B_y + B_z ||$

-   ***Geomagnetic Field Horizontal Intensity:*** $H = || B_x + B_y ||$

38

- *Vertical Geomagnetic Field Intensity*: $V = \| B_z \|$

- *Geomagnetic Field Inclination Angle:* the angle of the magnetic field above or below horizontal, $I = \tan^{-1}\left(\dfrac{V}{H}\right)$

The expected values for the different magnetic field parameters are shown in Table 2.2 with respect to the city of Calgary, Alberta, Canada (Finlay et al. 2010).

Table 2.2: The reference values of the tested parameters.

Component	Symbol	Ref. Value	Unit
Total Magnetic Field	*F*	567	*mGauss*
Horizontal Component	*H*	161	*mGauss*
Vertical Component	*V*	543	*mGauss*
Inclination Angle	*I*	73.5	*Deg.*
Declination Angle	*D*	14.8	*Deg.*

Unpredictable perturbation of the magnetic field is a major drawback of using geomagnetic sensors. Pedestrians spend most of their time in harsh environments such as urban areas and indoor environments. Unlike outdoor environments, indoor ones mainly contain metal infrastructures, electrical and electronic devices. Such objects generate or influence the magnetic field which can alter the EMF magnitude and direction. These kinds of disturbances lower the performance of the magnetometer which leads to inappropriate positioning for pedestrians. However, a change the environment affects the magnetometer's measuring operation.

Two tests were conducted outdoors to show the impact of the perturbations on the EMF components where the device was held stationary. During the first test the device was kept away from any source of perturbations while in the second a magnetic dipole was moved near the

device for approximately 20 seconds. Figure 2.10 shows the components of the magnetic field in the absence of any source of perturbations. As depicted in the figure, there is no change in the values of the magnetic field components. This reflects on the heading estimation as heading is almost constant without any change, seen in Figure 2.11.
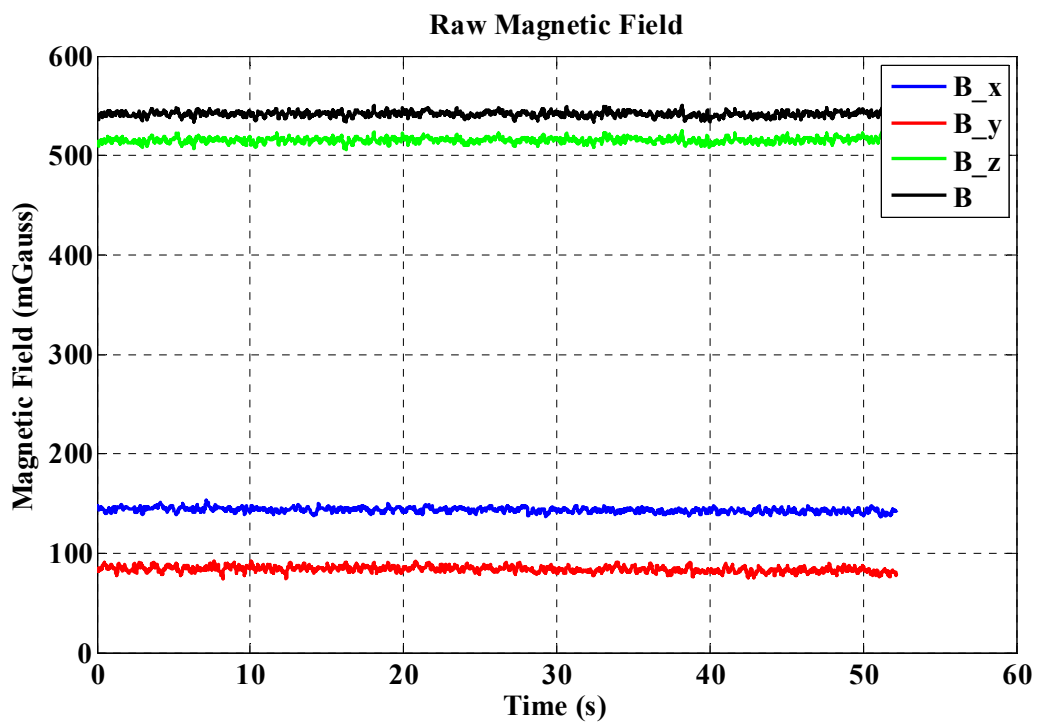
Figure 2.10: EMF as sensed in free perturbation area.
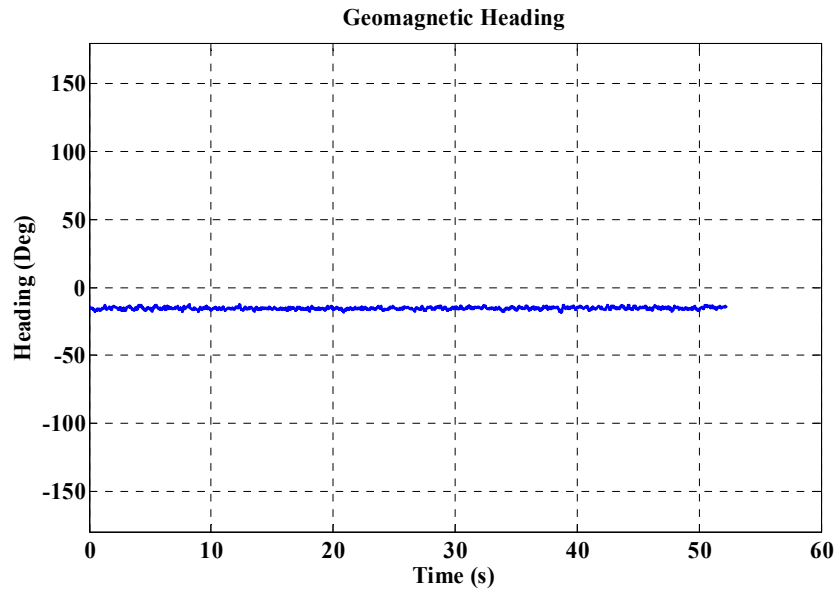
Figure 2.11: Heading estimates from non-perturbed magnetic field.

In contrast, Figure 2.12 depicts the magnetic field components in the presence of a perturbation source as it is moved closer to the device. The presence of an artificial magnetic field beside the device causes a disturbance for the magnetic field where the values change abruptly (refer to Figure 2.13). The change in the magnetic field components creates a change in the estimated value of the heading as it is supposed to be constant.
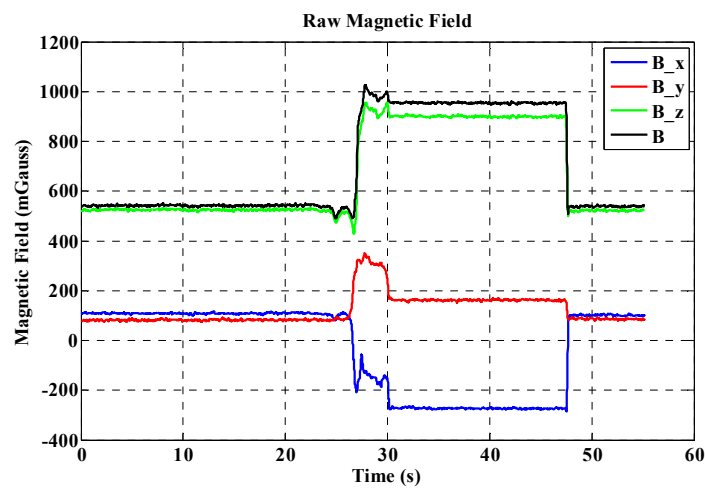
Figure 2.12: EMF's components in the presence of perturbation.

41
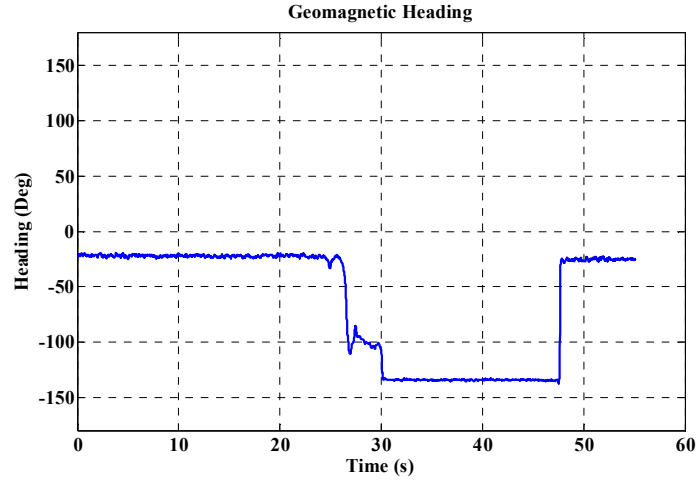
Figure 2.13: Heading estimates from perturbed magnetic field.

Since the EMF is weak and can be easily masked and unpredictably distorted by any kind of natural or man-made magnetic disturbance, it is necessary to evaluate and assess the performance of the magnetometer signals during the navigation process. This can be achieved by inspecting the different levels and reference values for the different components of the magnetic field. This requires the use of a technique that will compensate for the effect of the different sources of distortion. This process is known as magnetometer calibration, where the necessary parameters are estimated to reduce the effect of the magnetometer perturbations. A proposed magnetometer calibration technique is described in Chapter 3.

Occasionally, the calibration process must be repeated. Recalibration occurs when; (1) there is a significant change in latitude and longitude (2) there is a change in environment such as indoor to outdoor or to a vehicle. To detect such change in the magnetic field, a magnetometer anomaly detection algorithm should be used in combination with the navigation process to indicate the

42

need for magnetometer recalibration, described in Chapter 4. Unlike MEMS based sensors such as accelerometer and gyroscope which use mechanical sensing elements unaffected by electromagnetic components on the device, magnetometers are sensitive to the magnetic fields generated by other circuit components. The most common magnetic field sources are:

- Induced fields within any ferromagnetic materials lacking a permanent field (such as sheet steel).

- Generated fields by current flows from the power supply.

Due to these factors, most magnetometer calibrations degrade over time and regular re-calibration is a necessary step to ensure the integrity of the measurements. Even in well-designed handheld devices, these sources create extraneous fields with high magnitudes. Designers of such devices should not assume that the calibration process will always be correct for a poor layout. The device should also be moved in all possible directions in the space during the calibration process to ensure maximum benefit. Different Manoeuvring Modes (DMMs) are investigated to achieve the best estimation for the calibration parameters in the 3D Space. The purpose of this manoeuvring is to move the device in the space so as to allow the magnetometers the opportunity to cover a wide range of change in the magnetic field. This will be discussed in Chapter 4.

2.5 Kalman Filter (KF) Principles

Integrating different sources of information requires an efficient combination of sensors in an optimal filter. The Kalman filter is a well-known filter, employed in the fusion of information and estimation of states of interest. It plays a key role in several applications; because it has an

optimal combination, in terms of minimization of variance, between the prediction of parameters from a previous time instant and external observations at the present instant (Brown & Hwang 1992; Gelb 1974). The Kalman filter principle is built around two independent models: kinematic and observation. Each model has a functional and a stochastic part. The general Kalman filter consists of two main steps: a prediction and correction step. The prediction step reflects the effects produced by a change in the states and states-covariance over time while the correction step presents combined information of the states and states-covariance with the measurements and its covariance. The strength of the KF technique lies in its ability to recursively estimate current states based on previous time steps and current measurement input data.

The implementation of the KF is optimal for linear systems driven by Additive White Gaussian Noise (AWGN). The state model can be written in the following form:

$$\dot{x} = Fx + Gw \tag{2.14}$$

Where x is the state vector, F is the state transition matrix, and Gw represents the covariance matrix of the applied state model. The measurement system can be represented by a linear equation of the form of Equation (2.15).

$$Z = Hx + v \tag{2.15}$$

Where Z is the vector of measurement updates, H is the design (observation) matrix that relates the measurements to the state vector, and v is the measurement noise.

KF equations are divided into two groups; time prediction and measurement update (Grewal & Andrews 2001). The time prediction equations are responsible for the forward time transition of the current epoch (k) states to the next epoch (k+1) states. Time prediction equations are given by:

$$\hat{x}_{k+1}^{-} = \Phi_{k+1,k}\,\hat{x}_{k}^{+} \tag{2.16}$$

$$P_{k+1}^{-} = \Phi_{k+1,k}\,P_{k}^{+}\,\Phi_{k+1,k}^{T} + Q_{k} \tag{2.17}$$

Where (ˆ) denotes estimation, Φ is the model transition matrix, P is the estimated variance-covariance matrix of system states, Q is the system noise matrix, (-) denotes the estimated value after prediction, and (+) denotes the estimated value after update.

The measurement update equations utilize new measurements into the states estimate equations are given as:

$$K_{k} = P_{k}^{-}H_{k}^{T}\left(H_{k}\,P_{k}^{-}H_{k}^{T} + R_{k}\right)^{-1} \tag{2.18}$$

$$\hat{x}_{k}^{+} = \hat{x}_{k}^{-} + K_{k}\left(z_{k} - H_{k}\,\hat{x}_{k}^{-}\right) \tag{2.19}$$

$$P_{k}^{+} = (I - K_{k}\,H_{k}^{T})\,P_{k}^{-} \tag{2.20}$$

Where K is the Kalman gain, R is the measurements variance-covariance matrix. All noise terms are considered to be white sequences with known covariance. The general process of the discrete time KF is presented in Figure 2.14.

$$\hat{x}_{k+1}^{-} = \Phi_{k+1,k}\, \hat{x}_{k}^{+}$$

Prediction Loop

$$P_{k+1}^{-} = \Phi_{k+1,k}\, P_{k}^{+}\, \Phi_{k+1,k}^{T} + Q_{k}$$

$$\hat{x}_{k}^{+} = \hat{x}_{k}^{-} + K_{k}\left(z_{k} - H_{k}\, \hat{x}_{k}^{-}\right)$$

$$K_{k} = P_{k}^{-} H_{k}^{T}\left(H_{k}\, P_{k}^{-} H_{k}^{T} + R_{k}\right)^{-1}$$

Update Loop

$$P_{k}^{+} = P_{k}^{-} - K_{k}\, H_{k}^{T}\, \hat{x}_{k}^{-}$$
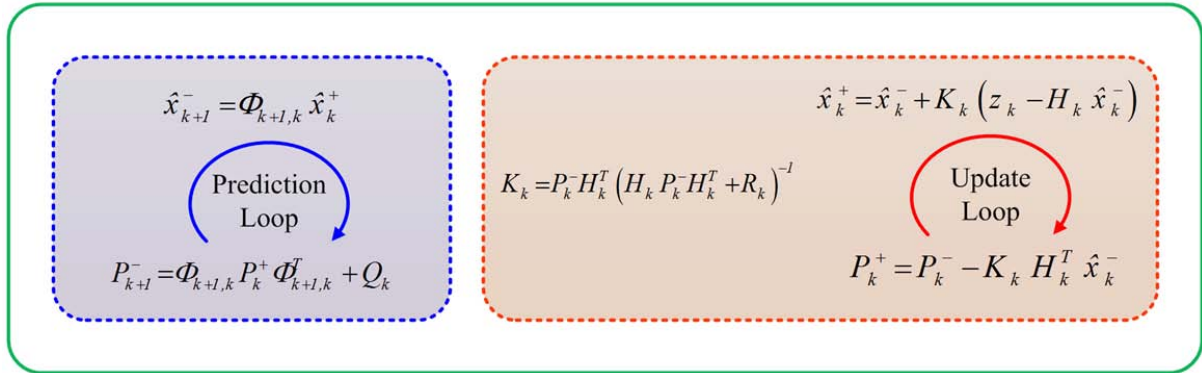
Figure 2.14: The general process of the Discrete time KF

The dynamic system used for prediction is non-linear by definition, but the Kalman filter requires a linear set of differential equations to relate one state to another. The Kalman filter performs a linearization of these equations using the Taylor series expansion of the non-linear measurement and system equations and truncates them to first-order approximations.

Chapter Three: Swarm Intelligence Based Magnetometer Calibration

In this chapter, a magnetometer calibration technique is presented using the concepts of swarm intelligence and its application to pedestrian navigation. First, a brief background is presented on the state-of-the-art real-time calibration technique for magnetometer measurements. Then, a PSO-based technique of magnetometer calibration is described.

3.1 Introduction

In recent years, inertial sensors, gyroscopes and accelerometers, have become more popular for navigation in cluttered indoor environments that challenge the capabilities of for GNSS. The output of these sensors can be used to provide different navigational information. However, the errors produced by the data from these sensors are rapidly especially with low cost MEMS sensors that achieve low accuracy levels. Consequently, regular updates are necessary to provide drift free data for device attitude estimation. For heading updates, a triad magnetometer can be employed to measure the different EMF components in the space. These components help provide an estimate for an absolute value of the device heading. The ubiquitous nature of the EMF makes magnetometers usable more favorable tool in airplanes, vehicles, and ships. Nowadays, they are also available in smartphones, tablets, and most other handheld devices. To provide an accurate heading solution from a magnetometer or gyroscope depends on the cost, accuracy, and type of application at hand. Therefore, magnetometers offer the opportunity to have an update source for the heading can therefore be used over extended periods of time, especially in magnetically stable environments.

In densely cluttered outdoor or indoor areas, navigating a pedestrian with the use of a personal device becomes even more challenging due to the proximity of metallic objects and walls supported by ferrous pillars. These can cause a distortion in the EMF. Even when travelling in certain outdoor environments, the EMF can be distorted due to the presence of power lines or moving vehicles. In order to improve the performance of the magnetometer, a calibration process is required to compensate for the distortion in the measured EMF. The calibration process provides the required parameters to compensate for the various distortion effects. Therefore, without an appropriate calibration process, the magnetometer-based estimated heading is subject to inaccuracies resulting from the uncompensated errors.

In most of the previous research, the calibration of magnetometers accomplished in the magnetic field domain (Gebre-Egziabher et al. 2006). The application of the calibration algorithm has convincing benefits for the compensation of the calibration parameters. For a given region, the Earth's total magnetic field is constant and its value can be obtained from the International Geomagnetic Reference Field (IGRF) model (Finlay et al. 2010) which becomes a base for developing a mathematical model for sensor calibration (Siddharth et al. 2011). A simplified calibration technique is presented in (Caruso 1997) which determines the calibration parameters in the horizontal) (X-Y) plane only. The estimated parameters are two scale factors and two biases. Recently, a batch least square technique is presented for magnetometer calibration in (Elkaim & Foster 2006) that accounts for different distortion effects. In (Alonso & Shuster 2002), a non-linear two-step calibration parameter estimator was presented. The main operation of this algorithm was to estimate the initial values of the calibration parameters in the first step

and provide them to a linearized least square batch algorithm in the second step. An extension of this work including misalignment and scale factors is presented in (Alonso & Shuster 2003). Although the algorithm achieved good results, it becomes complex when all parameters are considered such as biases, scale factors and misalignment angles. A related work in (Crassidis et al. 2005) presented a recursive algorithm for magnetometer calibration based on nonlinear Kalman filter. In another study, (Gebre-Egziabher et al. 2006) implemented an algorithm that estimates the bias and scale factor of magnetometer based on least squares which takes in account the effect of the different distortions. The major defect of the method is that the algorithm requires several iterations to converge to the required values. The proposed work in (Santana 2009) combines the advantages in (Foster & Elkaim 2008; Lötters et al. 1998) to obtain a reasonable results from the previous technique. A game theory based calibration technique is proposed in (Siddharth et al. 2012). In this application the Kalman filter is tuned for the calibration parameters estimation using the game theory concept. The primary weakness of the technique is that nonlinearity still could not be handled.

3.2 Swarm Intelligence

Artificial Intelligence (AI) based algorithms are considered practical tools for nonlinear optimization problems (Kaniewski & Kazubek 2009). Various approaches are implemented based on AI such as Artificial Neural Network (ANN), Genetic Algorithms (GA), and Swarm Intelligence (SI). SI is the property of a system whereby the collective behaviours of (unsophisticated) agents interacting locally with their environment cause coherent functional global patterns to emerge. SI provides a basis with which it is possible to explore distributed

problem solving without centralized control or the provision of a global model (Liu & Passino 2000). Anti-Colony Optimization (ACO), Bees Algorithm, and PSO are just some examples of the approaches and versions of SI, which are implemented and explained in detail in the literature. PSO is one of the modern heuristic algorithms (Kennedy & Eberhart 1995) and can be applied to nonlinear optimization problems (Wang et al. 2006). It has been developed through simulation of simplified social models. PSO has gained wide recognition for its ability to provide solutions efficiently and for requiring only minimal implementation effort.

3.2.1 Particle Swarm Optimization (PSO)

Bird flocks, fish schools, and animal herds are all examples of natural systems where an organized behaviour is successful in producing impressive, collision-free, and synchronized movements (Kennedy & Eberhart 1995). In these natural systems, the behaviour of each group member is based on simple inherent responses. SI is mainly inspired by such kinds of animal and natural systems. Although SI is still in its infancy compared to other paradigms of artificial intelligence, it offers an attractive new research field.

Swarm-based algorithms are beginning to show promising performance in efficiency, ease of use and in comprehensive functionality (Parsopoulos & Vrahatis 2010). One of the most interesting research areas within computational swarm intelligence is the PSO which was developed based on the concepts and rules of socially organized populations in nature. The swarm is a group of individual agents called particles. Each particle follows a simple behaviour to achieve best performance by following the best in the group. PSO is a population based stochastic

optimization technique, developed by Eberhart and Kennedy in 1995 (Kennedy et al. 2001). They claimed that searching for a food source is similar to finding a solution for a common research goal (Hernane et al. 2010). In comparison with other AI based optimization techniques, the power of PSO lies in its simplicity of implementation. The performance of different optimization techniques used in industry today, along with their computational efficiency, clearly indicates that PSO performed better than other algorithms in terms of success rate, solution quality, and convergence speed (Elbeltagi et al. 2005). It can be applied to solve various functional optimization problems. In contrast with other optimization algorithms that require the objective function to be differentiable, PSO can work in cases of non-differentiable transfer functions where no error information is available (Rajini & David 2010).

The PSO technique employs a set of feasible solutions called a 'swarm of particles' that are populated in the search space with initial random positions and velocities as shown in Figure 3.1 (a). At any particular instant, each particle has its own position and velocity (Havangi et al. 2010). In essence, it is trying to find its own solution for the problem in the search space to target the optimal "solution". All particles have fitness values that are evaluated according to the cost or fitness function to be optimized. They also have update values and velocities that control the movement of the particles. When PSO is initialized it is done so with a group of random particles (solutions) and then searches for optima by updating generations. The algorithm is iterative and the locations will change at each time step. In addition, each particle will record the location of its 'best position'. In every iteration, the particle (P) is updated by two best values. The first best value is the best solution (fitness) achieved so far among the closest particles in the neighbourhood, where the fitness values are stored during the process up to the current

51

iteration—this is known as the local best particle or p$_{best}$ (p_i). The other best value is the global

best or g$_{best}$ (p_g) which represents the best fit position at that moment among all the particles in

the population (Bai 2010; Dian et al. 2011; Liang et al. 2006; Sabat et al. 2011; Sedighizadeh &

Masehian 2009). After finding these two best values, the algorithm then updates the position of

each particle iteratively through the process, defined in Section 3.4. Figure 3.1 (b) shows the

visualization of the PSO vector components during the update process. The updated position is

the result of a summation for the basic vectors of the current position, local best vector, and

global best vector (Blum & Li 2008).

(a) Swarm search technique for the particle local and global best.

(b) Particle's vector update.
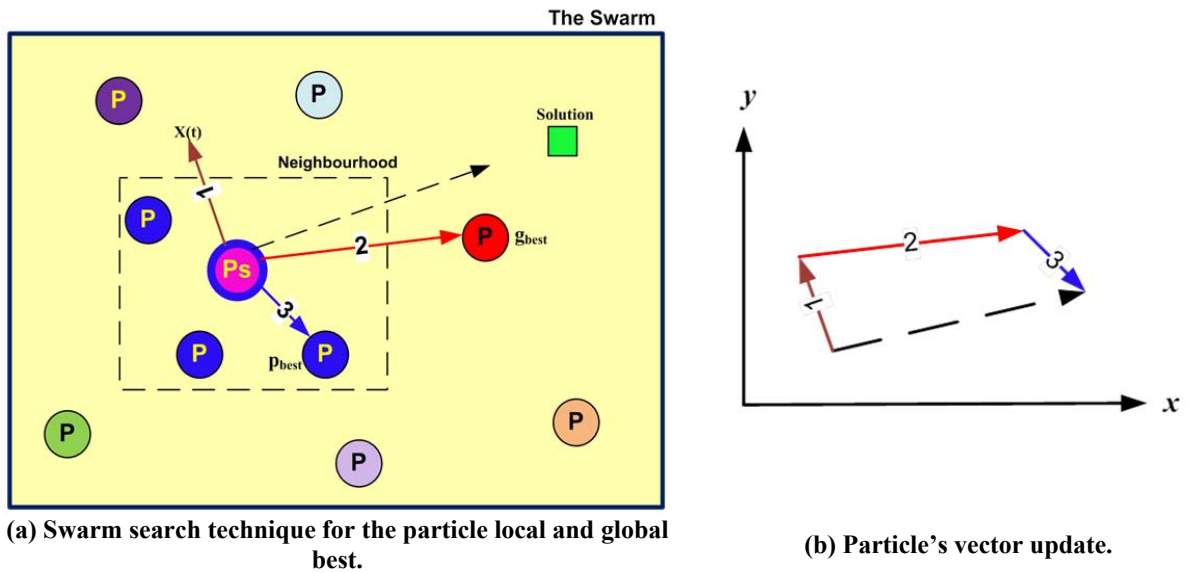
Figure 3.1: Principles of Swarm Intelligence.

3.3 Magnetometer Calibration Technique

A calibration technique based on PSO technique is presented in the current work (Ali et al.

2012a; Ali et al. 2011). There are a number of reasons for why a PSO-based technique would be

used over other well-known estimators such as the Kalman filter. The following list outlines the drawbacks of using the latter method: (Siddharth et al. 2011):

- A prior knowledge of initial states is required.

- Inaccurate knowledge of noise statistics (Process Noise/state Covariance).

- Matrix implementation, especially, inversion operation which may lead increased computation time and leads to singularity.

- Higher uncertainty of heading initialization.

Furthermore, the PSO algorithm has an advantage over other optimization techniques since it has no need for linearization and fast convergence. Additionally, the PSO has been proven to be stable and efficient in noise optimization problems (Pan et al. 2006; Parsopoulos & Vrahatis 2001) which makes it suitable for the magnetometer calibration process.

Dealing with low cost magnetometers requires improving the accuracy of raw measurements (Dorveaux et al. 2009). Therefore, the mathematical models should be adequately prepared to take into account the various sources of disturbance. A major part of the magnetic field distortion is produced when the induced permanent unwanted fields from ferromagnetic materials exist in the vicinity of the magnetometer, which create a bias. Another type of distortion is generated by the materials that react with the externally magnetic field. Based on the EMF, the formulation can be stated according to the following mathematical model (Ali et al. 2012b):

$$B = AH + b + \varepsilon \qquad (3.1)$$

Equation (3.1) can be rewritten in the form:

$$H = A^{-1}(B - b - \varepsilon) \tag{3.2}$$

Where

- H is 3x1 estimated EMF vector,

- B is 3x1 magnetometer measured magnetic field vector, $\boldsymbol{B} = \begin{bmatrix} \boldsymbol{B}_x & \boldsymbol{B}_y & \boldsymbol{B}_z \end{bmatrix}^T$

- A is 3x3 magnetometer scale factor matrix, $\boldsymbol{A} = \boldsymbol{daig(\, a_x \quad a_y \quad a_z\,)}$,

- b is 3x1 magnetometer bias vector, $\boldsymbol{b} = \begin{bmatrix} \boldsymbol{b}_x & \boldsymbol{b}_y & \boldsymbol{b}_z \end{bmatrix}^T$ and

- ε is 3x1 magnetometer noise vector, $\varepsilon = \begin{bmatrix} \varepsilon_x & \varepsilon_y & \varepsilon_z \end{bmatrix}^T$

To simplify the mathematical formulation in Equation (3.2), matrix A compensates for the errors due to misalignments, scale factors, and soft iron where b combines biases caused by the combination of misalignments and hard iron. Additionally, the white noise can be ignored as it is not part of the model used for calibration parameters in the estimation process. As such Equation (3.2) can be rewritten as:

$$H = A^{-1}(B - b) \tag{3.3}$$

In a disturbance free environment, the value of the norm of the measured magnetic field components should be equal to the reference value of the EMF. Consequently, the bias and scale factors are estimated and subject to the objective function as represented in Equation (3.4)

$$H_m^2 - \|H\|^2 = H_m^2 - H^T H = 0 \tag{3.4}$$

Where H_m is the true reference magnitude of the Earth's magnetic field in a given geographical location (which can be obtained from the IGRF model). Every five years, the International

54

Association for Geomagnetism and Aeronomy (IAGA) revises and updates the IGRF parameters. The user is required to input the latitude, longitude and height of the place where the Earth's magnetic field intensity is sought. The 11th generation IGRF accepts years ranging from 1900 to 2020. The accuracy of the reference value based on this model is within *10 (nT) Nano Tesla*; more details about IGRF-11 in (Finlay et al. 2010).

The proposed technique has been adapted to achieve a real time performance. Both magnetometer and gyroscope data are utilized to perform the calibration process. This process requires that the gyroscope data is used to detect the range of the manoeuvring movement and distinguish between the static and motion states. The user is asked to perform the manoeuvring movement for about 20 seconds so that the magnetometer data will be patched for the calibration process. The proposed technique consists of three main parts as shown in Figure 3.2.
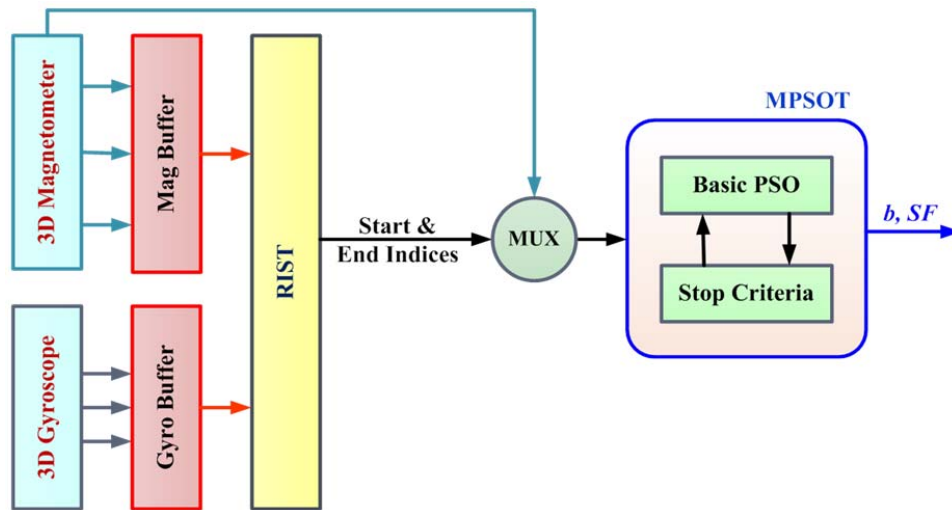
Figure 3.2: Schematic diagram for the PSO based calibration scheme

The first part is the basic PSO based calibration algorithm which estimates the bias and scale factor values. To optimize the operation, a second part is added to select the effective range of

the magnetometer measured data during the manoeuvring movement. This part is called the Region of Interest Selection Technique (RIST) which returns the start and end indices. The output of this part is the actual input for the calibration algorithm. The third part is a modification of the basic PSO algorithm to accelerate the convergence of the estimated parameters. This is referred to as the Modified PSO Technique (MPSOT). Each of these parts will be explained in further detail in the following section.

3.3.1 Basic PSO Based Calibration Algorithm

The proposed algorithm is used to estimate the bias (b) and scale factor (SF) values of the magnetometer measurements by minimizing the difference between the measured and the reference values of the EMF. The proposed method is best suited for problems of a non-linear and non-Gaussian nature (Ali et al. 2012b). This consideration also becomes important since in most cases there is no prior knowledge about the nature of the external fields corrupting the magnetometer's signal. PSO is a better choice to circumvent these difficulties, and is employed extensively to solve complicated design optimization problems as they can handle both discrete and continuous variables in addition to non-linear objective and constrained functions without the computation of a gradient (Alonso & Shuster 2002). Three bias and three scale factor terms corresponding to each axis of the tri-axial magnetometer are estimated, which constitute the six elements of the state vector.

To define the ith position and velocity of the particle as $x_i = (x_{i1}, x_{i2}, ..., x_{iD})$ and $v_i = (v_{i1}, v_{i2}, ..., v_{iD})$ respectively for a swarm of N particles and a search space of dimension D, the PSO algorithm is performed:

$$v_i^k = w.v_i^{k-1} + c_1 r_{i1}^{k-1}(p_i^{k-1} - x_i^{k-1}) + c_2 r_{i2}^{k-1}(p_g^{k-1} - x_i^{k-1}) \tag{3.5}$$

$$x_i^k = x_i^{k-1} + v_i^k \tag{3.6}$$

Where

- k is the index of the current, new, iteration and $k-1$ refers to the previous, old, iteration.

- $i = 1, 2, ..., N$ where N is the size of the population, number of particles,

- c_1 and c_2 are acceleration coefficients,

- r_{i1} and r_{i2} are random numbers uniformly distributed within the range [0, 1].

- w is inertial weight factor, and the bigger the value of w, the wider is the search range.

Equation (3.5) is used to estimate the update of change in position, velocity, of the ith particle while Equation (3.6) provides the new updated position. The standard values for w, c_1, and c_2 to be 1, 2, and 2, respectively are used as fixed values during this process. These parameters are set according to different groups of values where they are found to provide the best performance for the PSO algorithm in its current application. For more information about selecting of the different parameters in the PSO algorithm please refer to (Pedersen 2010; Shi & Eberhart 1998). The error in the magnetic field magnitude ΔH is given by comparing the norm of calibrated of magnetic field (H) with the reference value in a certain area (H_m).

$$\Delta H = H_m^2 - H^T H \tag{3.7}$$

$$Fit\_Value = \sum_{i=1}^{N} (\Delta H_i)^2 \qquad (3.8)$$

Where N is the number of samples.

The performance of each particle is measured according to a fitness function, which is problem-dependent. In optimization problems, the fitness function is usually identical to the objective function under consideration. Equation (3.8) shows the applied fitness function is the difference (error) between the estimated value of the total magnetic field and the reference value. The reference value is 170 *mGauss* in the case of 2D calibration while 570 *mGauss* is for the 3D calibration case. These reference values are obtained from IGRF for the city of Calgary (Finlay et al. 2010). The fitness value is computed as the square root of the summation of the squared error.

The algorithm re-evaluates the locations of all particles' after each iteration and receives the new best values. To determine the optimum value, a recurring searching process is performed until the maximum iteration number is reached or the minimum error condition is achieved. The PSO general computational steps are shown in Figure 3.3.
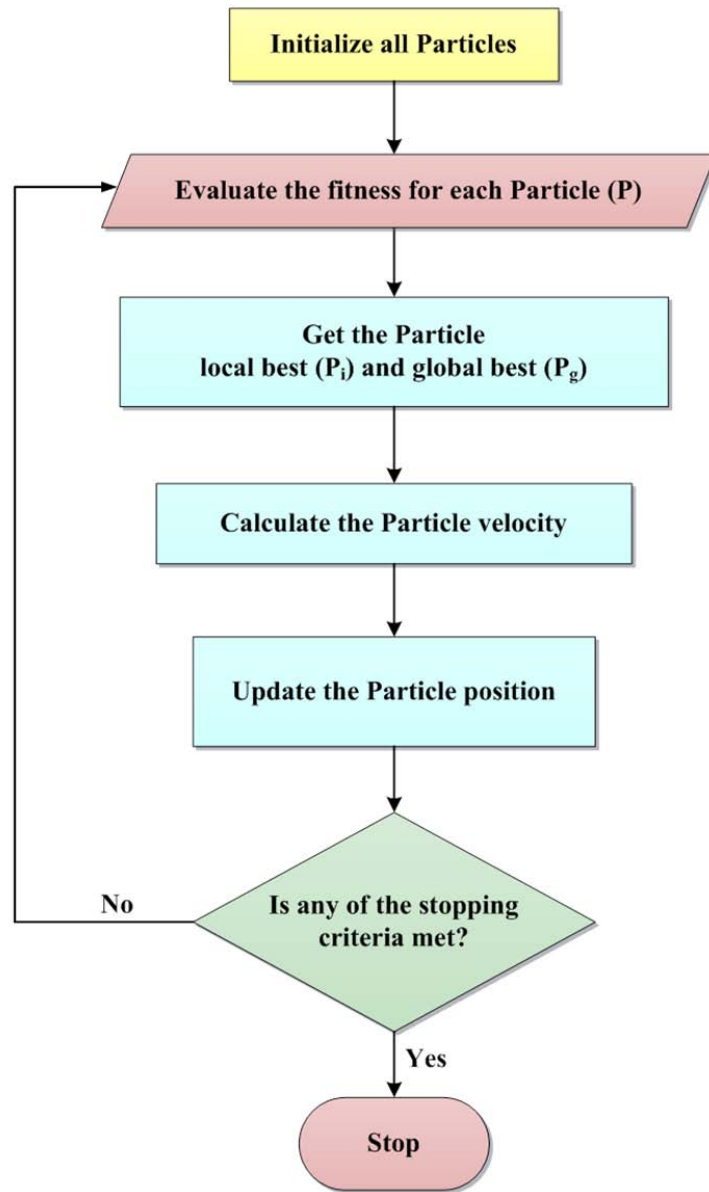
Figure 3.3: The basic PSO algorithm.

The main objective of the proposed technique is to estimate the values of the scale factor and bias respectively according to Equation (3.8) where $SF = \begin{bmatrix} a_x & a_y & a_z \end{bmatrix}^T$ and $b = \begin{bmatrix} b_x & b_y & b_z \end{bmatrix}^T$.

3.3.2 The Range of Interest Selection Technique (RIST)

In all previous research on the calibration of magnetometers, a range of interest selection for the measurements was not taken in account. In order to make the calibration procedure more efficient, the appropriate range of the signal from the entire dataset is extracted and processed. The RIST is used to select the most effective part of the raw data which will be used during the calibration process.

The proposed technique searches for the maximum change in the magnetic field for each axis and acquires the interval in between. The algorithm receives the overall raw measurements and returns the start and end indices of the nominated interval as shown in Figure 3.4. The selection operation is based on detecting the maximum and the minimum signal amplitude in the raw measurements. Based on the selected indices, the range of interest is extracted and passed to the calibration algorithm to get the estimated values for *SF* and *b*.
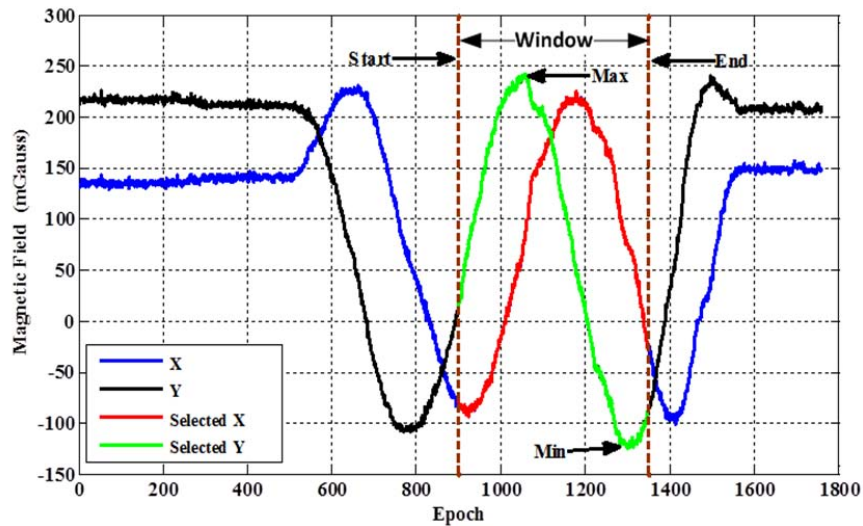
Figure 3.4: The range of interest Selection technique principles.

RIST is important for real time calibration; a typical process for most magnetometer calibration in any PND. In doing so, the calibration algorithm becomes fast, and therefore, fit the real time requirements. To improve upon this methodology, outlier detection may be implemented to achieve greater results by distinguishing between signal max/min arising out of rotation and external disturbance or noise. Enhanced accuracy can take place in the selection of peak values by observing the signal pattern of other sensors. These sensors might be found in the same device (e.g. gyroscopes and accelerometers), which attain a specific pattern during rotation motion as the calibration of the magnetometer requires a full rotation of the sensor on a (horizontal/vertical) plane.

Figure 3.5 shows the first stage of the proposed calibration scheme. The measurements taken from magnetometers and gyroscopes are entered into the RIST so they can be trimmed. The output of the auto-selection algorithm is the beginning and end of a selected range of magnetometer measurement.
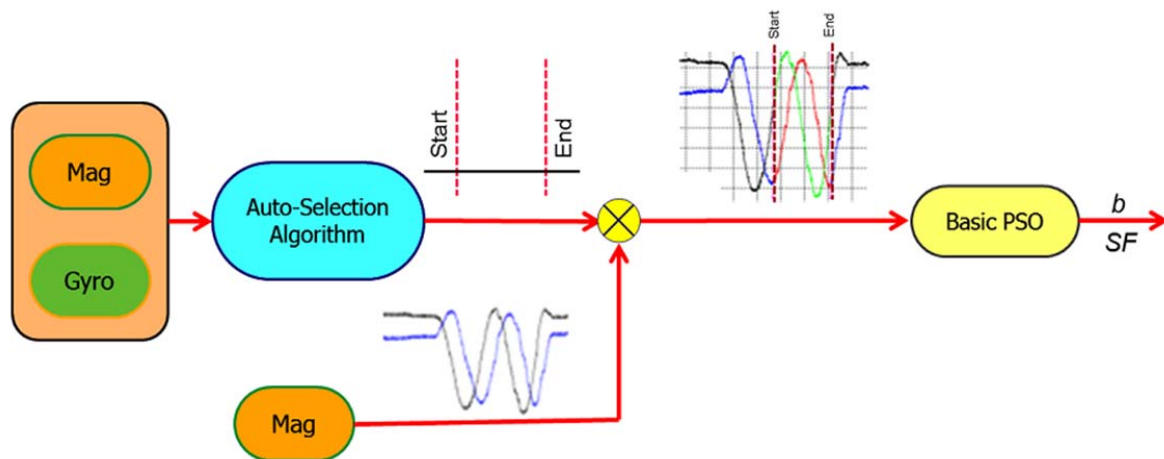
Figure 3.5: The RIST algorithm.

61

The embedding of RIST to the scheme means fewer samples have to be processed during the calibration step. As a result, the total time of the calibration process is reduced and improves power consumption on consumer devices.

3.3.3 Modified PSO Technique (MPSOT)

The PSO algorithm is based on an iterative process to reach optimum solution. This algorithm uses an iterative process to estimate b and SF. Over the iterations, these values converge to the best values and then the process is terminated. The purpose of MPSOT is to create new criteria to terminate the estimation process. To reduce the processing time, the basic PSO algorithm is modified by creating termination criteria for the calibration process seen in Figure 3.6. The stop criteria requires that the following three factors exist:

- A maximum number of iterations.
- A minimum error value.
- Change in bias and scale factor values becomes less than a threshold of 0.01 for consecutive iterations.
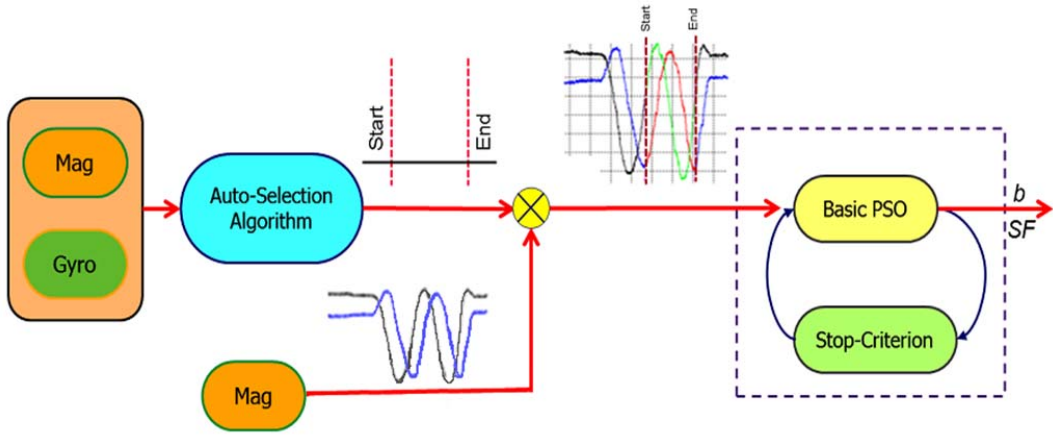
Figure 3.6: The MPSO based calibration algorithm.

Once the convergence is reported by the termination criteria, the requirement of more iterations or process time is redundant, thereby improving the efficiency of the algorithm and reducing the time-complexity.

3.4 Test and Discussion

To assess the performance of the proposed calibration technique, a group of field tests were conducted. The tests include data collection for static, walking, indoors and outdoors modes of operation. For 2D calibration, the magnetometer was rotated $360°$ in the horizontal plane while the heading was computed using the magnetometer-calibrated measurements based on the estimated b and SF. The 3D test was conducted by rotating the device about the three axes in the vertical and horizontal directions.

A description of the results can be found in the next section, where the basic PSO algorithm is first applied using the entire dataset of the magnetometer measurements in the parameters

estimation process. First, with the basic PSO there is no modification to the core of the algorithm. Secondly, the application of RIST illustrates where a range of interest in the dataset is selected for use rather than the entire dataset, as described in Section 3.2. Third, the MPSOT is used when a significant change is applied to the core of the basic PSO algorithm. Finally, the effect of the proposed modification on the PSO processing time performance is discussed.

3.4.1 2D Calibration Scenario

2D calibration tests conducted by maintain the PNS in the horizontal plane. The total magnetic field is calculated in the horizontal frame (X-Y) and tests are performed in the multi-sensors lab at the University of Calgary using the rotation table shown in Figure 3.7.

Figure 3.7: Rotation table

Tests include two 360-degree turns around the z-axis using a rotation table to ensure that the device is held in the horizontal plane. Both *b* and *SF* values are estimated by passing the magnetometer readings to the basic PSO algorithm.

3.4.1.1 Basic PSO Results

Figure 3.8 shows the results for the basic PSO where "Raw" and "PSO" terms refer to the calculated magnetic field using the raw measurements and the calibrated data respectively. Figure 3.8 (a) shows the raw magnetic field in the *X* and *Y* directions, while the total horizontal magnetic field is shown in Figure 3.8 (b). The calibrated readings show the constancy of the estimated magnetic field, which is approximately the reference value of the EMF. Figure 3.8 (c) shows the resulted track after calibration where the two 360-degree turns around the z-axis are calibrated and adjusted around the origin in the shape of circles based on the values estimated by the Basic PSO algorithm.
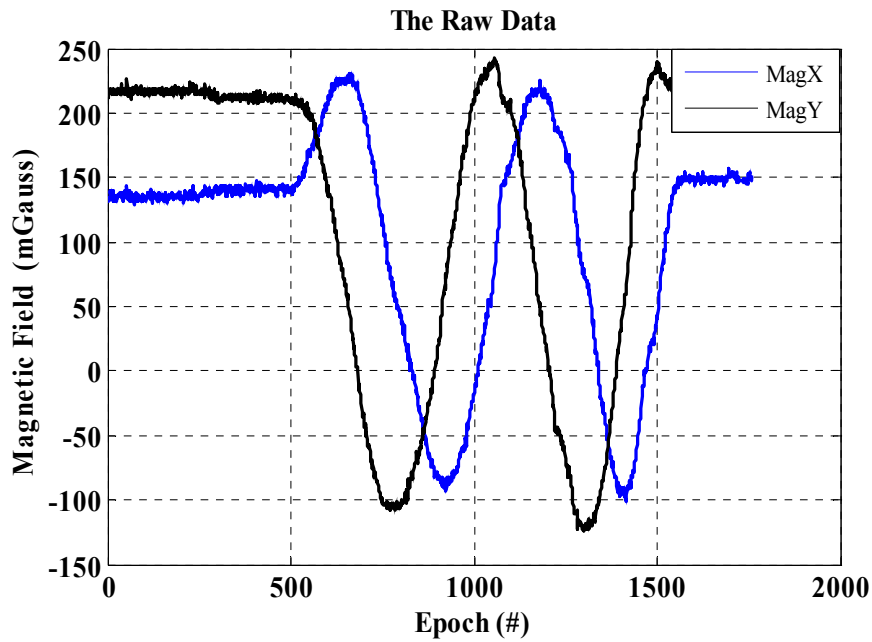
(a) Raw magnetic field readings.
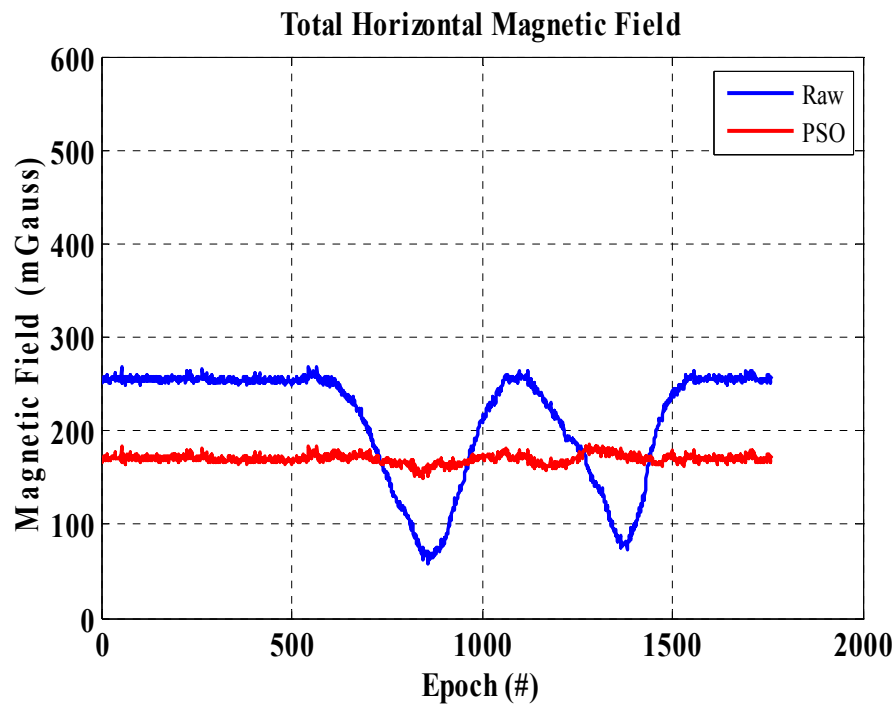
(b) Horizontal raw and PSO calibrated magnetic field.
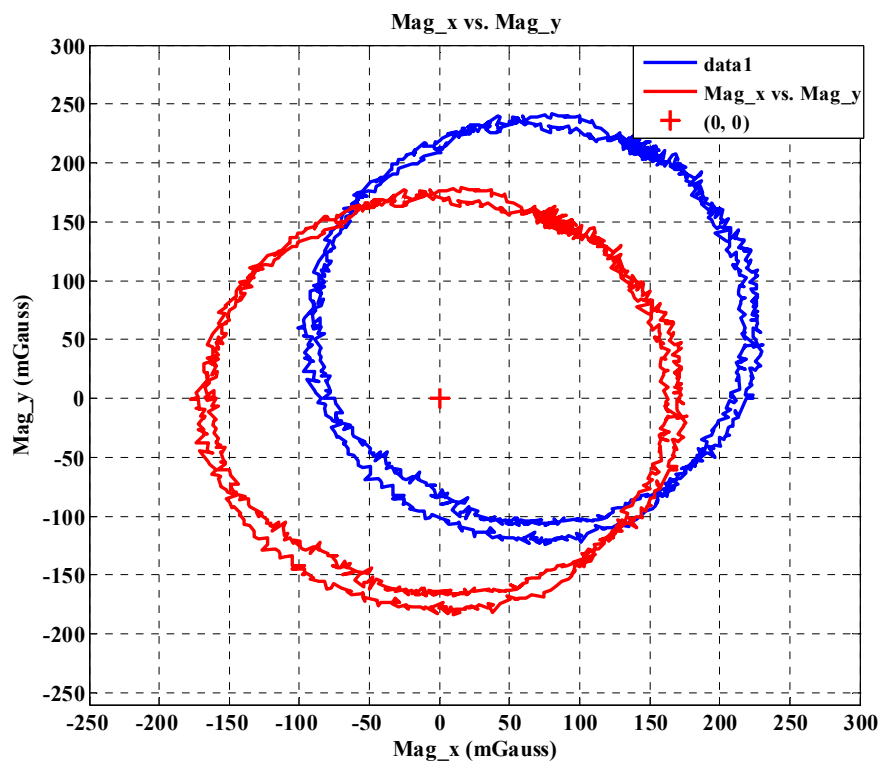
(c) 2-D calibration for adjusted magnetic field.

Figure 3.8: Standard PSO based 2D calibration

66

3.4.1.2 RIST Results

In this section, the impact of applying RIST to reduce the time required for estimating b and SF values is observed. The number of samples is compared the entire dataset and the range of interest (part of the data). Figure 3.9 shows the compared results where the total number of samples decreased for all cases. For example, 1240 samples (all the measured data) are used in Test1; however, applying RIST reduces the number to just 279 samples. As a result of this decrease, the time required to perform the calibration process is also decreased.
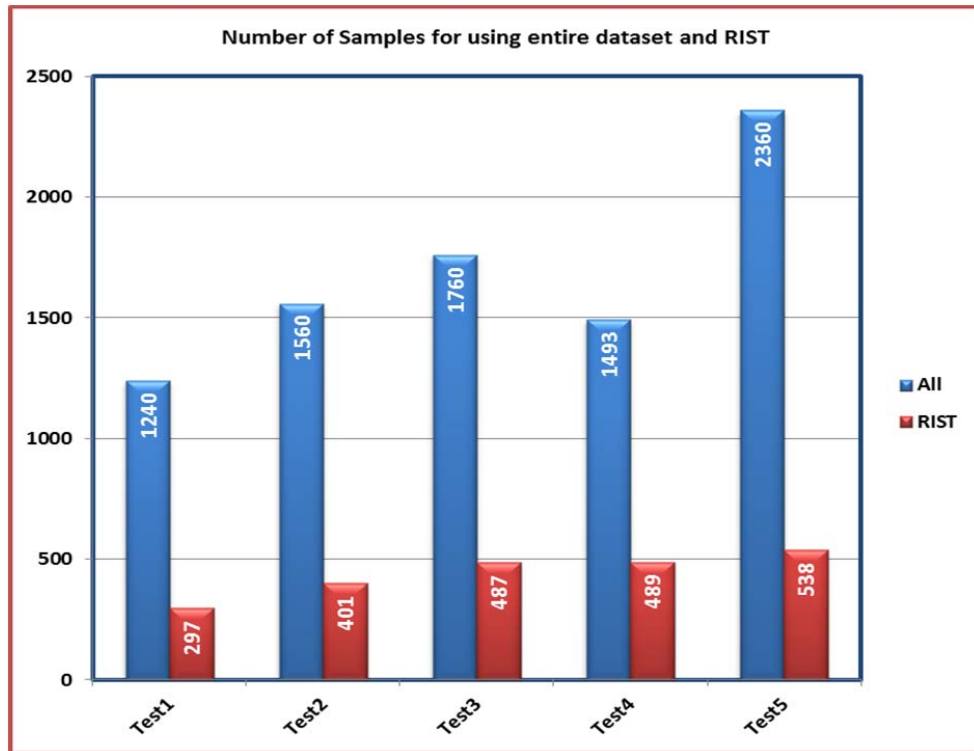
Figure 3.9: Number of applied samples in 2D calibration.

Although less information is fed to the PSO algorithm, the accuracy of the results has not been affected, as indicated in Table 3.1 where the values of **SF** and **b** are close in all tests and in both

cases. Therefore, the results gathered from the PSO, with the entire dataset and with RIST, behave almost identically.

Table 3.1: Comparison of calibration parameters in 2D calibration.

	X Scale Factor		Y Scale Factor		X bias (*mGauss*)		Y bias (*mGauss*)	
	All	RIST	All	RIST	All	RIST	All	RIST
Test1	0.873	0.866	0.998	0.973	87.279	87.419	54.190	50.008
Test2	0.601	0.598	0.655	0.649	33.490	32.674	42.887	42.193
Test3	0.925	0.913	1.018	1.050	66.016	63.461	61.332	58.556
Test4	2.498	2.535	2.720	2.773	36.912	50.207	42.229	51.725
Test5	0.791	0.793	0.872	0.869	19.483	19.986	42.121	43.142

3.4.1.3 MPSOT Results

To demonstrate the final impact of the proposed algorithm, both RIST and MPSOT were fused together in the calibration process. In this scenario, the entire dataset was applied to RIST to produce the range of interest for the dataset. Then, the MPSOT was applied to reduce the number of iterations required to converge by the algorithm. Figure 3.10 provides a comparison between the number of iterations, which the algorithm consumes to converge when using the basic PSO, and its modified version, MPSOT.
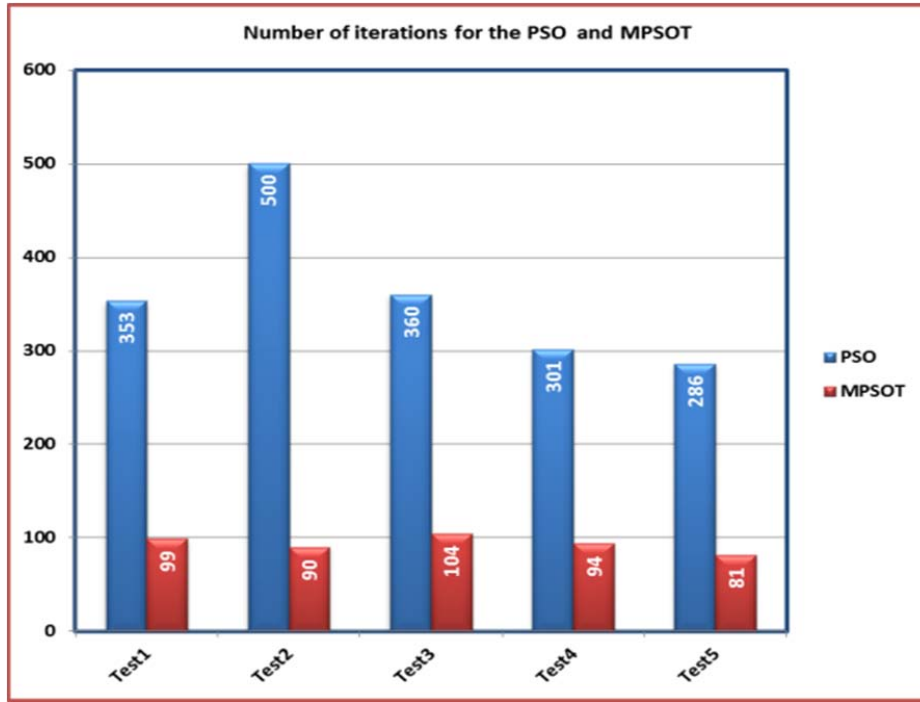
Figure 3.10: Number iterations basic PSO and MPSOT in 2D calibration.

The comparison establishes that the number of iterations decreased in most cases by 1/3 when MPSOT is applied. Without doubt, the values of *SF* and *b* were unaffected, as illustrated in Table 3.2.

Table 3.2: Comparison of PSO and MPSOT in 2D calibration.

	X Scale Factor		Y Scale Factor		X bias (*mGauss*)		Y bias (*mGauss*)	
	PSO	**MPSOT**	**PSO**	**MPSOT**	**PSO**	**MPSOT**	**PSO**	**MPSOT**
Test1	0.858	0.863	0.982	1.027	85.615	86.025	50.381	46.695
Test2	0.597	0.602	0.649	0.629	32.659	29.96	42.003	43.227
Test3	0.913	0.911	1.05	1.049	63.563	62.955	58.489	58.503
Test4	2.534	2.535	2.773	2.773	50.356	50.162	51.822	51.59
Test5	0.787	0.775	0.856	0.859	18.75	16.295	40.415	47.76

3.4.2 3D Calibration Scenario

To examine the performance of the proposed technique in 3D space calibration, six different tests were conducted. During these tests, the device was moved freely in the space; in fact 3D calibration is more convenient for the user when the device is not held in the horizontal plane. The total magnetic field was calculated when the reference value of the total EMF reached 570 *mGauss*. The algorithm received data from the 3-axis magnetometer.

Figure **3**.**11** illustrates the calibration results for the magnetic field sensors, where both the un-calibrated and calibrated magnetic fields are plotted in 3D. The mesh globe outlines the expected 3D magnetic field, which differs significantly from the one that was measured in the un-calibrated version. After calibration, the measured field components coincided with those that were expected, thereby proving a successful calibration.

(a) Raw data   **(b) Calibrated data**
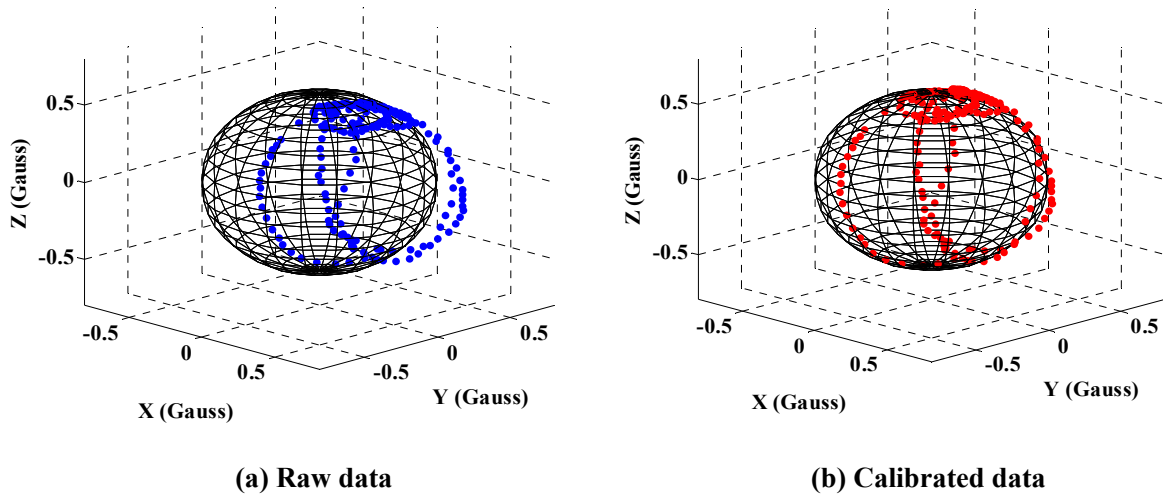
Figure 3.11**: 3D PSO magnetic field sensors calibration.**

3.4.2.1 RIST Results

Figure 3.12 shows the comparison between the number of samples in both cases using the entire dataset and the region of interest.
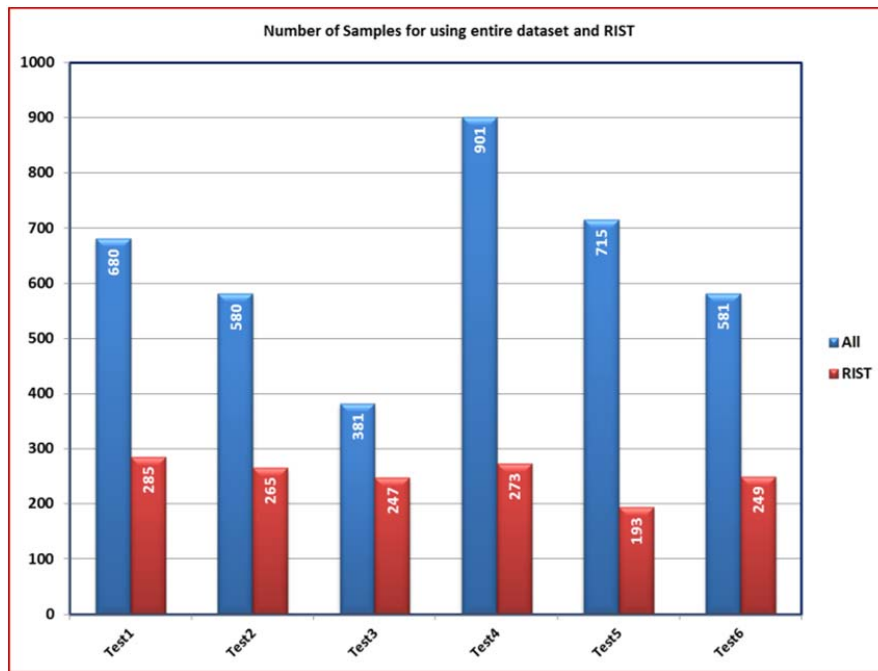
Figure 3.12: A comparison between the numbers of samples applied for magnetometer calibration in case of using the entire dataset and RIST in 3D calibration.

Error! Reference source not found. indicates no significant change in *SF* and *b* values and the results confirm the validity of the proposed calibration technique even with a fewer number of observations. Much like the previous case in 2D calibration, a comparison of the RIST results highlights the benefits of the proposed technique for calibrating the magnetometer.

Table 3.3: Magnetometers parameters resulted from using the entire dataset and RIST in 3D calibration.

	X Scale Factor		Y Scale Factor		Z Scale Factor	
	All	**RIST**	**All**	**RIST**	**All**	**RIST**
Test1	1.0371	1.0325	1.1141	1.0985	0.9394	0.9317
Test2	1.0479	1.0465	1.1003	1.1014	0.9364	0.9384
Test3	1.0153	1.0158	1.0895	1.0860	0.9318	0.9324
Test4	0.9136	0.9249	0.9761	0.9718	0.8453	0.8541
Test5	0.9286	0.9248	0.9817	0.9859	0.8368	0.8460
Test6	0.9454	0.9311	1.0169	1.0167	0.8733	0.8674

(a) Scale factor values

	X bias (*mGauss*)		Y bias (*mGauss*)		Z bias (*mGauss*)	
	All	**RIST**	**All**	**RIST**	**All**	**RIST**
Test1	38.1795	40.0139	30.8485	38.8051	135.8694	128.0139
Test2	36.3021	35.7039	34.2721	33.6313	135.5421	134.6297
Test3	40.3624	38.9419	37.8209	36.4251	134.4415	134.2701
Test4	28.4165	16.2188	46.2673	53.2383	121.8317	114.8561
Test5	34.5628	34.1847	58.8522	58.1043	129.9453	126.9294
Test6	46.1353	40.1545	33.8024	37.6382	126.3606	128.5436

(b) Bias values

3.4.2.2 MPSOT Results

Figure 3.13 shows the comparison between the number of iterations for the basic PSO and the MPSOT.
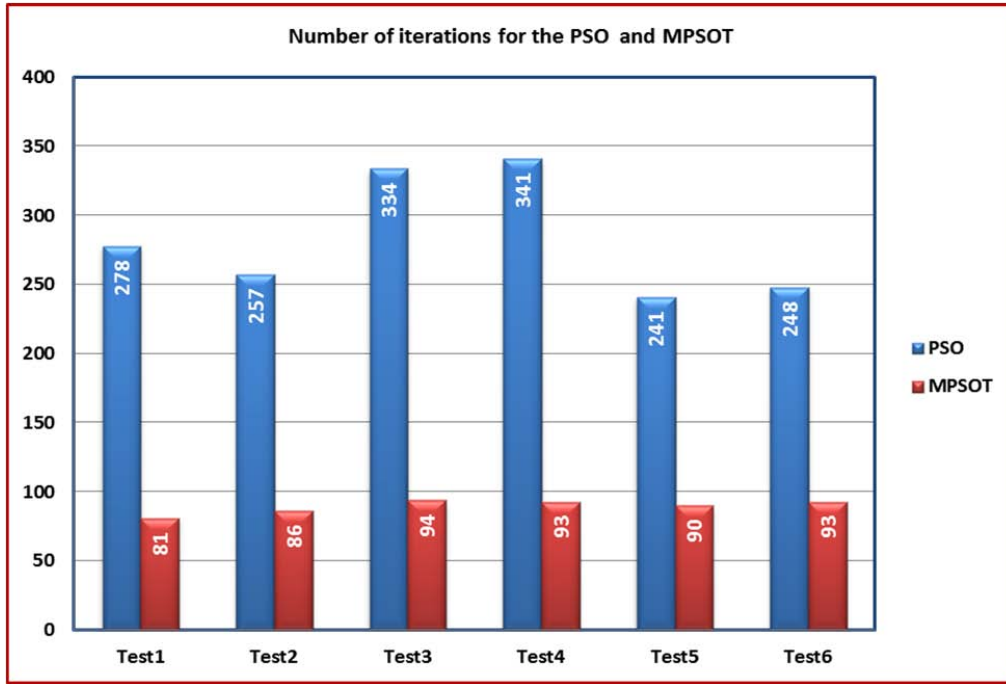
Figure 3.13: A comparison between the numbers of iterations in case of using the basic PSO and MPSOT in 3D calibration.

Table 3.4 presents the different values of *SF* and *b* for both algorithms where the values are close. These results indicate that the MPSOT reduces the time required for the calibration process as in the previous 2D calibration case.

Table 3.4: Magnetometers parameters resulted from using the basic PSO and MPSOT in 3D calibration.

	X Scale Factor		Y Scale Factor		Z Scale Factor	
	PSO	**MPSOT**	**PSO**	**MPSOT**	**PSO**	**MPSOT**
Test1	1.0267	1.0228	1.1643	1.1334	0.9385	0.9515
Test2	1.0485	1.0449	1.0994	1.0998	0.9385	0.9325
Test3	1.0079	1.0082	1.0807	1.0903	0.928	0.9371
Test4	0.9249	0.9152	0.9717	0.9868	0.8539	0.8452
Test5	0.9235	0.9008	0.9812	0.9916	0.8504	0.8608
Test6	0.9227	0.9276	1.0191	1.0281	0.8703	0.8644

(a) Scale factor values

73

	X bias (*mGauss*)		Y bias (*mGauss*)		Z bias (*mGauss*)	
	PSO	MPSOT	PSO	MPSOT	PSO	MPSOT
Test1	40.0418	35.2361	8.1353	23.3182	133.0826	150.0231
Test2	36.1018	25.7854	33.8402	42.4474	134.9986	130.0379
Test3	33.6985	32.2681	32.9084	20.48	135.5549	139.0494
Test4	18.5793	8.9173	51.7038	49.8835	115.2107	128.7535
Test5	32.2353	33.1784	59.1892	49.9255	127.8947	126.5982
Test6	38.1294	36.6339	31.4223	28.0506	130.0527	119.8037

(b) Bias values

The innovative features of the proposed PSO-based magnetometer calibration technique can be summarized as the following:

- It accounts for unexpected terms - that may be neglected - to simplify the objective function.

- It makes no assumptions for the magnetic deviation.

- The magnetometer measurements are calibrated directly without estimating the geometrical proprieties of the ellipsoid (rotation, translation and lengths of the semi-axes).

3.4.3 2D Calibration bias and scale factor convergence

This section describes the effect of the modification in the PSO algorithm in the required time for the calibration process. Figure 3.14 provides the results of the comparison between the calibration process using standard PSO and the MPSOT. As shown in Figure 3.14, the standard PSO terminates after 309 iterations to estimate the proper bias values while the

74

MPSOT consumes only 108 iterations ($\approx$ 1/3rd) to provide closer bias values to the standard version.

(a) Bias convergence using standard PSO   (b) Bias convergence using MPSOT

(c) Scale factor convergence using standard PSO   (d) Scale factor convergence using MPSOT.
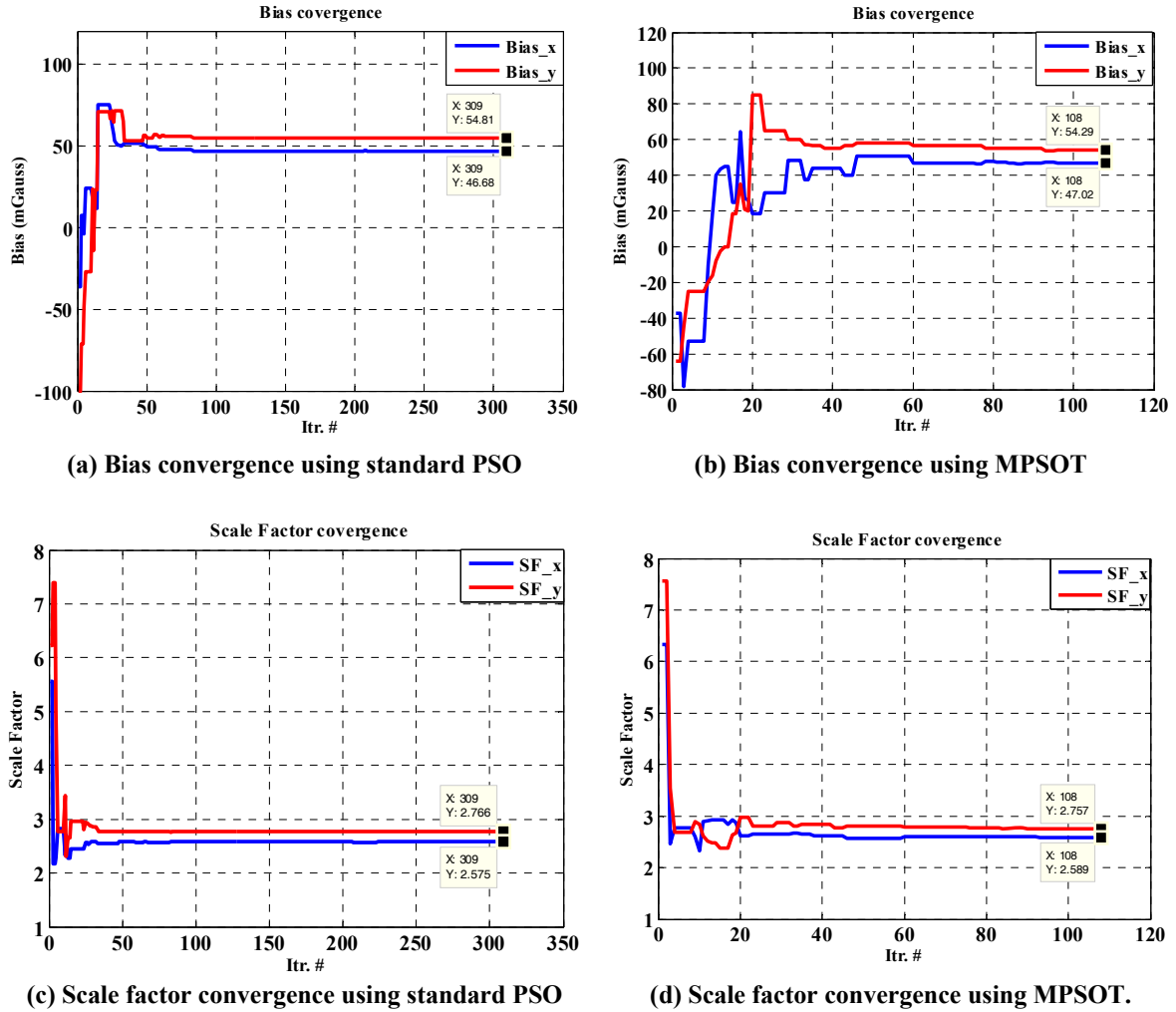
Figure 3.14: The convergence of estimated bias and scale factor values in 2D calibration.

3.4.3.1 3D Calibration bias and scale factor convergence

The results of the comparison between the calibration process using standard PSO and the MPSOT in the scenario of 3D calibration are shown in Figure 3.15. The standard PSO algorithm

takes 310 iterations to converge while the MPSOT takes only 83 iterations to estimate the proper bias values. The ratio between standard and the modified algorithm is ($\approx 1/4^{\text{rd}}$).

(a) Bias convergence using standard PSO (b) Bias convergence using MPSOT

(c) Scale factor convergence using standard PSO (d) Scale factor convergence using MPSOT.
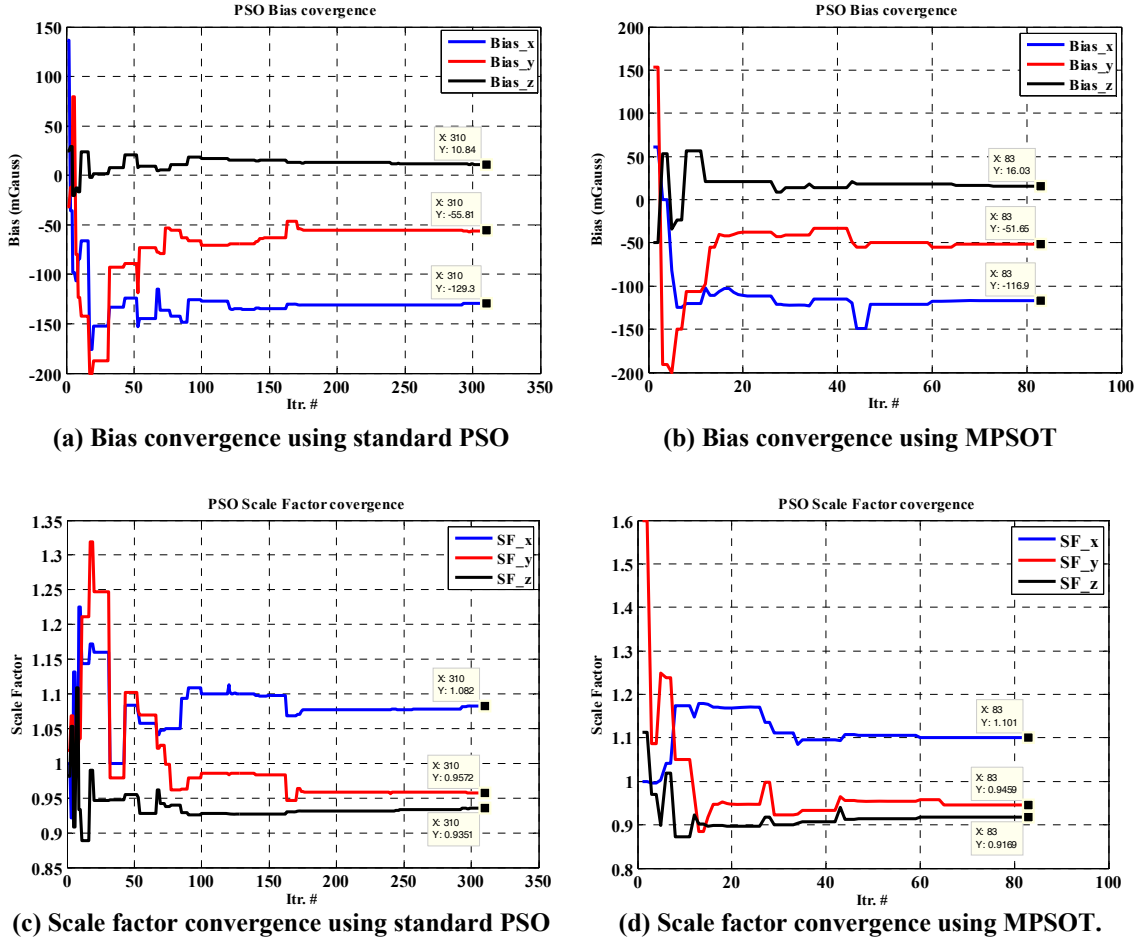
Figure 3.15: The convergence of estimated bias and scale factor values in 3D calibration.

3.5 Comparison between PSO & KF techniques

In this section, the performance of the proposed PSO-based magnetometer calibration technique is compared to the Kalman filter technique.

3.5.1 KF Parameters Conversion

One of the major disadvantages to using the KF technique for magnetometer calibration is the conversion of the bias and scale factor values. Figure 3.16 provides an example for 2D calibration using the KF technique. As shown in the figure, the values diverge and fail to indicate an appropriate termination for the calibration process.
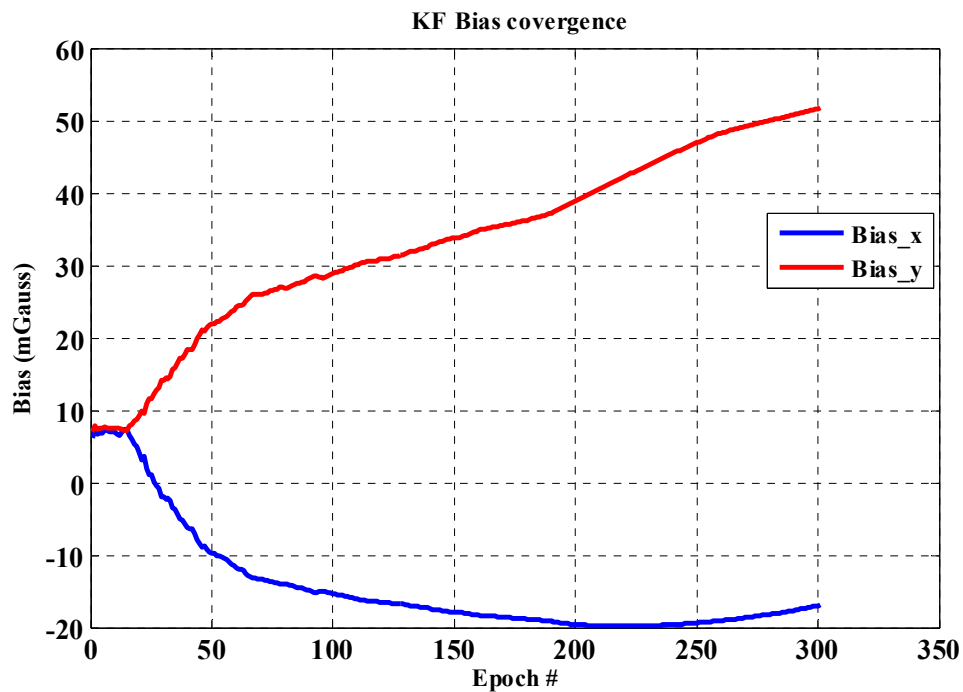
(a) Bias convergence
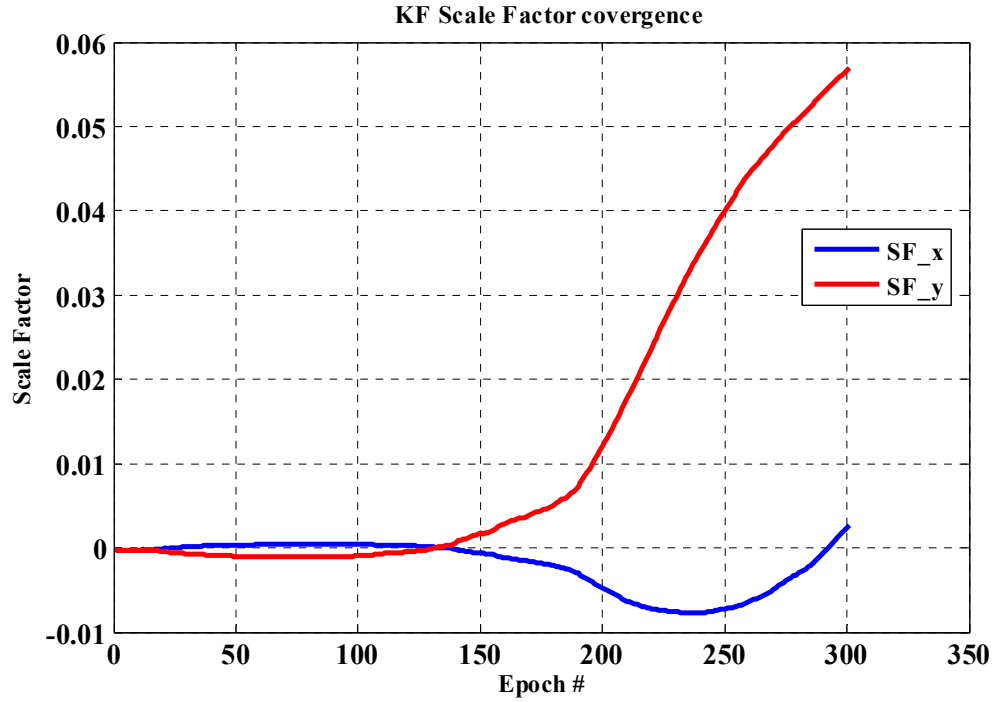
(b) Scale Factor convergence

Figure 3.16: KF-based calibration parameters convergence.

3.5.2 2D Calibration

For comparisons purposes, two types of tests were conducted for the 2D scenario. The first test included a hand rotation applied to the device in the horizontal plane, ensuring that rotations were sensed about the horizontal frame, x and y, axes of the device. The test was conducted outdoors.

As evidence by Figure 3.17 (a), the PSO successfully estimates bias and scale-factor errors while KF fails to converge for the correct values as shown. The correct heading values should change from 250° to 250° again as the device is rotated one circle in the horizontal plane around z-axis.

Where the KF-based heading yields different values with errors caused by improper calibration processes, the PSO-base estimated heading follows the correct heading values as seen in Figure 3.17 (b).
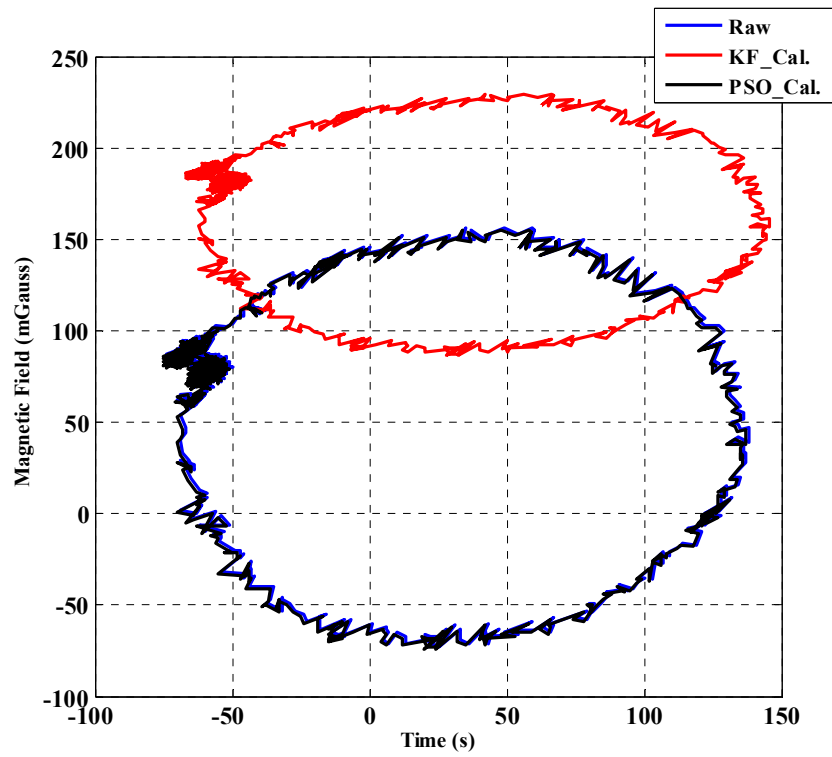
(a) Mag_x vs Mag_y
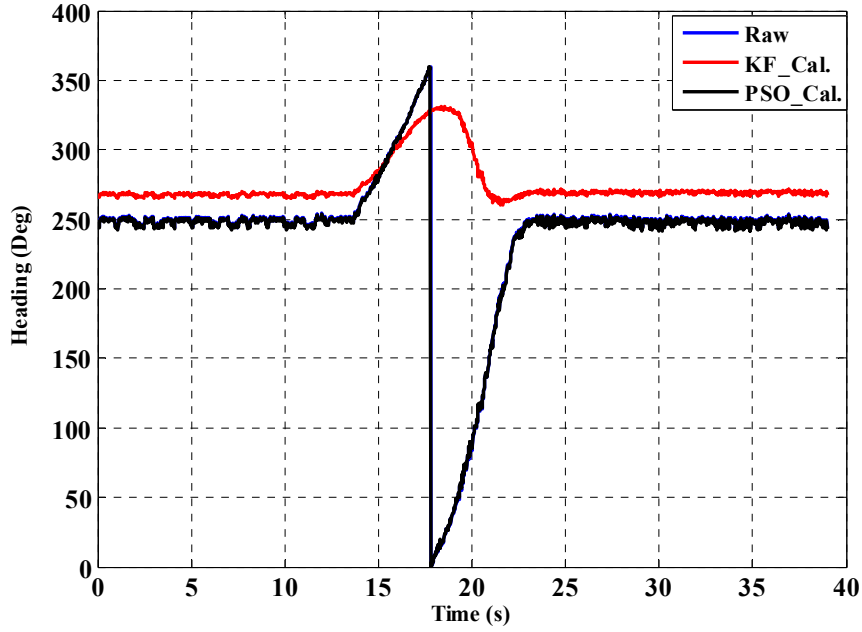
(b) One 360 degrees turn around z-axis and corresponding estimated heading.

Figure 3.17: A comparison between PSO and KF calibration techniques performance.

For the second type of test, a typical lab environment with even more dense magnetic structures was chosen. 2D rotation of the module was performed using a rotation table about the vertical z-axis. The results are shown in Figure 3.18. The bias and scale-factor errors shift the circle from the origin and skew the circle to form an ellipse The PSO works well to estimate this bias and scale-factor error while the KF fails however, to estimate the correct scale factor value as shown in Figure 3.18 (a) since the calibrated data shape is an ellipse and not a circle. The total magnetic field is expected to be around 170 *mGauss* after calibration. As shown in Figure 3.18 (b), the PSO algorithm achieves the closest result to the reference value and has less variation during the calibration movement. Figure 3.18 (c) illustrates the estimated heading for all techniques.
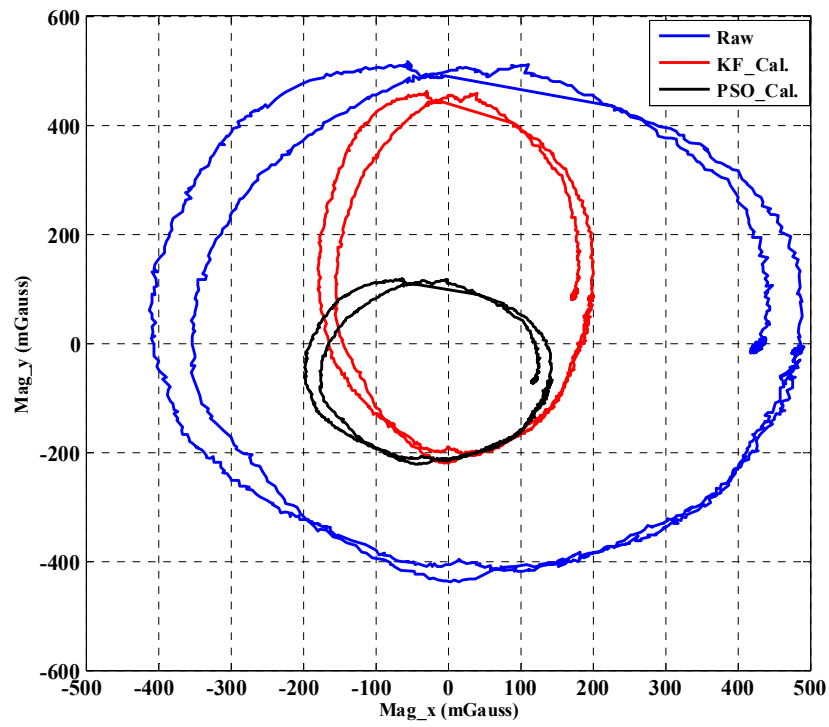
(a) MagX vs MagY
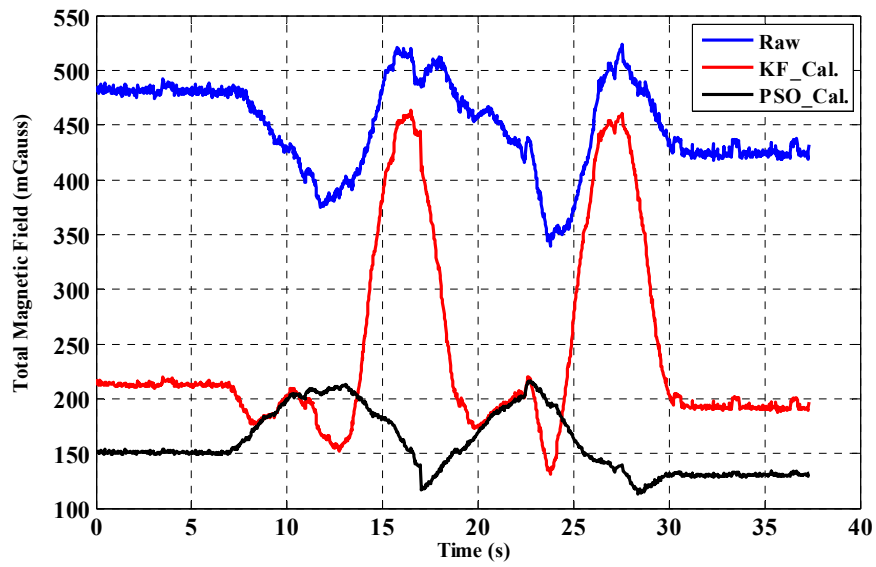
(b) Total horizontal magnetic field

81
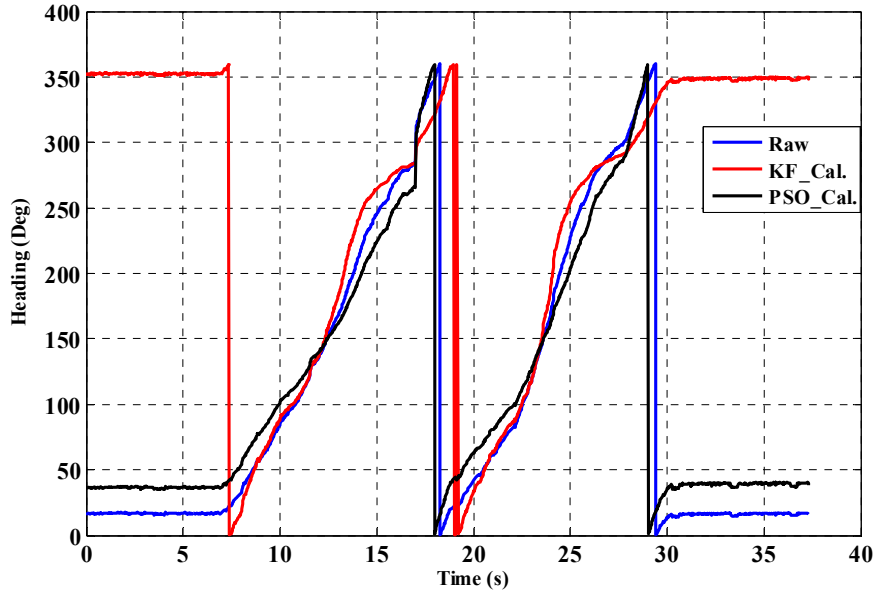
(c) Estimated heading for two 360 degrees turns around z-axis.

Figure 3.18: A comparison between PSO and KF calibration techniques performance for rotation-table motion of the device.

The PSO for both indoor and outdoor scenarios performed well when estimating the bias and scale factors. After a comparison of the outdoor and the indoor results, a higher scale-factor error is determined to have corrupted the magnetometer. This is to be expected since indoor environments contain more ferrous objects than outdoor environments

3.5.3 3D Calibration

To evaluate the performance of the different techniques in 3D space, an outdoor test was conducted in a soccer field, as shown in Figure 3.19 (a). The device was first moved in the space around 3 axes, meaning it, was held in the compass mode during the test. The test began in a south direction at 180°. A complete square was tracked as 180, 90, 0, and 270 degrees. The total

magnetic field is shown in Figure 3.19 (b) as the PSO and KF results are close to the reference value. Figure 3.19 (c) demonstrates that the obtained heading from the calibrated magnetometer readings were close to the reference heading. This can be seen in the heading comparison between PSO-and KF-based calibrated and un-calibrated magnetometer readings.
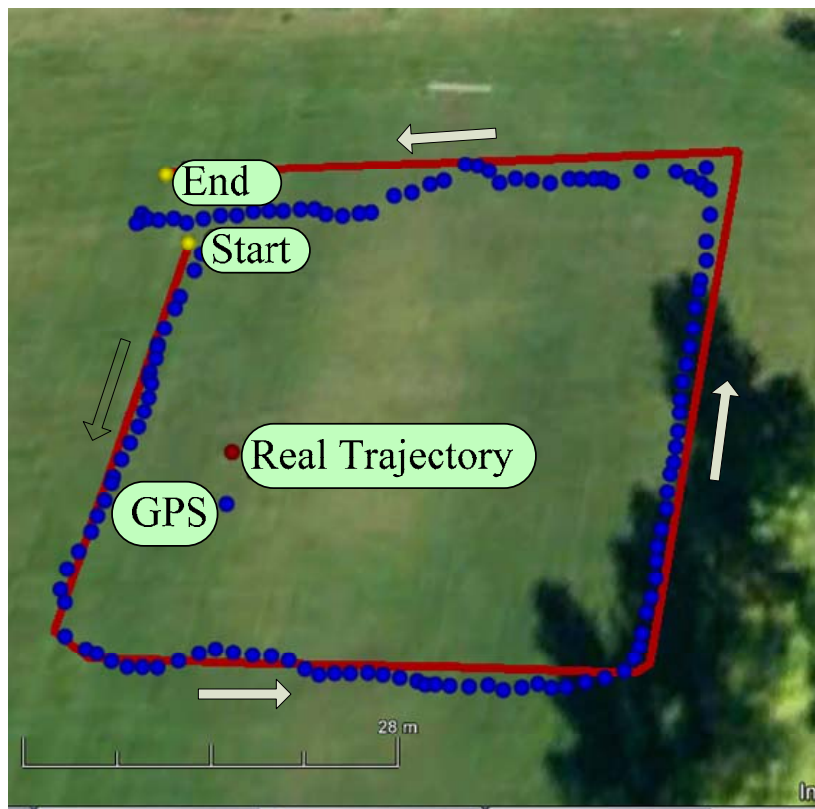
(a) The field test
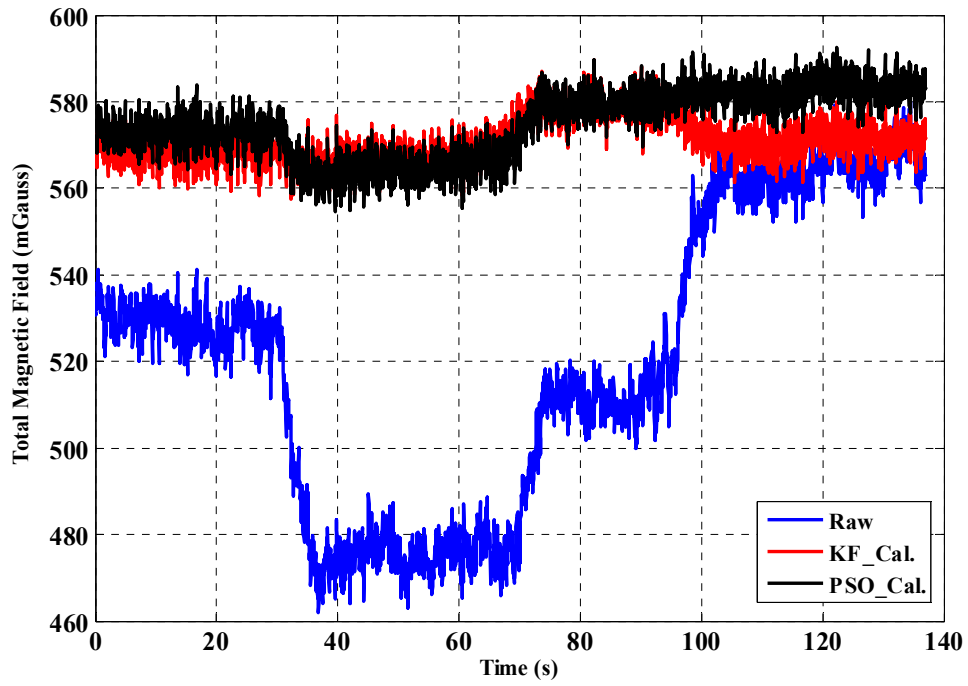
(b) Total magnetic field
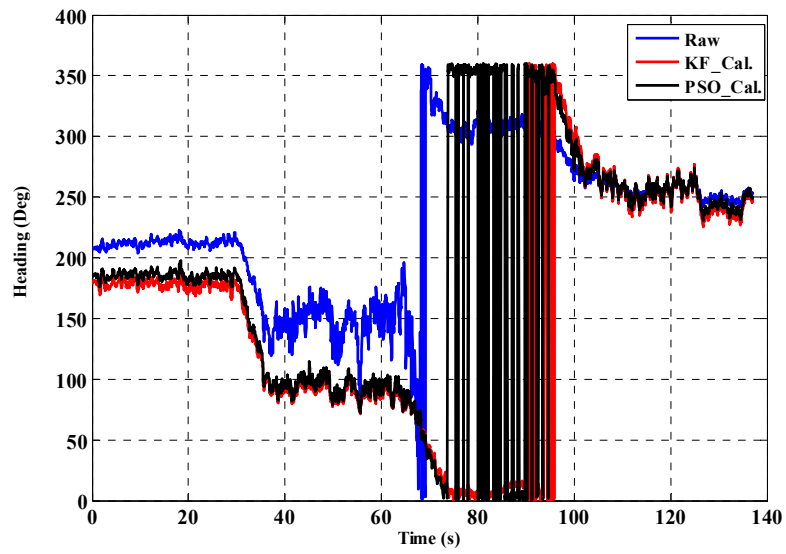
(c) Magnetometer derived walk-heading of the device

Figure 3.19: A comparison between PSO and KF base calibration performance in 3D space with the raw measurement.

84

As mentioned in the previous sections, the objective of the estimation algorithm is to obtain bias and scale-factor values in different environments. By using the proposed formula, it is assumed this is nearly constant and hence the process noise is negligible. Even if a small amount of it were to have any effect it would be modeled by default in the estimated values achieved by using the swarm technique - according to which all effects are modeled as bias and scale factor. The selection of the swarm parameters' values had some influence on the algorithm performance. In this algorithm however, it was determined to be sensitive only to the parameter initialization. The range of the parameter initialization should be investigated from the signal behaviour in order to have the appropriate range for each parameter. However, the PSO was found to be robust against the environment change and many parts of the surrounding objects distortions. The PSO-based calibration technique leads to improved calibration performance and significantly outperforms the KF in harsh conditions.

Chapter Four: Magnetometer Measurement Pre-Calibration and Post-Calibration Analysis

As discussed in Chapter 3, measurements acquired from magnetometers require frequent calibration due to the change in the environment and the surrounding objects. Moving the magnetometer around the different axes significantly affects the calibration process. To improve the performance of the magnetometer in cluttered environments, pre- and post-calibration procedures should be followed (Ali et al. 2013). The pre-calibration process is the movement of the device to affect the magnetic field around the different axes while the post-calibration process involves monitoring and assessing the measured magnetic field to initiate the re-calibration process. In this chapter, efficient manoeuvring modes for pedestrian navigation applications are investigated to calibrate low-cost magnetometers. A magnetometer anomaly detection technique is also proposed for the recalibration process.

4.1 Error Sources in Magnetometer Measurements

Distortion in the magnetic field can occur as a result of different objects in the surrounding environment. Even in well-designed handheld devices, these sources create extraneous fields with high magnitudes. Designers of such devices should not assume that the calibration process will be always correct for a poor layout. Magnetometers' measurements are influenced by several types of errors which can be grouped in one way mathematically (Takahashi et al. 2010). The scale factor can be modeled together with hard and soft iron effects, as they have the same mathematical consequence (Foster & Elkaim 2008). The scale factor and bias therefore become

the main calibration parameters to be considered. Such parameters have a significant effect on the overall performance of the magnetometer and should be corrected (Granziera Jr 2006). The temperature can also be considered as one of the distortion sources for the magnetic field (Titterton & Weston 2004).

However with an efficient calibration technique, there is no need to have a specific method for thermal effect correction as the recalibration process for the different parameters can be sufficient. In general, hard iron effect causes much larger contribution for the resulted distortions. It is important to understand the different effects, of hard and soft-iron, to estimate the appropriate and necessary parameters. The following subsections describe the different source of distortion for the magnetic sensor.

4.1.1 Ideal case without distortions

In the absence of any disturbance on the sensed field, the plot of the measurements in the horizontal plane should form a perfect circle. The circle is centered on the origin, (0, 0), with a radius equal to the magnitude of the magnetic field. Figure 4.1 presents the resulted track from plotting the magnetometer x vs. magnetometer y and rotating the device in the horizontal plane 2 turns at 360° about the z-axis. The result shows a circle around the origin as no distortion effects in the surrounding environment.
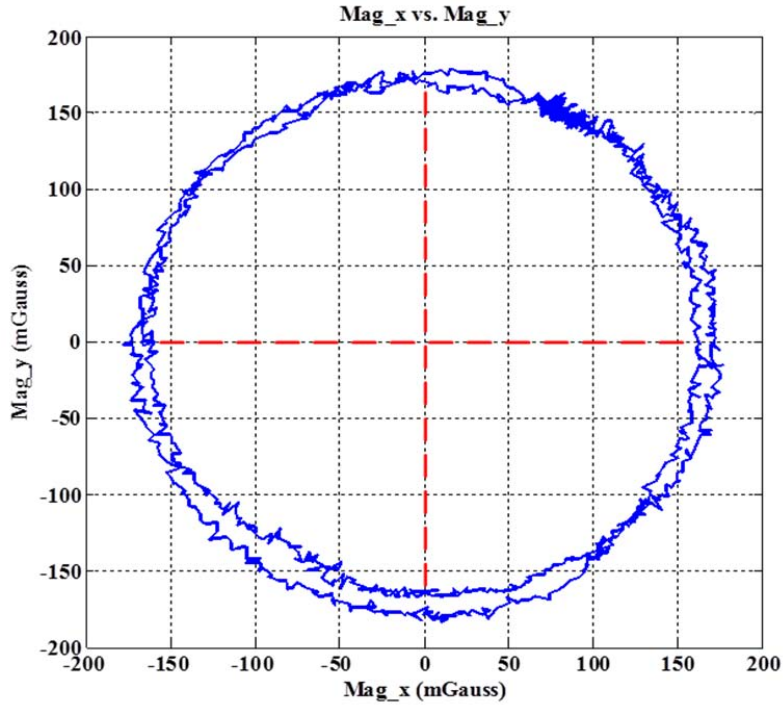
Figure 4.1: Distortion-free magnetometer data.

However, the perturbation in the magnetic field can be produced in the presence of any hard or soft iron effect. The perturbation shifts the center of the data at a point rather other than (0, 0) in the case of hard iron effects while soft iron effects cause the plotted data to appear deformed as the circle shape becomes an ellipse with a different offset angle.

4.1.2 Hard Iron Effect

Hard iron distortions are generated by the objects that produce a constant and additive magnetic field to the EMF. Thus, the generated magnetic field is presented by a constant permanent bias in the output of each magnetometer. The hard iron distortions shift the origin of the produced circle out from (0, 0) as shown in Figure 4.2. The figure shows that the center point is moved to (70,

88

65) which means that there is a 70 *mGauss* hard iron bias in Mag_x's measurements and 65 *mGauss* hard iron bias in Mag_y's measurements. However, the hard iron effect does not change the shape of the circle. Consequently, a compensation for the hard iron distortion is accomplished by estimating the offset in the x and y direction. The estimated values are then subtracted from the measurements. It is important to convert the measured data into the horizontal plane before estimating the hard iron corrections.
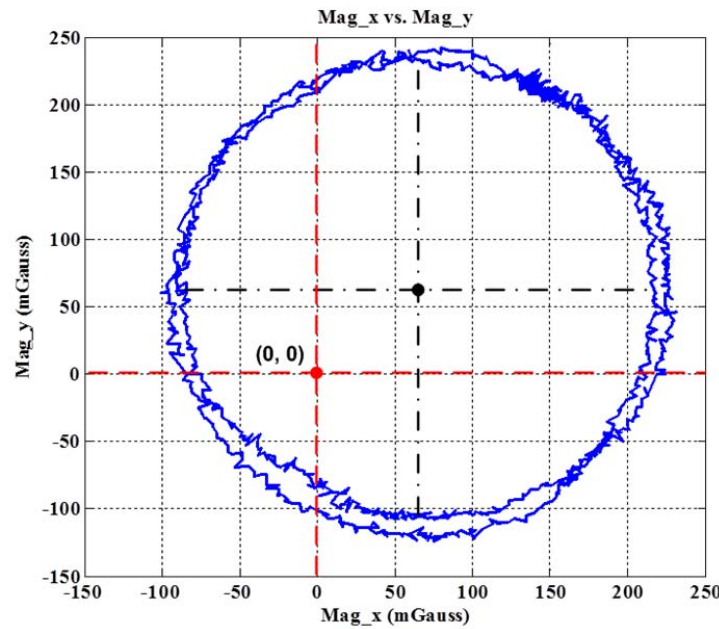
Figure 4.2: Magnetometer data with hard-iron distortion.

4.1.3 Soft Iron Effect

Soft iron effects are caused by the interaction of an external magnetic field with ferromagnetic materials in the neighbourhood of the magnetometer (Vasconcelos et al. 2011). In other words, soft iron distortion is commonly caused by materials that influence or distort a magnetic field but that do not necessarily generate a magnetic field, such as nickel and iron. Only the magnitude

and direction of the applied magnetic field with respect to the soft iron material affects the resulting magnetic field. Therefore, it is not additive distortion and can be considered as deflections in the existing EMF. The effect of the soft iron materials depends on the direction in which the field acts related to the magnetometer. Thereby, the compensation of the soft iron is more complicated than for the hard iron distortion and not as straightforward. As made evident by Figure 4.3, the typical effect of a soft iron distortion is exhibited as a deformation of the circle into ellipse at (0, 0).
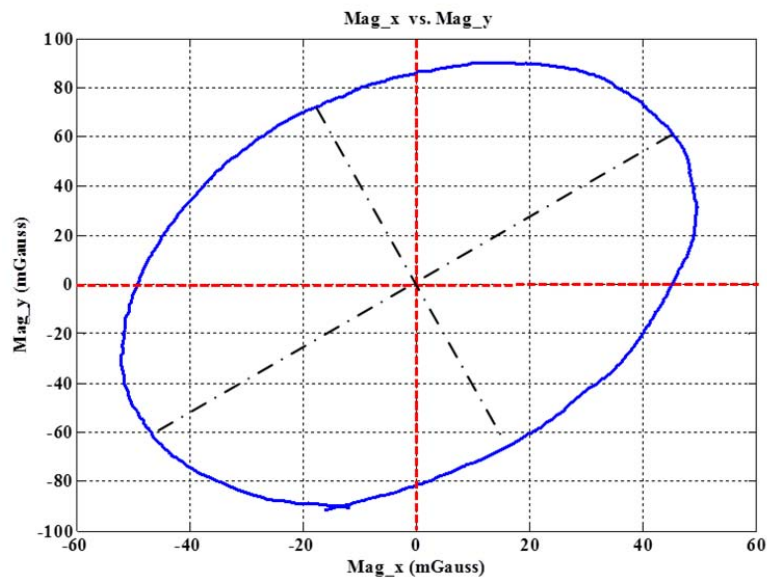
Figure 4.3: Magnetometer data with soft-iron distortion.

4.1.4 Case with Hard and Soft Iron Distortions

Figure 4.4 shows a combined hard and soft iron distortion where the circle has been distorted into an ellipse. The center of the ellipse is shifted from (0, 0) into (17, 68) in the presence of the hard iron distortions.
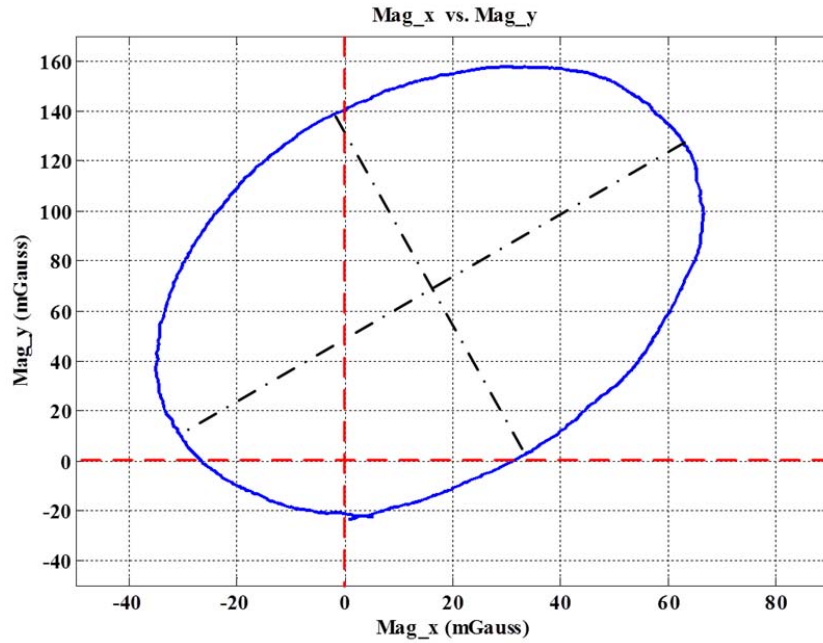
Figure 4.4: The effect of soft and hard iron effects.

4.2 Pre-Calibration process (Manoeuvring Modes)

Once the user is asked to do magnetometer calibration, he/she can move the device in different ways. In this section, suggested different manoeuvring modes are presented and analyzed.

4.2.1 Different Manoeuvring Modes (DMMs)

Since the EMF is weak and can be easily masked and unpredictably distorted by any sort of natural or man-made magnetic disturbance, a good manoeuvring technique during the calibration process can help improve the accuracy of calibration which will improved estimated heading. Different Manoeuvring Modes (DMMs) are investigated to achieve best estimation for the calibration parameters in the 3D Space. The purpose of the manoeuvring is to move the device in

91

the space and give the magnetometers the opportunity to cover a wide range of the change in the magnetic field.

Manoeuvring Mode (MM) is important for the calibration of magnetometer, which depends on the application at hand. It is proven by the experiments, shown later, even in cluttered indoor environments, a good Manoeuvring of the navigation device can lead to an improved heading estimation quality. This is mainly due to weak Signal to Noise Ratio (SNR), in dense indoor scenarios. The most common way to calibrate magnetometers in smartphones is by moving the device for a few seconds in the space to create 3D figure eights. By investigating the effect of this kind of motion other kinds of movement were found to be worth analyzing as well. This section focuses on the investigation of DMMs for the calibration process with the handheld devices such as portable navigations, smartphones, and tablets. Two more MMs, random and coordinated manoeuvring modes, are proposed for the purpose of the comparison. In the random MM, the device is moved randomly in space, while for the coordinated mode the device is rotated around the three axes in space.

The device can be maneuvered in different ways within the space, but some device movement could be restricted to certain space dimensions due to the applied dynamics. The device can be moved in 2D or 3D space. In 2D space, the coordinates refer to the movement in a plane with only 2 axes whilst 3D space represents the movement in the entire space with full axes definition. 2D calibration is suitable for constrained situations such as wheel-chair motion, vehicle dash-board fixed device, marine navigation (ships) etc. For these applications, the movement in circles is more intuitive. However, 3D calibration is apparent for pedestrian

navigation due to higher degrees of freedom in three dimensions. While moving the sensor in space, the shape, as described by its measurements, should be a sphere with a radius equal to the magnitude of the local Earth's magnetic field (Gebre-Egziabher et al. 2006). Thus, it is recommended to calibrate the device before starting the navigation mission for enhanced positioning accuracy. Three main MMs are selected to be compared, listed below.

4.2.1.1 Random Movement

The device is moved randomly in space as shown in Figure 4.5. The idea is to acquire significant changes in the signal levels for each axis of the magnetometer to allow the algorithm an opportunity to work efficiently. However, random movements may not always guarantee that. The absence of movements along a particular axis defies the purpose of 3D calibration logic and may not lead to optimal calibration.
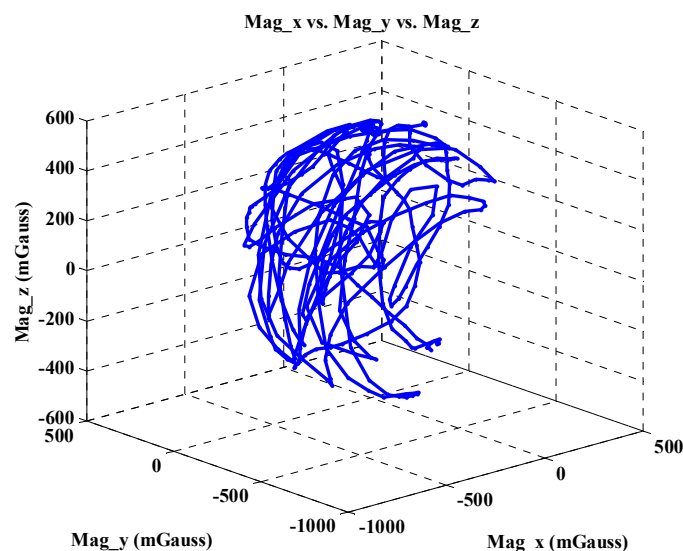
Figure 4.5: Random movement in the space.

4.2.1.2 Figure of Eights Movement

The device is moved to form a 3D-Figures Eight (3D-Eights) shape in the space. For the movement most smartphone devices, a 3D-Eights patter is recommended, shown in Figure 4.6. Accordingly, this technique was adopted to test other manoeuvrings to allow for results comparisons with other industry benchmarks.

(a) diagram   (b) Raw magnetometer data
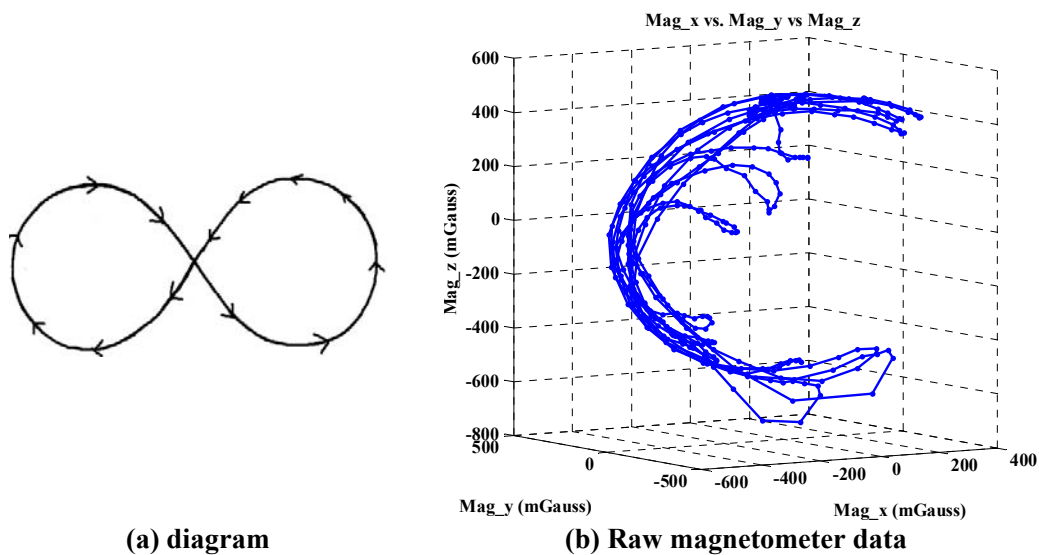
Figure 4.6: 3D- Figure Eights movement

4.2.1.3 Coordinated Movement

The device is moved in the space around the 3 axes X, Y, and Z, independent of the rotation sequence and direction. A synchronized movements about each axis as shown in Figure 4.7, is another way to calibrate the device which guarantee to cover the 3D space for calibration.

94

(a) diagram	**(b) Raw magnetometer data**
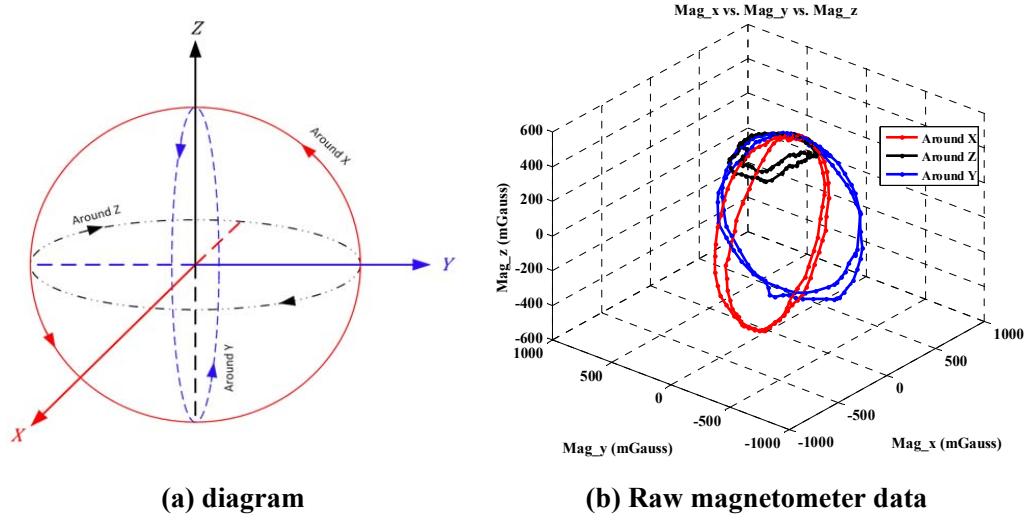
Figure 4.7: Coordinated movement

4.2.2 DMMs Performance and Analysis

In this section the testing of the calibration technique's performance is presented. This process was performed with each MM separately. The benchmark for testing the DMMs was the proximity of a calibrated magnetic field with a reference value for the EMF that did not contain any large perturbations. DMMs such as Random, 3D-Eights, and Coordinated are tested in different environments such as indoors and outdoors. Also, different users were involved in the experiment to validate the algorithm.

4.2.2.1 Accuracy of the calibrated magnetic field

It was important that the EMF value after the calibration process compensated for bias and scale factor effects in order to be close to the reference value of the local EMF. Therefore, the accuracy of the calibration process is reflected by the raw and calibrated total magnetic field

plots shown in Figure 4.8 (a - c) for indoor environment and Figure 4.9 (a - c) for outdoor environment. The estimated (after calibration) and raw values of earth's magnetic field are plotted on both figures. The calibrated readings show the constancy of the magnetic field, which is closer to of the EMF's reference value. These results indicate that the MMs play an important role in calibration; where the best results are obtained from coordinated modes.

(a) Random MM

(b) 3D Eights MM

Total Magnetic Field
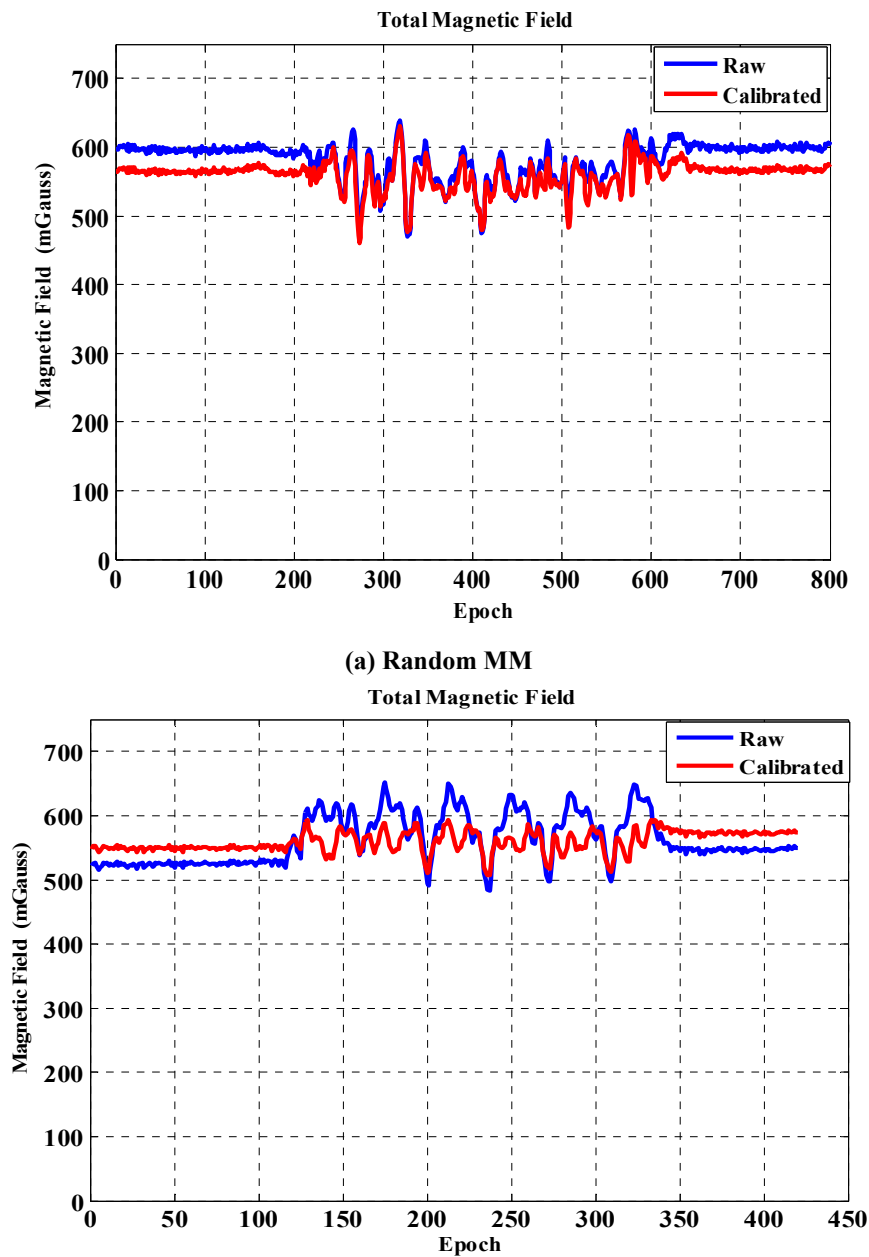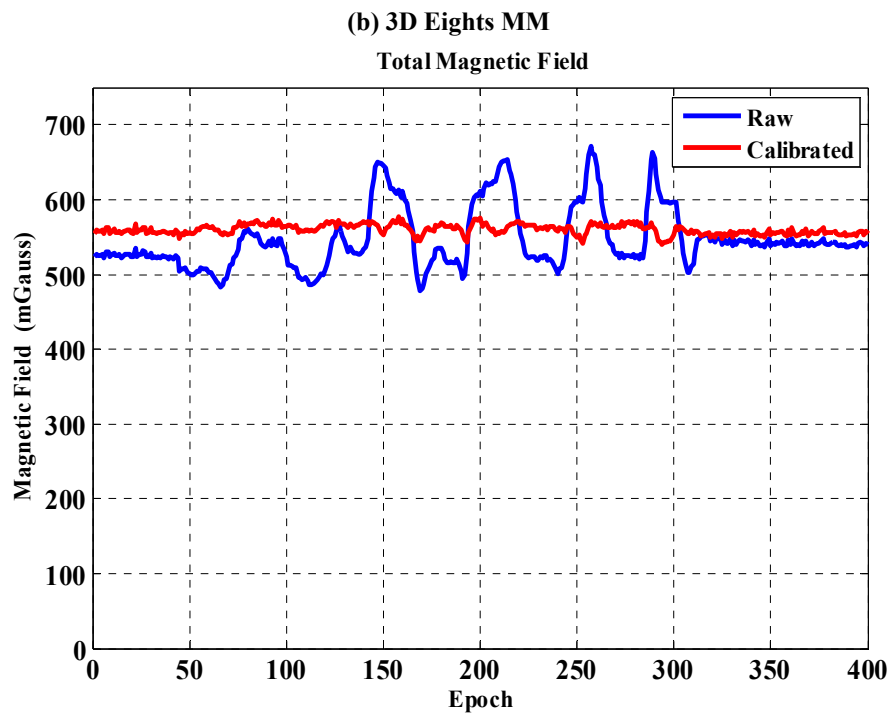
(c) Coordinated MM
Figure 4.8: Total raw and calibrated magnetic field indoors.

Total Magnetic Field

(a) Random MM

97
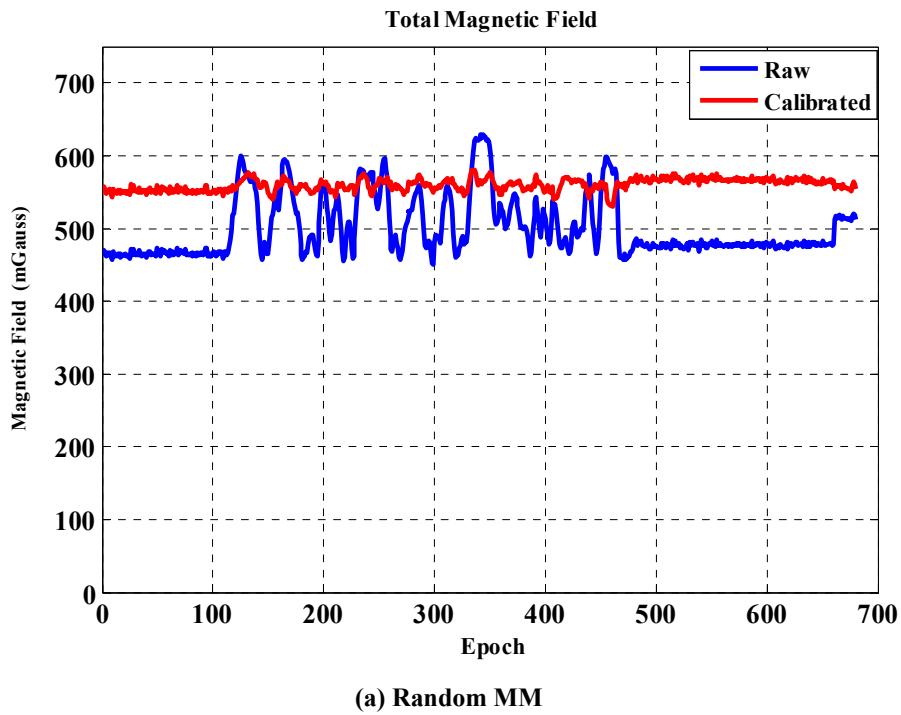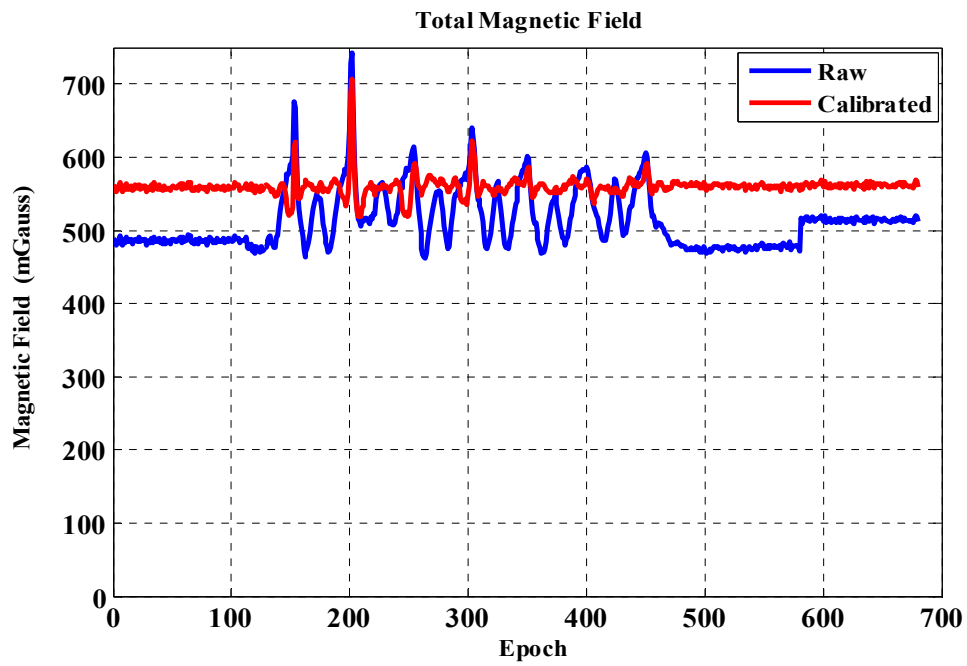
(b) 3D Eights MM
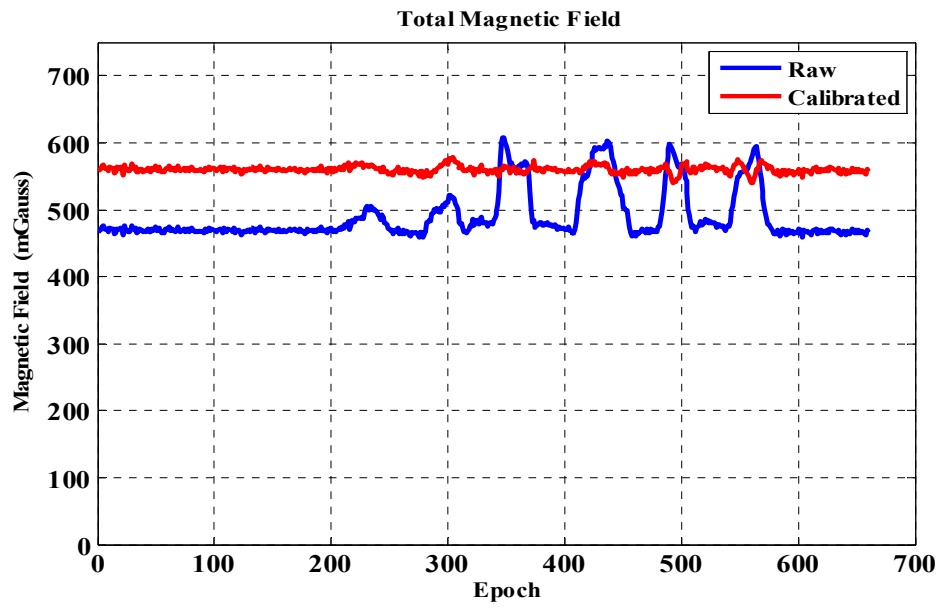
(c) Coordinated MM

Figure 4.9: Total raw and calibrated magnetic field outdoors.

98

Figure 4.10 (a - c) shows the calibration results using the PSO algorithm for the magnetometer measurements where both raw and calibrated measurements are plotted in a 3D mesh globe. As shown in Figure 4.10, the calibrated magnetic field differs from the raw in the un-calibrated case for all MMs which indicate the effects of the calibration process. The calibrated data is expected to fit the surface of the sphere with a radius of 570 mG. A comparison of the performance of the three manoeuvring modes shows that the coordinated mode is the most accurate where the calibration successfully coincides the field components with the mesh globe.

Raw   **Calibrated**

(a) Random manoeuvring mode

Raw   **Calibrated**

(b) 3D Eights manoeuvring mode

99
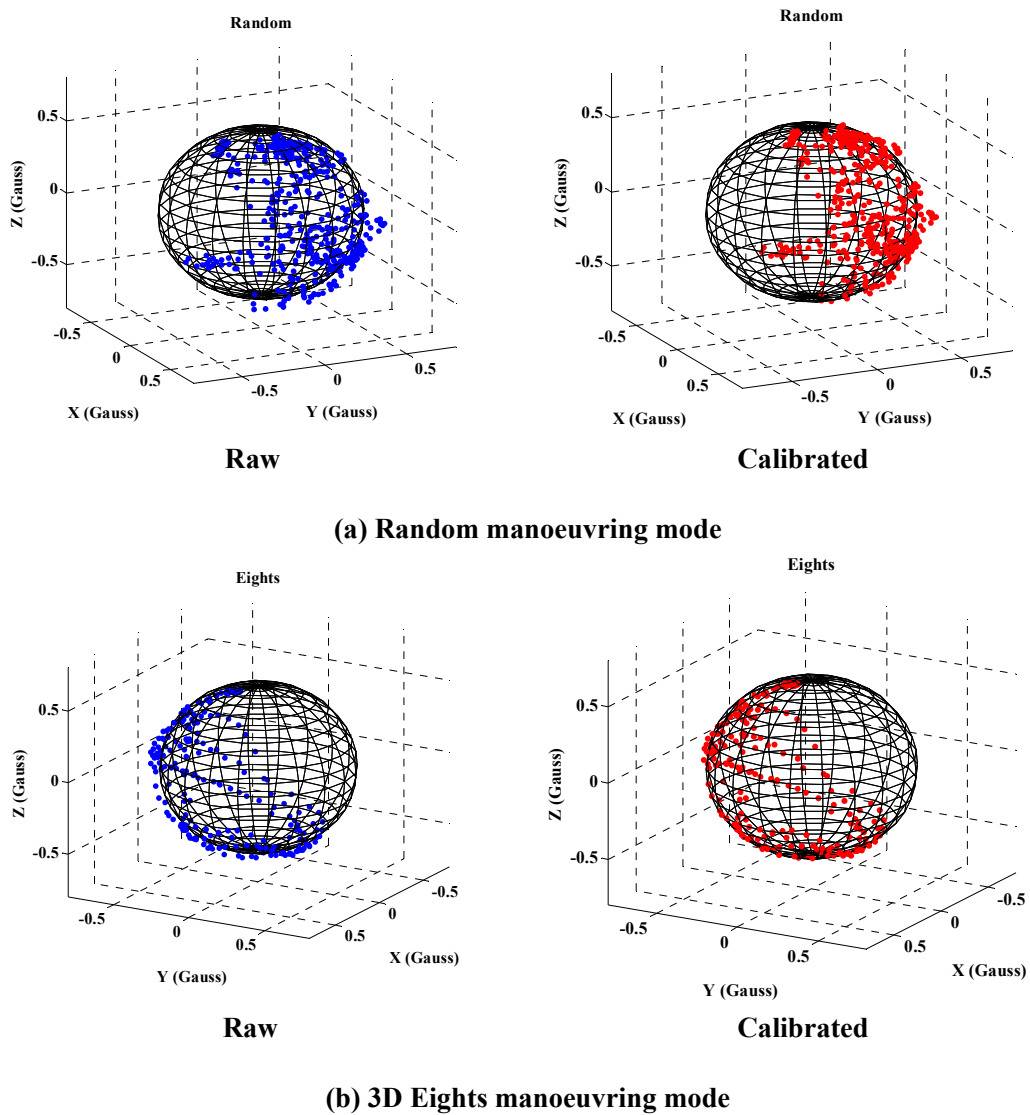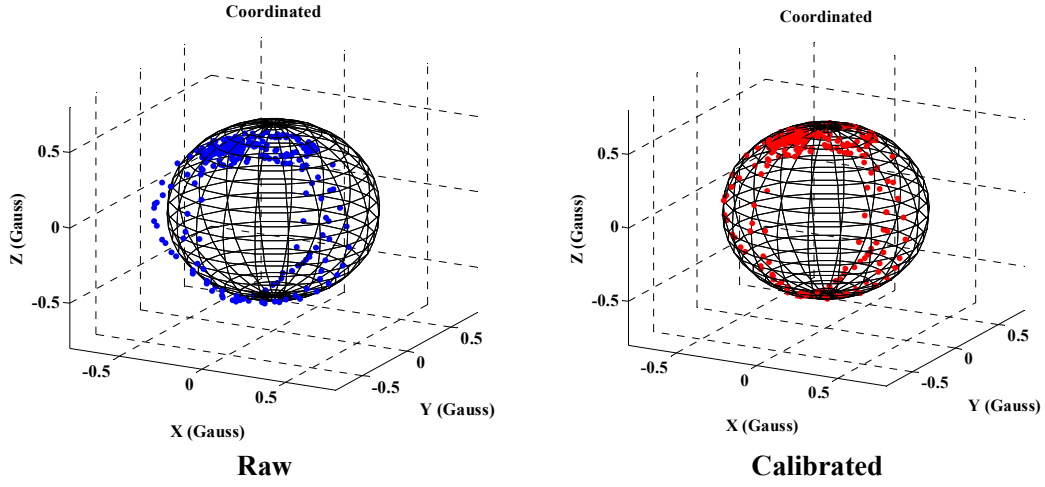
(c) Coordinated manoeuvring mode

Figure 4.10: Magnetometer calibration using DMMs.

4.2.2.2 Residual error analysis

The accuracy of the performance for the DMMs is compared in Figures (4.11 – 4.14) where the calibration error are calculated to assess the performance of the DMMs-based sensor calibration. Through these figures, the prefix "in_" is used to refer to indoor environment and "out_" is used to refer to outdoor environment. The MM calibration error for each user, *User_MM_error*, is calculated as the difference between the reference EMF value, H_m, and the calibrated magnetic field values, *H*, as given in Equation (4-1).

$$User\_MM\_error = H_m - H \qquad (4-1)$$

For all users, the mean and standard deviation of the error for each MM are calculated for the purpose of comparison as in Equation (4-2) and Equation (4-3).

$$User\_error\_mean = \frac{1}{n}\sum\left(User\_MM\_error\right) \qquad (4\text{-}2)$$

$$User\_error\_std = \sqrt{\frac{1}{n-1}\sum_{i=0}^{n}\left(User\_MM\_error_i - User\_error\_mean\right)^2} \qquad (4\text{-}3)$$

Where n is the total number of the measured samples.
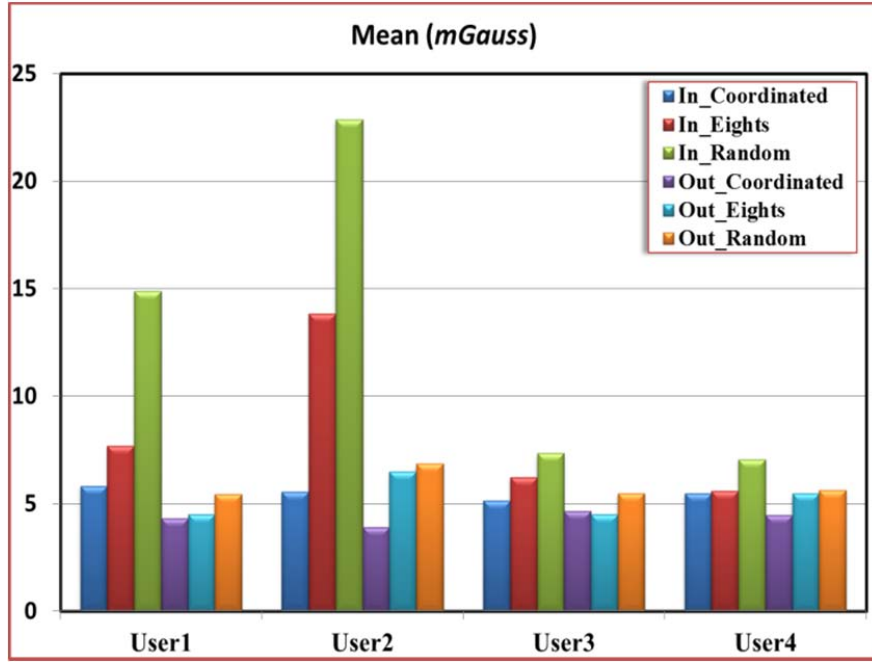
Figure 4.11: DMMs error means for all users.
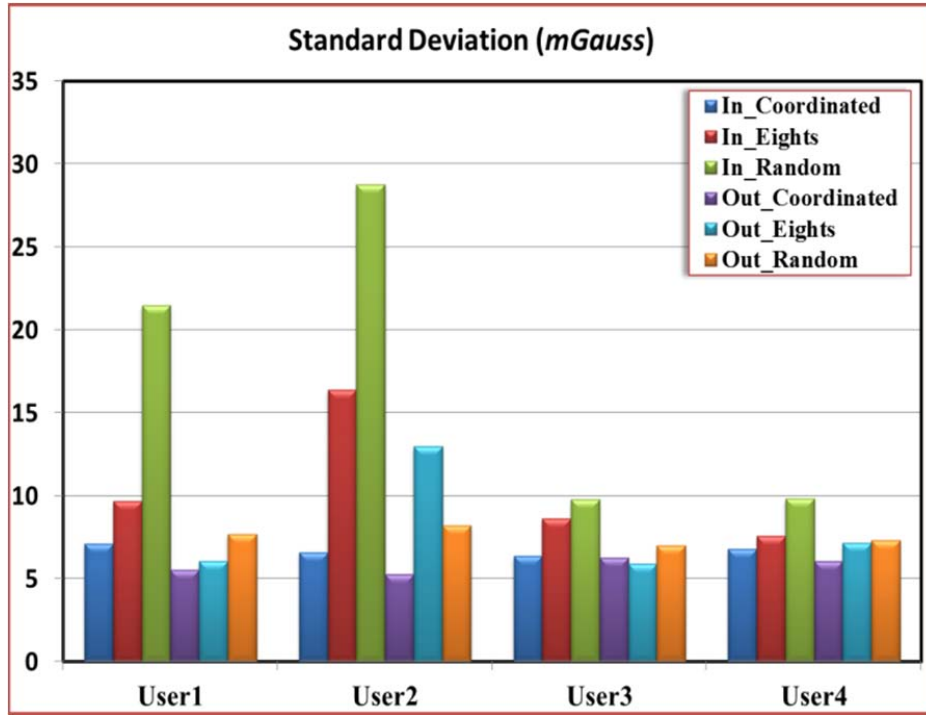
Figure 4.12: DMMs error standard deviations for all users.

For all users, the coordinated MM in both indoor and outdoor environments produces the lowest error on average. Compared to other MMs for all users in Figure 4.11, the recommended MM gives the minimum average error. Furthermore, Figure 4.12 indicates that for the same user, the coordinated MM is more accurate than other MMs, as observed from the standard deviation values.

To evaluate the overall performance of each MM, the errors for all users of the same MM are concatenated in one vector as given in Equation (4-4) where the mean and standard deviation are calculated, as in Equation (4-5) and Equation (4-6).

$$MM\_error = \begin{bmatrix} MM\_error\_user_1 & MM\_error\_user_2 & \dots & MM\_error\_user_m \end{bmatrix}^T \qquad (4\text{-}4)$$

$$4.2.2.2.1.1.1.1 \quad MM\_error\_mean = \frac{1}{N}\sum \left(MM\_error\right) \tag{4-5}$$

$$MM\_error\_std = \sqrt{\frac{1}{N-1}\sum_{i=0}^{N}\left(MM\_error_i - MM\_error\_mean\right)^2} \tag{4-6}$$

Where N is the number of all error samples as listed in Table 4.1 and m is the number of users - in this case four. Table 4.1 shows the total number of samples that were used in the evaluation process for each MM in the indoor and outdoor cases. The number includes samples of the four users for each MM.

Table 4.1: Total number of samples for each MM.

Manoeuvring Mode	N (samples)
Indoor Coordinated	1960
Indoor Eights	1780
Indoor Random	2440
Outdoor Coordinated	2480
Outdoor Eights	2720
Outdoor Random	2840

Figure 4.13 and Figure 4.14 illustrate that the coordinated MM yields the lowest error on average and has a smaller standard deviation among all other MMs in both indoor and outdoor environments.
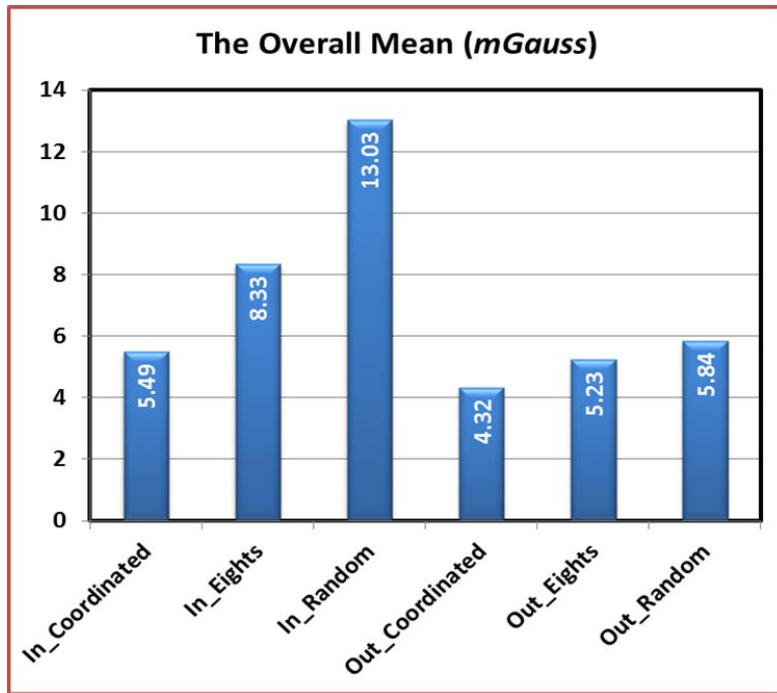
Figure 4.13: The average of the error mean of all users for DMMs.
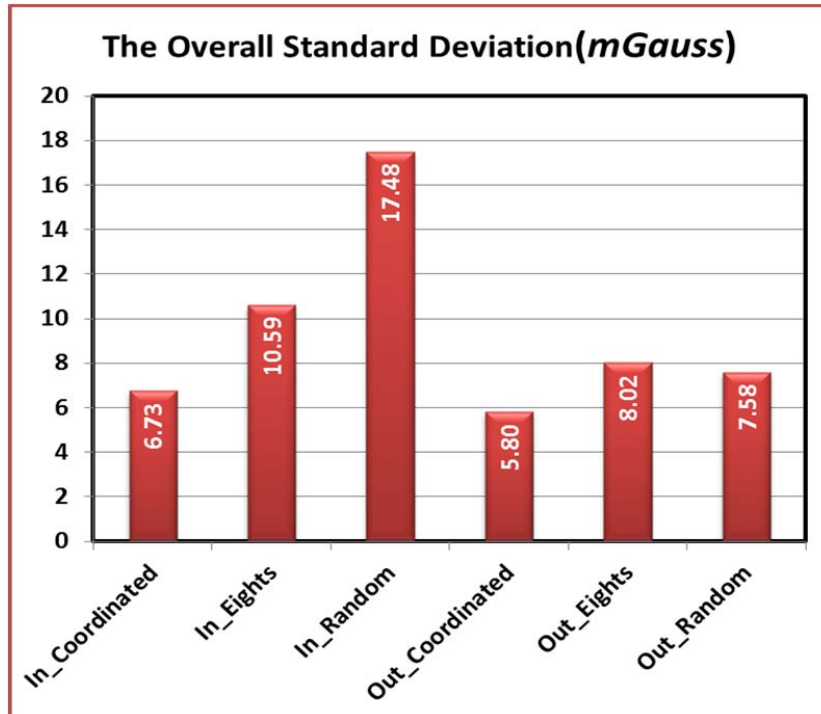
Figure 4.14: The average of the error standard deviation of all users for DMMs.

104

4.2.2.3 Error Distribution

The different histograms for the DMMs are plotted for the total error of both indoor and outdoor scenarios. The histogram provides important information about the shape of a distribution. According to these values, the histogram is either highly or moderately skewed to the left or right. The error levels percentages are shown in

Table 4.2:

a) Random.　　　　　**b) 3D-Eights.**　　　　　**c) Coordinated.**
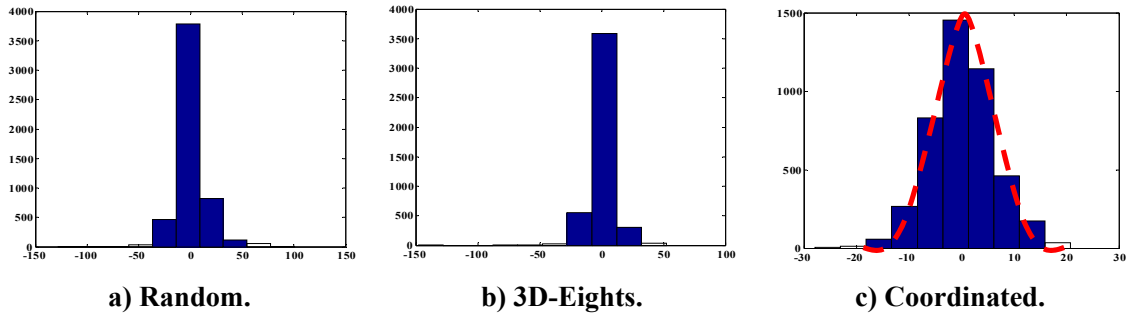
Figure 4.15: Histogram for the total errors (indoor and outdoor) of the DMMs.

Any natural process with unbiased errors tends to approximate a Gaussian behaviour (bell-shaped curve) (Chen 1996). The histograms in Figure 4.15 (a - c) present the error values of the DMMs and demonstrate the nature of the error values. A typical assumption is that the errors are normally distributed, *i.e.*, the deviations between the actually measured data if plotted as a histogram form a Gaussian (bell shaped) curve. This behaviour was observed in the MM described as coordinated. Indeed, the error vector behaves as a Gaussian noise with small standard deviation, and hence the manoeuvring can be described as optimal for magnetometer calibration.

Table 4.2: The percentages of error ranges.

Mode	≤ 10 *mGauss*	>10 *mGauss* & ≤ 20 *mGauss*	>20 *mGauss*
Random	68.13 %	19.00 %	12.87 %
3D-Eights	79.88 %	16.43 %	03.69 %
Coordinated	88.55 %	11.13 %	00.32 %

The percentage of the error values which lies around zero is also another important criterion to be discussed. As shown in

Table 4.2, the error range is divided into three main ranges; <= 10 *mGauss*, >10 & <= 20 *mGauss*, and > 20 *mGauss*. The results show that 88.55% of the error values are in the range of - 10 and 10 *mGauss* whereas it was 79.89% and 68.13 for 3D-Eights and random modes respectively. In the meanwhile, the portion of the error greater than 20 *mGauss* in coordinated mode is 0.32% while it was 3.69%, 12.87% for 3D-Eights and coordinated modes respectively.

4.2.2.4 Impact on magnetometer based heading estimation

In this section, the effects of different manoeuvring modes on the navigation solution are presented where the solution is estimated using the PDR algorithm. The magnetometer is calibrated based on DMMs mentioned earlier. At the beginning of the test, the DMMs were applied and a walking interval began while the device was held in the texting/reading mode. The

track was a tennis court in a rectangular shape that began at point **0**, reflected in Figure 4.16. The duration of the walk was 4 minutes around the 4 sides of the rectangle (1, 2, 3, and 4). The results were plotted to evaluate the efficiency of the estimated heading values. As shown in Figure 4.16, the coordinated manoeuvring mode resulted track was the closet to the GPS solution. All DMMs yielded acceptable results along sides 1 and 2. However, at side 3 the PDR solutions based on random and 3D Figure Eights began to drift while the coordinated solutions followed those from the GPS. As observed, the solution of Random and 3D Eights continuously drifted as time passed. In the meantime, the coordinated solution was closest to the GPS solution. As seen in the figure, the maximum drift of the coordinated manoeuvring mode after the 4 minute walking test was around 3-4 meters and 8 meters for the other modes. The drift in the different solutions was due to the surrounding elements and objects in the environment.

Figure 4.16: Heading results based on DMMs.

4.3 Magnetic Field Perturbation Detection Technique

Unpredictable perturbation of the magnetic field is a major drawback of geomagnetic sensors. Pedestrians spend most of their time in harsh environments such as urban areas, parking lots and offices. Unlike outdoor environments, harsh indoor environments are infrastructures containing primarily metals, electrical and electronic devices. Such objects generate or influence by the magnetic field which may change the EMF magnitude and direction. These kinds of disturbances make the magnetometer perform unsatisfactorily, which leads to inappropriate positioning for pedestrians.

4.3.1 Perturbation Detection

Due to the fluctuations in the magnetic field, it is necessary to smooth the measurements using a low pass filter to have the signal around the reference value of the magnetic field. To recognize any perturbations in the measurement, a threshold is defined as a normal margin for the signal variation. A threshold value of 3μT (30 *mGauss*) has been roughly defined as the root mean square value of the magnetic field during three steps (Ladetto et al. 2002). Thus, any signal bigger than this value will be considered a perturbation where the last estimated heading value will be held until the field becomes normal again. The effect of the disturbances decreases as the user is moving away from the source of the distortion. However, the effects are visible only for a few meters.

The proposed technique for magnetometer measurements perturbation detections is based on comparing the values of the different parameters with the expected values over fixed time interval. In this technique, the values are checked over a window size of 3 steps or 2 seconds of data. If there is a perturbation over 3 consecutive steps, the perturbation algorithm set a flag to indicate inaccurate magnetic measurement. The error values for the different parameters of the magnetic field can be calculated as in Equation (4-7):

$$S_{Err\_i} = S_{meas\_i} - S_{ref\_i} \tag{4-7}$$

Where:

- $i = 1{:}N$ is i^{th} element of the error vector in the data window
- S_{Err_i} is the error value for each parameter
- S_{meas_i} is the measured value for each parameter
- S_{ref_i} is the expected value for each parameter

The different thresholds for the test parameters are defined in Table 4.3.

Table 4.3: The threshold values for the parameters.

Parameter	Threshold (S_{thr})	Unit
F	30	*mGauss*
H	10	*mGauss*
V	30	*mGauss*
I	5	*Deg.*

The calculated errors of the magnetic field parameters as in Equation (4-7) are compared to the predefined thresholds to detect the perturbation in the magnetic field as given in Equation (4-8) based on the values shown in Table 4.3.

109

$$S_{Err\_i} < S_{thr} \tag{4-8}$$

The effect of the perturbation vector on the different magnetic field components should be taken into consideration for any magnetometer anomaly detector. When a pedestrian is walking in areas of dense infrastructure or even indoors it causes changes in the measured magnetic field. Such changes affect the different parameters and consequently lead to inaccurate heading estimation (Faulkner et al. 2010). The perturbation problem becomes difficult and more complicated if the external disturbance source affects different magnetic field parameters in different ratios. In contrast, the perturbation effect will be ignored if the external source affects the different components equally. The only change in this case is that the measured values of the parameters will be different from the expected, reference, values. Thus, the detector should compare the change in components individually and assess their different ratios. The magnetometer-based heading estimate is considered free of perturbation if the differences between the reference and the measured values are within the predefined thresholds.

Extensive tests have been conducted at the University of Calgary Campus. One test is done indoors using the Samsung Galaxy SII smartphone at the Olympic Oval, which consists of steel walls and concrete floors. The ability of the anomaly detection technique to detect the perturbation areas and the distorted magnetic field measurements is shown in Figure 4.17 and Figure 4.18. The figures describe two different parts of the trajectory with perturbed and non-perturbed areas. Figure 4.17 shows the interval of 60^{t} - 90th second while Figure 4.18 shows the interval of 530th – 560th second. As shown in Figure 4.17 (a), magnetic field strength variation was much larger than the expected value and creates an inaccurate heading estimation

(Figure 4.17 (b)). Only a few samples of the measurements successfully met the conditions of correct heading estimation.
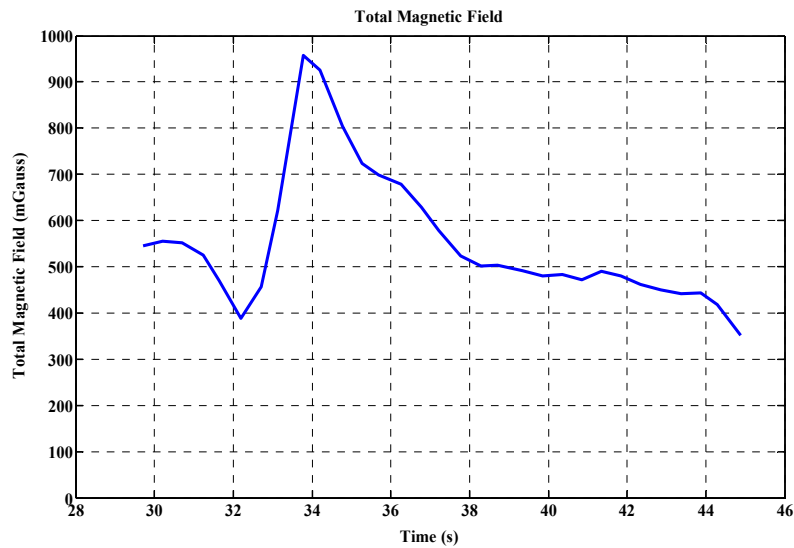
(a) Total magnetic field in perturbed area.
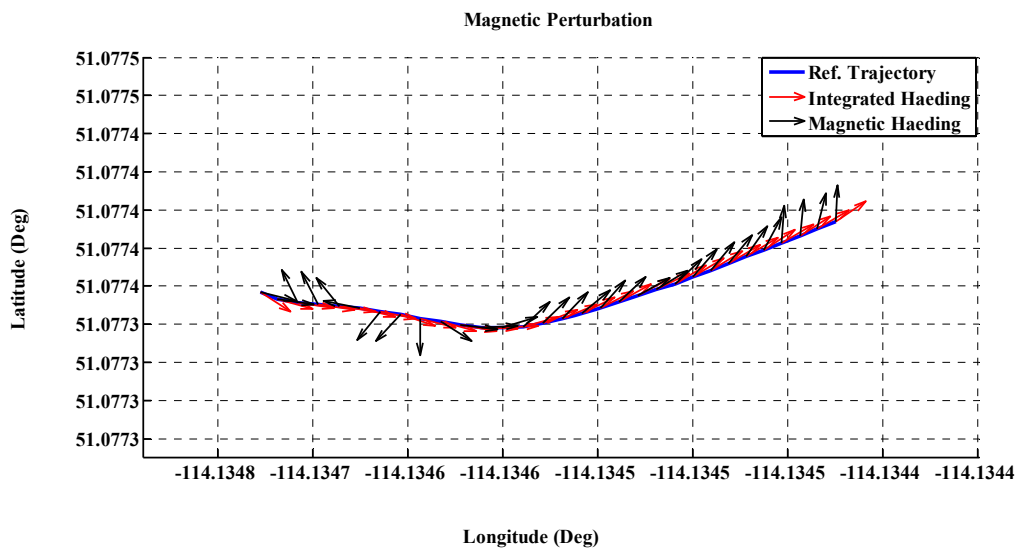
(b) Expected heading vectors in perturbed area.

Figure 4.17: Magnetometer behavior in a perturbed area.

In contrast, Figure 4.18 shows that the magnetic field does not have an abrupt change in the value, which indicates a normal area without perturbation.
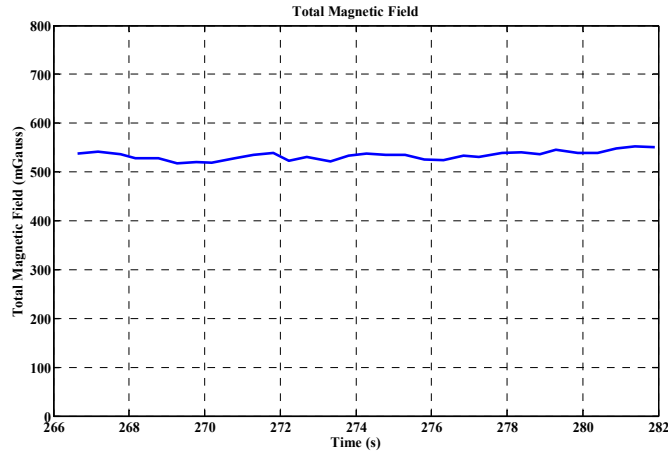
(a) Total magnetic field in non-perturbed area.
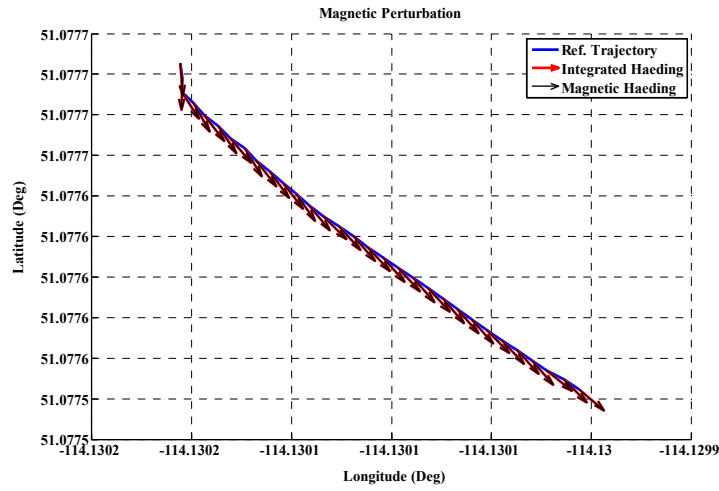
(b) Expected heading vectors in non-perturbed area.

Figure 4.18: Magnetometer behavior in a non-perturbed area.

The quality of the magnetometer based heading estimate can be observed and assessed based on the proposed anomaly detection. The technique estimates the different associated errors with the magnetic parameters. As a result, this can lead to significantly reduced heading errors and improved position accuracy by rejecting distorted magnetic measurements efficiently in real-time.

Chapter Five: Integrated Gyroscope/Magnetometer Heading Estimation

The PDR navigation is mainly based on estimating the traveled distance and the attitude of the user. As described in Chapter 2, the total traveled distance is estimated by detecting and counting the user steps and step length using accelerometer data, while the heading information can be determined using GPS, gyroscope, or magnetometer information. In certain areas, satellite signals are partially or completely blocked limiting the use of the GPS. In contrast, the heading information from a magnetometer and gyroscope is continuously available. Integrating the solutions from both gyroscopes and magnetometers can play an important role in pedestrian navigation through various environments. In this chapter, a de-centralized LKF-based technique with an open loop error feedback scheme is proposed to estimate the device's attitude using the quaternion mechanization from the gyroscopes' data.

5.1 Introduction

Nowadays, most smartphones are programmable and equipped with self-contained, low cost, small size, and power-efficient sensors, such as gyroscopes and accelerometers in addition to magnetometer. Therefore, an integrated inertial navigation solution with a magnetometer-derived heading can significantly improve the heading estimates for pedestrian navigation applications in different environments. In current state of the art of MEMS technology, the accuracy of gyroscopes is not good enough for deriving the attitude information over longer durations of time. However, for short periods this accuracy is quite acceptable. Magnetometers in contrast, provide absolute heading information once it they have been correctly calibrated. However, the

EMF can easily be disturbed by nearby ferrous objects, which makes the data unreliable for brief intervals. This highlights a need for further investigation into possible integration scheme for complementary sensors such as gyroscope and magnetometer.

There have been several studies in recent years that investigate the use of magnetometers for personal positioning applications. Some approaches use magnetometers exclusively for heading estimation (Cho et al. 2003) while others integrate them with an IMU (Aparicio 2004; Yun & Bachmann 2006). One commercially available personal locator system based on this principle is the Dead Reckoning Module DRM-4000 made by Honeywell (Honeywell 2009). A quaternion based method to integrate IMU with magnetometer is presented by (Marins et al. 2001). Three body angular rates and four quaternion elements were used to express orientation and were selected as the states of KF. In (Han & Wang 2011), a linear system error model based on the Euler angles errors expressing the local frame errors was developed and the corresponding system observation model derived. The proposed method does not need to model the system angular motion. It also avoids the issue of nonlinearity, which is inherent in the more frequently used methods. A similar technique is proposed by (Emura & Tachi 1994) where the angular rates were modeled for constant. A nonlinear derivative equation for the Euler angle integration kinematics is investigated in (Cooke et al. 1992). (Foxlin 1996; Setoodeh et al. 2004) presented a Euler angle error based method to integrate IMU with magnetometer data where three Euler angle errors and three gyroscope biases were used as states for KF. The estimated states were used to correct the Euler angles and to compensate gyroscope drifts, respectively.

114

As will be described through this chapter, the integration between the gyroscope and magnetometer based attitude was performed using the LKF technique. The quaternion mechanization using the gyroscopes' measurements was used to estimate the attitude information along with the gyroscope bias. The accelerometer data was used to update for roll and pitch information while the magnetometer data provided the heading update.

5.2 Sensors Heading Information

Heading estimation is probably the most challenging aspect of PDR, which largely determines the ultimate accuracy and quality of the navigation solution. Combining gyroscopes with magnetometers helps to achieve a desired level of accuracy in the heading solution, due to their complementary characteristics

5.2.1 Gyroscope Attitude Estimation

Gyroscopes are mainly used to determine the system orientation in many applications. The output of this sensor is a rotational rate. Performing a single integration on the gyroscopes outputs is necessary to obtain a relative change in angle. In the following subsections, the effect of the gyroscope bias on the estimated heading and the manner in which to estimate it using the appropriate sensor model will be described. Also, the quaternion-based heading estimation technique will be investigated.

5.2.1.1 Sensors Performance

All sensors are characterized by several errors types which it can be caused externally such as disturbance or internally such as noise (Boulic et al. 1990). The disturbance is more similar to a bias with respect to the noise. Such errors, noise and disturbance, are random in nature and can make the measurement sometimes unstable. The effects of the different errors can be reduced by conducting a rigorous investigation into their potential causes. This section will describe the effect of the drift on the gyroscope measurements and the appropriate way to reduce such effect. Also, AV analysis is a common procedure used for modeling the effects of sensor noise is presented (Xing & Gebre-Egziabher 2008)

5.2.1.1.1 Effect of Bias Drift on Gyroscope based Heading Estimation

All sensors are characterized by several errors types which it can be caused externally such as disturbance or internally such as noise (Boulic et al. 1990). The disturbance is more similar to a bias with respect to the noise. Such errors, noise and disturbance, are random in nature and can make the measurement sometimes unstable. The effects of the different errors can be mitigated by conducting an investigation into their causes. Bias can be considered the main source of error in inertial sensors, which has systematic behavior for all data epochs. There are two major types of bias; static bias and dynamic bias. Static bias is called the turn-on or repeatable bias because it is constant during the run; however it has a different value each time the device is turned on. The effect of such bias can be considered constant if the operation time is limited to a few hours (De Agostino et al. 2010). On the other hand, the dynamic bias, known as in-run bias, depends on the

116

sensitivity of the sensors to the variation in the temperature. The effect of such error can be significant in the case of using MEMS sensors. Therefore, the bias should be compensated to avoid any effect on the navigation solution.

Due to the integration process, which is highly sensitive to the systematic errors of the gyroscopes, the bias introduces a quadratic error in the velocity and a cubic error in the position (El-Sheimy 2012). Gyroscopes measurements can generally be described using Equation (5.1):

$$I_{\omega} = \omega + b_{\omega} + S_{\omega} + N_{\omega} + \varepsilon(\omega)$$
(5.1)

Where I_{ω} is the measured angular rate, ω is the true angular rate, b_{ω} is the gyroscope bias, S is the linear scale factor matrix, N is the non-orthogonality matrix and $\varepsilon(\omega)$ is the sensor noise. With integration, the gyroscope bias will introduce an angle error in pitch or roll proportional to time i.e. $\delta\Theta = \int b_{\omega}dt = b_{\omega}t$; this small angle will cause misalignment of the IMU. Therefore, when projecting the acceleration, from the gravity vector g, from the body frame to the local-level frame, the acceleration vector will be incorrectly projected due to this misalignment error. This will introduce an error in one of the horizontal acceleration i.e. $\delta a = g \sin(\delta\Theta) \approx g\delta\Theta \approx gb_{\omega}t$.

Consequently, this leads to an error in velocity $\delta v = \int b_{\omega}gtdt = \frac{1}{2}b_{\omega}gt^{2}$ and in position $\delta p = \int \delta v dt = \int \frac{1}{2}b_{\omega}gt^{2}dt = \frac{1}{6}b_{\omega}gt^{3}$. To overcome the problem of error drift, a bias compensation of gyroscopes is required.

The deterministic bias can be sensed using a static period of 30 seconds, where the deviation in the gyroscope output can be observed. The effect of gyroscope drift on the estimated heading is

shown in Figure 5.1. The figure shows the results of seven tests conducted in static mode where the device is held on a table for approximately six minutes. The gyroscope-based heading estimated value is provided for each test. The expected heading during a test should be 0, 10, …, and 60° for all tests respectively. However, due to the gyroscope bias drift, the estimated heading drifted continuously with time.
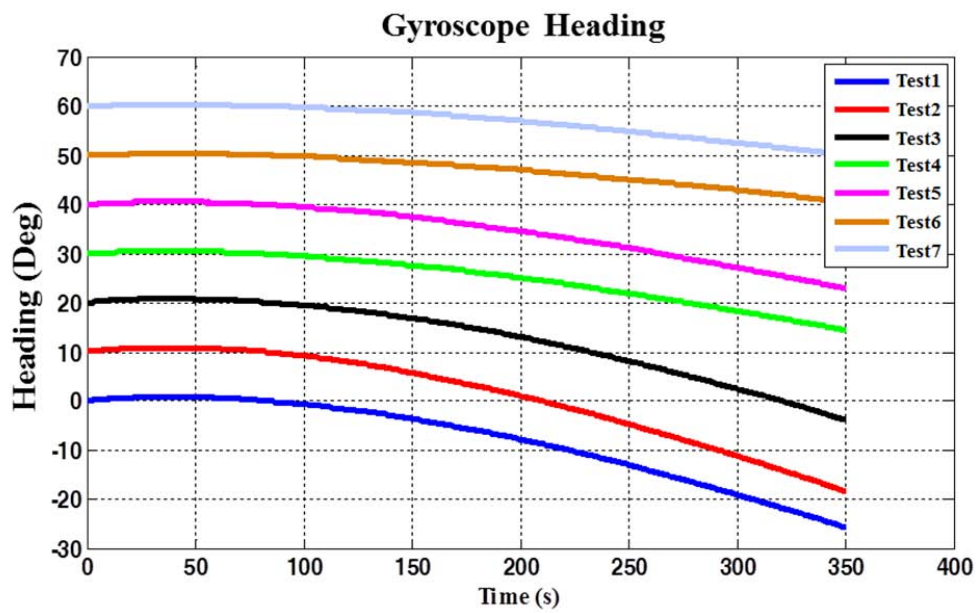
Figure 5.1: The effect of bias drift on the estimated gyroscope-based attitude.

5.2.1.1.2 Allan Variance (AV) Analysis

Irrespective of the type of sensor behaviour and structure, sensors calibration is necessary and required as part of the pre-processing stage. The calibration effectively enables the sensors to be able to combine their data effectively in real-time. After completion of the pre-processing stage, a further signal conditioning is required to remove the residual bias. Then, scale-factor errors analysis on the PND was done using AV analysis (El-Sheimy et al. 2008; Hou & El-Sheimy

118

2003; Shin 2005) and preliminary bias and scale factor estimation for the accelerometer and gyroscope.

Calibration for the deterministic errors associated with the different sensors involved in the navigation solution such as inertial and magnetic field sensors is not enough since their outputs should be compensated regarding the stochastic error. Different suggested approaches in the literature (El-Sheimy et al. 2008; Hou & El-Sheimy 2003; Savage 2000; Shin 2005) are available for calibrating accelerometer and gyroscope signals. Lab tests were also conducted to estimate the bias and scale factors of the gyroscope and accelerometer.

The performance of the sensors is characterized by two major sources of errors: noise and disturbance, where noise is an internal source and disturbance external (De Agostino et al. 2010). The disturbance is random, unpredictable and varies from epoch to epoch. The MEMS sensors that were used were low-cost, which makes the signal highly disturbed by noise and also subject to random and unpredictable, run-to-run, uncertainty. To estimate the error associated with the gyroscopes, AV analysis was used and realized. A static experiment was conducted for the different gyroscopes while taking into consideration a data logging time of about 22 hours. A series of data composed by N elements with a sampling rate of Δt_o, can be clustered to groups with n elements where $n<N/2$. The AV analysis can be described as:

$$\sigma^2(T)=(\frac{1}{2T^2(N-2n)})\sum_{i=1}^{N-2n}(S_{i+2n}-2S_{i+n}+S_i)^2 \qquad (5.2)$$

Equation (5.2), S is the gyroscope sensors data to be analyzed in Figure 5.2. During the test, a gyroscope Invensense MPU 3050 was used. A complete description of the sensor's characteristics will be discussed in Chapter 6.

Allan deviation of Invensense MPU3050 gyroscope
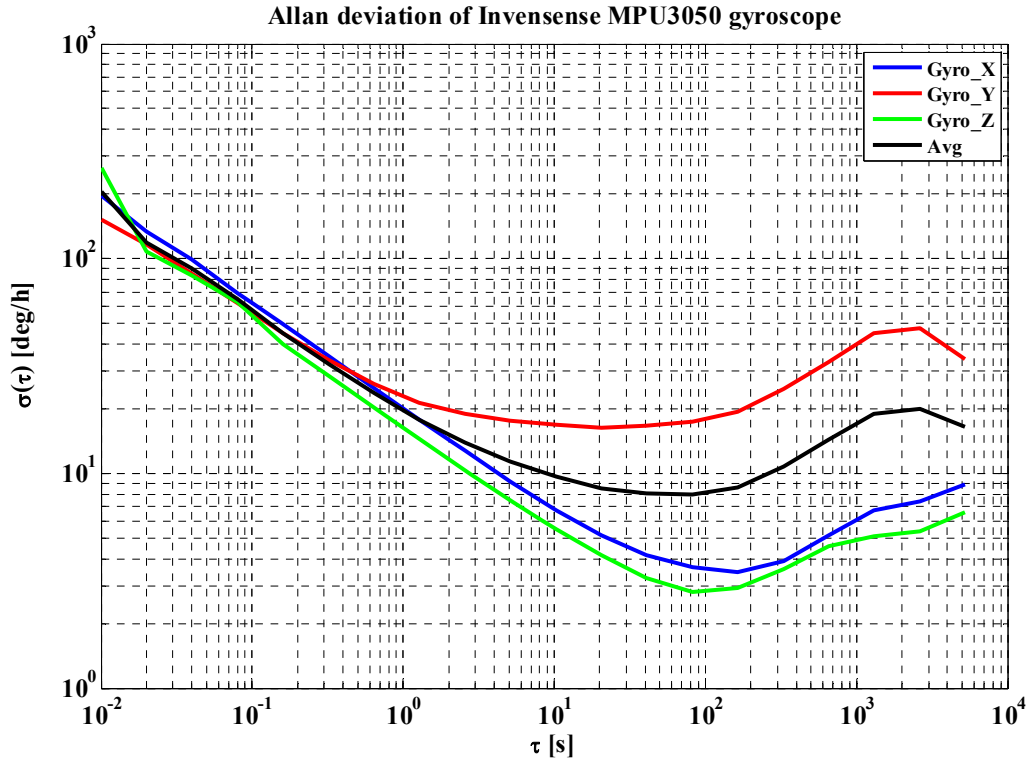
Figure 5.2: Allan Deviation for the *Invensense MPU3050* gyroscopes.

Table 5.1 shows the angle random walk and bias instability values of the gyroscopes axes. The values are estimated and derived from the Allan deviation plots.

Table 5.1: Gyroscopes Noise Measurements.

	Bias Instability	Angle Random Walk
Gyro_X	3.473 °/h (164 s)	20 °/√h
Gyro_Y	16.37 °/h (20 s)	22 °/√h
Gyro_Z	2.804 °/h (82 s)	16.27 °/√h
Avg	7.958 °/h (82 s)	19.75 °/√h

5.2.1.2 Quaternion Mechanization

In order to obtain the heading from the gyroscope, the initial attitude should be provided from an absolute reference or by the user. At the first epoch, the derived heading from the magnetometer is provided to the algorithm. In addition to that, the initial roll and pitch angles, calculated from the accelerometer signal during a static period, should be passed as well. The relationship between the C^n matrix and Euler angles is given in Equation (5.3) with the sequence ($R_\phi^x R_\theta^y R_\psi^z$) (Kuipers 1999).

$$C^n = \begin{bmatrix} cos\,\theta cos\,\psi & cos\,\theta sin\,\psi & -sin\,\theta \\ sin\,\phi sin\,\theta cos\,\psi - cos\,\phi sin\,\psi & sin\,\phi sin\,\theta sin\,\psi + cos\,\phi cos\,\psi & sin\,\phi cos\,\theta \\ cos\,\phi sin\,\theta cos\,\psi + sin\,\phi sin\,\psi & cos\,\phi sin\,\theta sin\,\psi - sin\,\phi cos\,\psi & cos\,\phi cos\,\theta \end{bmatrix} \quad (5.3)$$

A quaternion is a four dimensional vector which is defined based on a vector q and a rotation angle. The vector q is given as:

$$q = (q_1,\ q_2,\ q_3,\ q_4) \quad (5.4)$$

While the magnitude of the rotation angle can be written as;

$$\Theta = \sqrt{\Theta_x^2 + \Theta_y^2 + \Theta_z^2} \quad (5.5)$$

Where $\begin{bmatrix} \Theta_x & \Theta_y & \Theta_z \end{bmatrix}^T$ is the rotation angle of the moving device. The angular increments for the above rotation angle, at $\Delta T = 1/(gyroscope\ rate)$, are:

$$\begin{bmatrix} \delta\Theta_x \\ \delta\Theta_y \\ \delta\Theta_z \end{bmatrix} = \Delta T \begin{bmatrix} \Theta_x \\ \Theta_y \\ \Theta_z \end{bmatrix} \quad (5.6)$$

The magnitude of the above angular increment is:

$$\delta\Theta = \sqrt{\delta\Theta_x^2 + \delta\Theta_y^2 + \delta\Theta_z^2} \quad (5.7)$$

121

The angular increments obtained in Equation (5.7) is used to update the quaternion (Schwarz & Wei 2000):

$$
\begin{bmatrix} q_1 \\ q_2 \\ q_3 \\ q_4 \end{bmatrix}_{k+1} = \begin{bmatrix} q_1 \\ q_2 \\ q_3 \\ q_4 \end{bmatrix}_k + \frac{1}{2} \begin{bmatrix} c & s\delta\Theta_z & -s\delta\Theta_y & s\delta\Theta_x \\ -s\delta\Theta_z & s\ c & s\ \delta\Theta_x & \delta\Theta_y \\ s\delta\Theta_y & -s\delta\Theta_x & c & s\delta\Theta_z \\ -s\delta\Theta_x & -s\delta\Theta_y & -s\delta\Theta_z & c \end{bmatrix} \begin{bmatrix} q_1 \\ q_2 \\ q_3 \\ q_4 \end{bmatrix}_k
$$
(5.8)

And the coefficients c and s are computed as:

$$
c = 2\left(cos\left(\frac{\delta\Theta}{2}\right) - 1\right)
$$

$$
s = \frac{2}{\delta\Theta} sin\left(\frac{\delta\Theta}{2}\right)
$$
(5.9)

The norm of the quaternion q_{norm} q$_{norm}$ is defined as:

$$
(q_{norm})_{k+1} = \begin{bmatrix} q_{1_{nrom}} \\ q_{2_{nrom}} \\ q_{3_{nrom}} \\ q_{4_{nrom}} \end{bmatrix}_{k+1} = \frac{1}{q_{mag}} \begin{bmatrix} q_1 \\ q_2 \\ q_3 \\ q_4 \end{bmatrix}_{k+1}
$$
(5.10)

Where the quaternion magnitude q_{mag} q$_{mag}$ is defined as:

$$
q_{mag} = (\sqrt{q_1^2 + q_2^2 + q_3^2 + q_4^2})_{k+1}
$$
(5.11)

The updated DCM can be calculated based on the quaternions norm values as in Equation (5.12). Where, the DCM matrix, in terms of quaternion vector components, can be obtained by using the following formulation:

$$
C_b^l = C^n(q) = \begin{bmatrix} 2q_1^2 - 1 + q_2^2 & 2q_2q_3 + 2q_1q_4 & 2q_2q_4 - 2q_1q_3 \\ 2q_2q_3 - 2q_1q_4 & 2q_1^2 - 1 + q_3^2 & 2q_3q_4 + 2q_1q_2 \\ 2q_2q_4 + 2q_1q_3 & 2q_3q_4 - 2q_1q_2 & 2q_1^2 - 1 + q_4^2 \end{bmatrix}
$$
(5.12)

122

Where C_b^l or C^n represents the transformation matrix between the quaternion vector and the DCM. The matrix transforms from the body frame to the local level (navigation) frame. The roll, pitch, and azimuth values can be obtained by using the *atan2* math function on the values of the C^n propagated inside the sensors navigation equations;

$$\phi = tan^{-1}\left(\frac{C^n\left(2,3\right)}{C^n\left(3,3\right)}\right) \tag{5.13}$$

$$\theta = -sin^{-1}\left(C^n\left(1,3\right)\right) \tag{5.14}$$

Similarly, the gyroscope-based heading values, ψ_{gyro}h$_{gyro}$, can be evaluated as:

$$\psi_{gyro} = tan^{-1}\left(\frac{C^n\left(1,2\right)}{C^n\left(1,1\right)}\right) \tag{5.15}$$

5.2.2 Magnetometer Based Heading Estimation

As discussed in Chapter 3 and 4, the magnetometer provides absolute measurement of the mobile device heading, or any object to which it is attached. The magnetometer is leveled with respect to the local level frame using the roll and pitch information. The heading (ψ_{mag}), magnetic direction can be calculated using the horizontal components (*x* and *y* axes) of a magnetic sensor as follows;

$$\psi_{mag} = tan^{-1}\left(\frac{-H_y}{H_x}\right) + D \tag{5.16}$$

Where D is the declination angle (15° for Calgary), H_x and H_y are the horizontal components of the de-tilted observed magnetic field. In order to account for the roll (ϕ) and pitch (θ) between the sensor frame and the local level frame, the sensor observations should be rotated by the

123

respective angles (roll and pitch) using Equation (5.17) and Equation (5.18) in prior to applying Equation (5.16)

$$H_x = B_x \, cos \, \theta + B_y \, sin \, \phi \, sin \, \theta + B_z \, cos \, \phi \, sin \, \theta \qquad (5.17)$$

$$H_y = B_y \, cos \, \phi - B_z \, sin \, \phi \qquad (5.18)$$

For an estimate of the heading angle from the magnetometer, the roll and pitch angle may be used to transform the magnetometer's measurements (denoted as *H*) from the sensor frame to the horizontal level frame (local level/h-frame). The heading value is obtained in the h-frame, and is measured about z-axis clockwise from a north direction.

5.3 Multi-Sensors Heading Fusion Filter

There are two different strategies that can be applied to the heading information from both the magnetometer and gyroscope in the PDR algorithm (Ladetto et al. 2001). In the first strategy, the magnetometer can be considered the primary source of heading while the gyroscope is used in the case of a geomagnetic disturbance. In the second approach, a self-contained gyroscope provides the attitude and the magnetometer functions as an absolute source for heading update to avoid error drift problem. As a complementary system, the gyroscope can be used to provide useful information to detect magnetometer disturbances while the magnetometer itself can be used to evaluate the bias and the initial heading for the gyroscope. Table 5.2 shows the different advantages and disadvantages of the gyroscope and magnetometer (Ladetto et al. 2001).

Table 5.2: Comparison between magnetometer and gyroscope.

	Advantages	Disadvantages
Gyroscope	- Self-contained, no external disturbances - Short term accuracy	- Error drift with time - Relative attitude
Magnetometer	- Absolute heading - Long term accuracy - No bias or error drift	- Unpredictable error - Measurement distortion

A complementary sensor fusion technique was designed to estimate the device attitude by combining the signals of three gyroscopes, three accelerometers, and three magnetometers. Gyroscopes measure orientation by integrating angular velocities and an accelerometer (as an inclinometer) while magnetometers (as a compass) provide a noisy and disturbed but drift-free measurement of orientation. The proposed fusion technique weighs the different sources of heading information appropriately according to knowledge about their signal characteristics.

The orientation of the device is commonly estimated using the inertial sensor. As described in Chapter 2, there are three main approaches for attitude representation; DCM, Euler Angle, and Quaternion. Among the three techniques, quaternion algebra was the preferred method. The estimated orientation from the gyroscope was very noisy leading to unbounded growth in the heading errors. An integration scheme for the gyroscope, accelerometer, and magnetometer data is proposed to estimate the device orientation and the gyroscope bias. The proposed scheme is a quaternion based KF as shown in Figure 5.3.
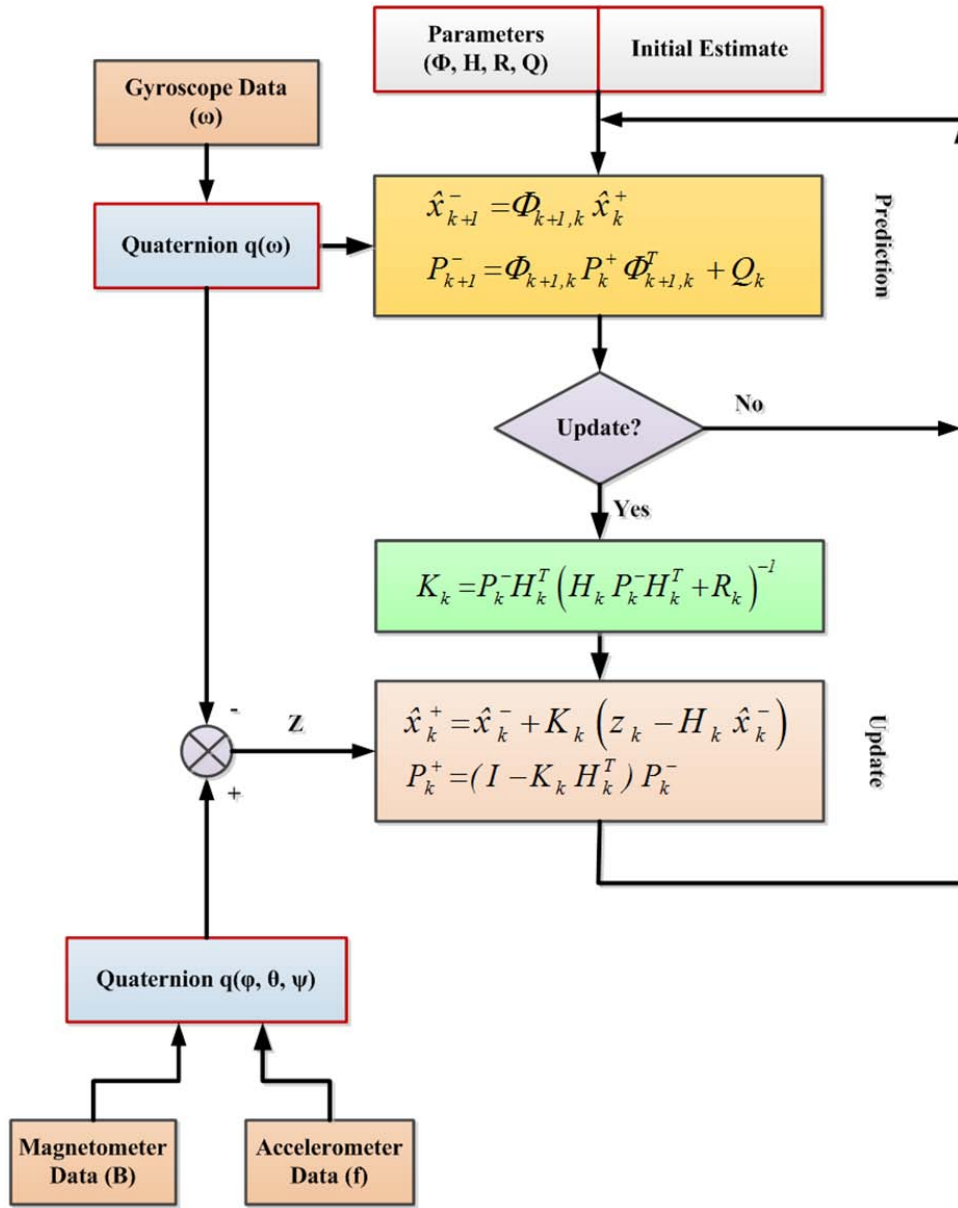
Figure 5.3: Flow of the Kalman filter process

In order to estimate the quaternion parameters and gyroscope biases estimation for a device carried by a pedestrian, the required models for the states and measurements in KF and their respective system and measurement error models are presented in this section.

5.3.1 The States Error Model

Essentially, the target of the proposed filter is to estimate the device attitude based on the quaternion technique. As discussed, the attitude information can be driven from the quaternion based DCM where roll, pitch, and azimuth can be estimated using Equations (5.13) to Equation (5.15) respectively.

The non-linear form of the system model in the absence of the known input can be written as

$$\dot{x}(t) = F(x(t), t) + G(t)W(t) \tag{5.19}$$

Where $F(x(t), t)$ is now a non-linear function describing the time evolution of the states. Consider a nominal trajectory, $x^{nom}(t)$, related to the actual trajectory, $x(t)$, as

$$\delta x(t) = x(t) - x^{nom}(t) \tag{5.20}$$

where $\delta x(t)$ is a perturbation from nominal trajectory. performing a Tylor Series expansion Equation (5.19) about the nominal trajectory yields

$$\dot{x}(t) \approx F(x^{nom}(t), t) + \left. \frac{\partial F(x(t), t)}{\partial x(t)} \right|_{x(t) = x^{nom}(t)} \delta x(t) + G(t)W(t)$$

$$= \dot{x}^{nom}(t) + F \, \delta x(t) + G(t)W(t) \tag{5.21}$$

$$\dot{x}(t) - \dot{x}^{nom}(t) = F \, \delta x(t) + G(t)W(t)$$

$$\delta \dot{x}(t) = F \, \delta x(t) + G(t)W(t)$$

where F is now the dynamic matrix for a system with state vector consists of the perturbed states, δx.

The main states to be estimated are the error in the quaternion parameters which can be given by:

127

$$\delta q = \begin{bmatrix} \delta q_1 & \delta q_2 & \delta q_3 & \delta q_4 \end{bmatrix}^T \tag{5.22}$$

The quaternion parameters are primarily determined using the angular rates obtained from gyroscopes' measurements. The deterministic errors associated with the gyroscope can be compensated using data from static interval at the beginning of the test while the stochastic errors in biases, $b_{\omega x}$, $b_{\omega y}$, and $b_{\omega z,}$ are given by:

$$b_\omega = \begin{bmatrix} \delta \omega_x & \delta \omega_y & \delta \omega_z \end{bmatrix}^T = \begin{bmatrix} b_{\omega x} & b_{\omega y} & b_{\omega z} \end{bmatrix}^T \tag{5.23}$$

The complete state vector is defined as a 7-dimensional vector with the first four components being errors in quaternion elements and the last three being the elements of the gyroscope biases.

$$x = \begin{bmatrix} \delta q & b_\omega \end{bmatrix}^T = \begin{bmatrix} \delta q_1 & \delta q_2 & \delta q_3 & \delta q_4 & b_{\omega x} & b_{\omega y} & b_{\omega z} \end{bmatrix}^T \tag{5.24}$$

5.3.2 The States Transition Model

The quaternion derivative is used for estimating the attitude using angular rate measurements. The angular rate is linked to the quaternion parameters as in Equation (5.25)

$$\dot{q} = \frac{1}{2} \cdot q \otimes \omega = \frac{1}{2} \begin{bmatrix} -q_2 & -q_3 & -q_4 \\ q_1 & -q_4 & q_3 \\ q_4 & q_1 & -q_2 \\ -q_3 & q_2 & q_1 \end{bmatrix} \begin{bmatrix} \omega_x \\ \omega_y \\ \omega_z \end{bmatrix} \tag{5.25}$$

Where q is the orientation quaternion, $\otimes$ represents quaternion representation, and ω_x, ω_y, and ω_z represent angular rate measurements in the sensor frame obtained using the rate gyroscopes. Quaternions are used to represent orientation in the filter design because do not have the singularity problem commonly associated with Euler angles. The previous equation can be rewritten as:

$$
\begin{bmatrix} \dot{q}_1 \\ \dot{q}_2 \\ \dot{q}_3 \\ \dot{q}_4 \end{bmatrix} = \frac{1}{2} \begin{bmatrix} -q_2\omega_x - q_3\omega_y - q_4\omega_z \\ q_1\omega_x - q_4\omega_y + q_3\omega_z \\ q_4\omega_x + q_1\omega_y - q_2\omega_z \\ -q_3\omega_x + q_2\omega_y + q_1\omega_z \end{bmatrix} \tag{5.26}
$$

The Taylor series expansion to first order is shown in Equation (5.27).

$$
\delta\dot{r} = \frac{\partial \dot{r}}{\partial r} \delta r \tag{5.27}
$$

Where r is the state vector, δr is the error in the state. Thus, the quaternion parameters error can be obtained as:

$$
\begin{bmatrix} \delta\dot{q}_1 \\ \delta\dot{q}_2 \\ \delta\dot{q}_3 \\ \delta\dot{q}_4 \end{bmatrix} = \frac{1}{2} \begin{bmatrix} 0 & -\omega_x & -\omega_y & -\omega_z \\ \omega_x & 0 & \omega_z & -\omega_y \\ \omega_y & -\omega_z & 0 & \omega_x \\ \omega_z & \omega_y & -\omega_x & 0 \end{bmatrix} \begin{bmatrix} \delta q_1 \\ \delta q_2 \\ \delta q_3 \\ \delta q_4 \end{bmatrix} \tag{5.28}
$$

A general equation for the 1st order Gauss-Markov model is given as:

$$
\dot{b} = -\beta b + \sqrt{2\beta\sigma^2}\, w \tag{5.29}
$$

Where β is the reciprocal of the correlation time and σ^2 is the variance of the gyroscope signal.

The different parameters of the Gauss-Markov model can be determined as shown in Figure 5.4.

The real gyroscope data is plotted in Figure 5.5 with the fitted Gauss-Markov curve.
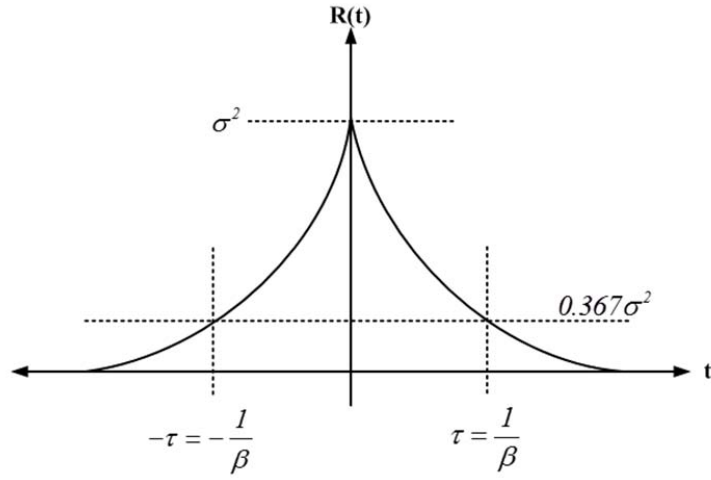
Figure 5.4: Signal correlation and Gauss-Markov parameters
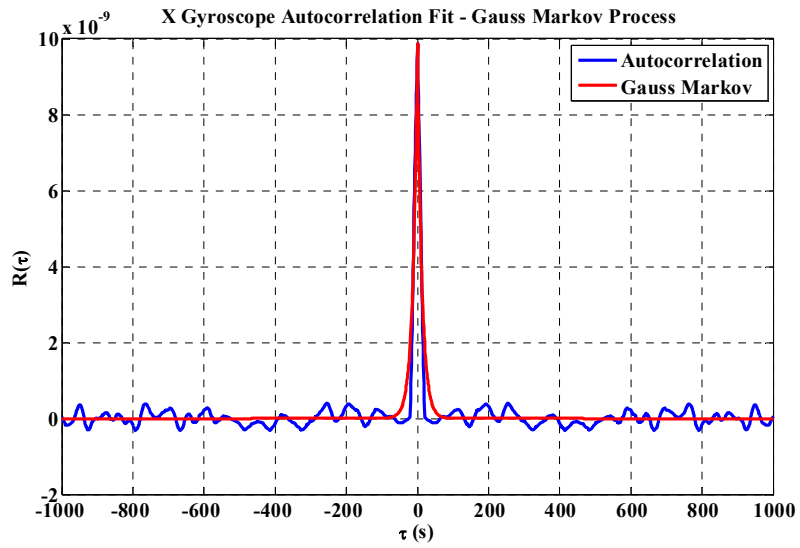
Figure 5.5: Autocorrelation fit for X gyroscope

From the exponential fit Figure 5.5, Gauss Markov process variance σ^2 time constant τ are computed for gyroscopes and tabulated in Table 5.3:

Table 5.3: Gauss-Markov parameters for the gyroscopes

		σ_ω	τ
Gyroscope	X	9.86×10^{-9} (rad/s)^2	12.6 s
	Y	1.37×10^{-8} (rad/s)^2	37.5 s
	Z	6.64×10^{-9} (rad/s)^2	13.05 s

According to Equation (5.29), the gyroscopes bias can be modeled as:

$$\dot{b}_\omega = \begin{bmatrix} \dot{b}_{\omega x} \\ \dot{b}_{\omega y} \\ \dot{b}_{\omega z} \end{bmatrix} = \begin{bmatrix} -\beta_x & 0 & 0 \\ 0 & -\beta_y & 0 \\ 0 & 0 & -\beta_z \end{bmatrix} \begin{bmatrix} b_{\omega x} \\ b_{\omega y} \\ b_{\omega z} \end{bmatrix} + \begin{bmatrix} \sqrt{2\beta_x \sigma_x^2} \\ \sqrt{2\beta_y \sigma_y^2} \\ \sqrt{2\beta_z \sigma_z^2} \end{bmatrix} w(t) \tag{5.30}$$

The complete state model can be written as Equation (5.31) :

$$\underbrace{\begin{bmatrix} \delta\dot{q}_1 \\ \delta\dot{q}_2 \\ \delta\dot{q}_3 \\ \delta\dot{q}_4 \\ \dot{b}_{\omega x} \\ \dot{b}_{\omega y} \\ \dot{b}_{\omega z} \end{bmatrix}}_{\delta\dot{x}} = \underbrace{\begin{bmatrix} 0 & -\omega_x/2 & -\omega_y/2 & -\omega_z/2 & 0 & 0 & 0 \\ \omega_x/2 & 0 & \omega_z/2 & -\omega_y/2 & 0 & 0 & 0 \\ \omega_y/2 & -\omega_z/2 & 0 & \omega_x/2 & 0 & 0 & 0 \\ \omega_z/2 & \omega_y/2 & -\omega_x/2 & 0 & 0 & 0 & 0 \\ 0 & 0 & 0 & 0 & -\beta_x & 0 & 0 \\ 0 & 0 & 0 & 0 & 0 & -\beta_y & 0 \\ 0 & 0 & 0 & 0 & 0 & 0 & -\beta_z \end{bmatrix}}_{F} \cdot \underbrace{\begin{bmatrix} \delta q_1 \\ \delta q_2 \\ \delta q_3 \\ \delta q_4 \\ b_{\omega x} \\ b_{\omega y} \\ b_{\omega z} \end{bmatrix}}_{\delta x} + \underbrace{\begin{bmatrix} 0 \\ 0 \\ 0 \\ 0 \\ \sqrt{2\beta_x \sigma_x^2} \\ \sqrt{2\beta_y \sigma_y^2} \\ \sqrt{2\beta_z \sigma_z^2} \end{bmatrix}}_{G} \cdot w(t) \tag{5.31}$$

Let Δt be the interval and using the dynamic matrix F in Equation (5.31), the state transition matrix can be defined as

$$\Phi_{k+1,k} = e^{(F \cdot \Delta t)} = I + F \cdot \Delta t \tag{5.32}$$

131

$$\Phi_{k+1,k} = \begin{bmatrix} 1 & \dfrac{-\omega_x}{2}\Delta t & \dfrac{-\omega_y}{2}\Delta t & \dfrac{-\omega_z}{2}\Delta t & 0 & 0 & 0 \\[2ex] \dfrac{\omega_x}{2}\Delta t & 1 & \dfrac{\omega_z}{2}\Delta t & \dfrac{-\omega_y}{2}\Delta t & 0 & 0 & 0 \\[2ex] \dfrac{\omega_y}{2}\Delta t & \dfrac{-\omega_z}{2}\Delta t & 1 & \dfrac{\omega_x}{2}\Delta t & 0 & 0 & 0 \\[2ex] \dfrac{\omega_z}{2}\Delta t & \dfrac{\omega_y}{2}\Delta t & \dfrac{-\omega_x}{2}\Delta t & 1 & 0 & 0 & 0 \\[2ex] 0 & 0 & 0 & 0 & 1-\beta_x\Delta t & 0 & 0 \\[1ex] 0 & 0 & 0 & 0 & 0 & 1-\beta_y\Delta t & 0 \\[1ex] 0 & 0 & 0 & 0 & 0 & 0 & 1-\beta_z\Delta t \end{bmatrix} \tag{5.33}$$

5.3.3 The Measurements Model

The update is designed to be performed at every detected step. The magnetometer measurements along with the accelerometer data are used for the update process in the Kalman filter. The measured magnetic field is tested for any perturbations. Once the magnetic field is free of disturbances, the geomagnetic heading is estimated based on the calibrated data. The accelerometer measurements are noisy since low-cost MEMS sensors are used and usually measured at higher rates. Therefore, the average of the measured data over the step time is used to estimate the roll and pitch values. The roll, pitch, and heading estimates are used to calculate the quaternion parameters using Equations (5.11) to (5.14). The only source of update is the quaternion parameters. Thus, the design matrix can be set as in Equation (5.34):

$$\delta z = \begin{bmatrix} \delta q_1 \\ \delta q_2 \\ \delta q_3 \\ \delta q_4 \end{bmatrix} = \begin{bmatrix} 1 & 0 & 0 & 0 & 0 & 0 & 0 \\ 0 & 1 & 0 & 0 & 0 & 0 & 0 \\ 0 & 0 & 1 & 0 & 0 & 0 & 0 \\ 0 & 0 & 0 & 1 & 0 & 0 & 0 \end{bmatrix} \cdot \begin{bmatrix} \delta q_1 \\ \delta q_2 \\ \delta q_3 \\ \delta q_4 \\ b_{\omega x} \\ b_{\omega y} \\ b_{\omega z} \end{bmatrix} \tag{5.34}$$

5.3.4 Modeling of Process and Measurement Noises

In order to complete the design of the KF, it is necessary to define the noise covariance matrices; the process noise covariance matrix Q and the measurement noise covariance matrix R. These matrices reflect the confidence in the system model and the measurements respectively. The covariance of w_k is often called the process noise matrix, Q_k, and can be computed as:

$$5.3.4.1.1.1.1.1 \quad Q_k = E\left[w_k \cdot w_k^T \right] \quad 5.3.4.1.1.1.1.2 \tag{5.35}$$

The Q_k matrix is a 7-dimension square matrix which can be computed using as in Equation (5.36) (Brown & Hwang 1992; Gelb 1974).

$$Q_k = \int_{t_k}^{t_{k+1}} \Phi_{t_{k+1},\tau} \cdot G(\tau) \cdot Q(\tau) \cdot G^T(\tau) \Phi_{t_{k+1},\tau}^T d\tau \tag{5.36}$$

The measured noise covariance matrix R also known as the covariance matrix for v. The R_k matrix represents the level of confidence placed in the accuracy of the measurements, and is given by:

$$R_k = E\left[v_k \cdot v_k^T \right] \tag{5.37}$$

133

The R_k matrix is a 4-dimension diagonal square matrix. The diagonal elements are the variances of the individual measurements, which can be determined experimentally using measurement data from the used sensors.

5.3.5 Filter State Initialization

The state vector should be initialized at the beginning of the process. For the gyroscope bias states, all biases are initialized as zeros. The quaternion states can be initialized from the DCM matrix using the Euler angles. The mean of the accelerometer calibrated data during a stationary period can be used to estimate the initial roll and pitch using the following relationships (Luinge & Veltink 2005):

$$\phi_o = tan^{-1}\left(\frac{-\bar{f}_y}{\sqrt{\bar{f}_x^2 + \bar{f}_z^2}}\right) \qquad \theta_o = tan^{-1}\left(\frac{\sqrt{\bar{f}_x^2 + \bar{f}_y^2}}{-\bar{f}_z}\right) \tag{5.38}$$

Where $\bar{f}_x, \bar{f}_y, \bar{f}_z$ are the mean values of the accelerometer data. ϕ_o and θ_o represent the initial values of the roll and pitch angles respectively. During the same interval, the roll and pitch estimates are used for levelling the magnetometer data to be in the navigation frame. The calibrated magnetometer data is used to estimate the initial azimuth ψ_o as in Equation (5.16):

The DCM is calculated using the initial Euler angles values as in Equation (5.3). Then, the relation between the quaternion and the Euler angles is used to calculate the initial quaternion vector.

134

$$q = \begin{bmatrix} c\,\bar{\phi}\,c\,\bar{\theta}\,c\bar{\psi} \; + \; s\,\bar{\phi}s\bar{\theta}\,s\bar{\psi} \\ s\bar{\phi}\,c\,\bar{\theta}\,c\bar{\psi} \; - \; c\,\bar{\phi}s\bar{\theta}\,s\bar{\psi} \\ c\,\bar{\phi}s\bar{\theta}\,c\bar{\psi} \; + \; s\,\bar{\phi}\,c\,\bar{\theta}\,s\bar{\psi} \\ c\,\bar{\phi}\,c\,\bar{\theta}\,s\bar{\psi} \; - \; s\,\bar{\phi}s\bar{\theta}\,c\bar{\psi} \end{bmatrix} \qquad where \; \bar{\phi} = \frac{\phi}{2}, \; \bar{\theta} = \frac{\theta}{2}, and \; \bar{\psi} = \frac{\psi}{2} \qquad (5.39)$$

Where **c** is used for *cos* and **s** for *sine*. The initial value of the quaternion vector q is calculated at the initial values of the roll, pitch, and azimuth. Equation (5.39) (Kuipers 1999) is also used to get the updated quaternion parameters.

5.4 Misalignment Effect on the Heading Estimation

Misalignment and boresight angles refer to the angle in the horizontal plane between the platform, pedestrian or vehicle, motion direction and the device direction. The direction of the pedestrian and the device are defined by the direction of their respective forward axis. In case the user remains in a given mode during the navigation, their direction can be acquired by estimating the horizontal components of acceleration. However, changing the orientation of the device during the navigation process requires estimating the change in the heading of the device with respect to the user direction of motion. As a result, the derived heading from the different sensors will not be enough to navigate the user as the misalignment angle will have to be compensated. A change in the axes definition will also not be suitable for the Kalman filter operation. Estimating the misalignment angle is a challenging process as the device can be held in any orientation with respect to the user body. The signal of the low cost MEMS sensors, commonly used in PNDs, is very noisy and requires considerable effort in the preprocessing operation.

During everyday use, a pedestrian will be required to carry the PND in different orientations. Reading/texting, ear talking, and belt tethering are common orientations for the device with respect to the user's body. Reading/texting has a negligible misalignment between the device's forward axis and the motion direction of the user at the horizontal level frame since both user and device have the same forward direction. In this scenario, the device's forward axis is aligned closely with the user's forward motion and boresight may be neglected. However, other orientations such as ear talking and belt produce a misalignment angle, as the forward axis of the device is not aligned with the user's motion direction. Such changes should conform to the heading changes of the human body about the vertical axis, when a hand-held device/smartphone, is used for navigation. Roll and pitch angles are permitted to change during motion, as these can be estimated in real-time using a suitable orientation filter used for levelling or de-tilting of sensors (transforming the sensor frame measured readings into LLF). The roll and pitch angles can be estimated from quaternion mathematics as in Equation (5.13) and Equation (5.14) respectively.

The normal usage of the PND as in reading/texting (compass) does not cause any problems for heading estimation as the device is aligned in the same direction of the user. Therefore, the misalignment angle is zero as both device and user have the same forward direction.

Figure 5.6 shows the frame orientation for the user and the device where the subscripts d and p denote device and pedestrian frames respectively.

(a) Pedestrian frame   **(b) Device (s-frame) frame**   **(c) Misalignment angle**
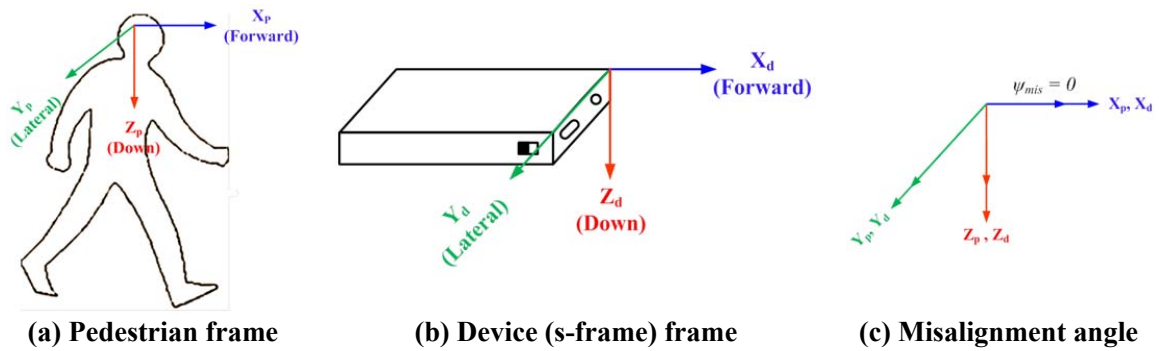
Figure 5.6: Reading/Texting misalignment definition

In the case of ear talking and belt, the situation is different as the misalignment angle can't be neglected. The device in each case has a forward direction different than the user's motion direction. Figure 5.7 and Figure 5.8 show the frame orientation for each case with the expected misalignment angle.

(a) Ear talking mode   **(b) Device orientation after leveling**   **(c) Misalignment angle**
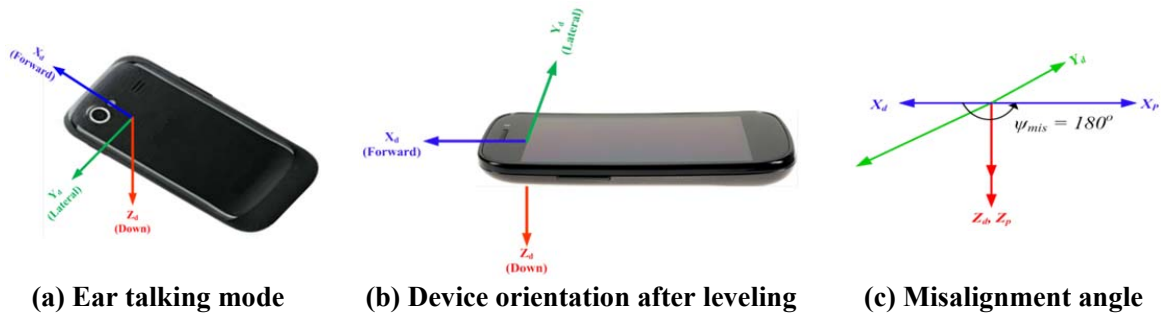
Figure 5.7: Ear talking misalignment definition

(a) Belt tethering mode   (b) Device orientation after leveling   (c) Misalignment angle
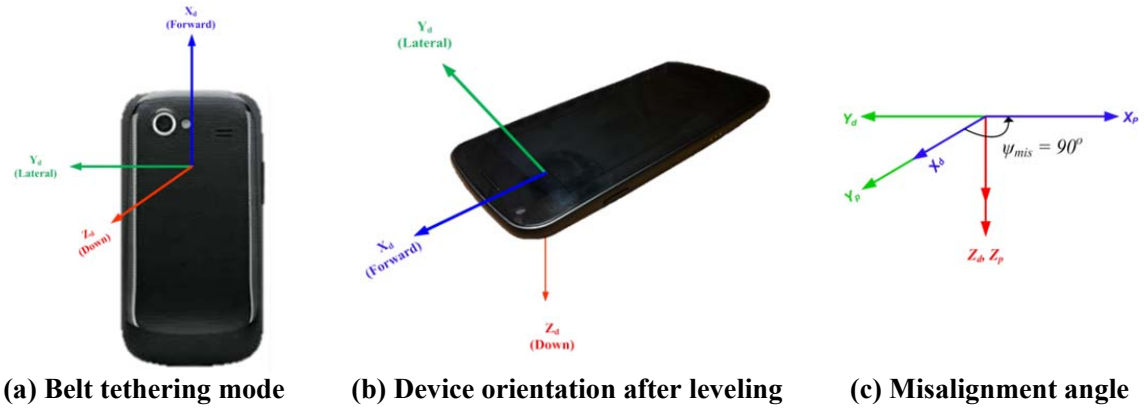
Figure 5.8: Belt tethering misalignment definition

Table 5.4 shows the expected values for the roll and pitch with each orientation. It also presents the expected misalignement angle for each orientation to be compenated for the device heading in the attempt to povide user heading.

Table 5.4: Expected roll and pitch values for the different orientations

Orientation	Roll	Pitch	Misalignment
	ϕ	θ	ψ_{mis}
Compass/Texting/Reading	$\approx 0^{\circ}$	$\approx 0^{\circ}$	$\approx 0^{\circ}$
Ear Talking	$\approx -90^{\circ}$	$\approx 0^{\circ}$	$\approx 180^{\circ}$
Belt	$\approx 0^{\circ}$	$\approx 90^{\circ}$	$\approx 90^{\circ}$

During the transition from one mode to another, the heading estimation process became a challenging task. In order to overcome this difficulty, a suitable coordinate transformation was performed by acquiring the axis orientation, which is closer or parallel to gravity vector as shown in Figure 5.9. Clearly, the coordinate transformation matrix for ear talking and belt to achieve the transformation task, with pedestrian frame as reference are given by Equations (5.40) and (5.41)

138

respectively. The original equation for heading estimation can now be used based on the knowledge of the above transformation.

$$
\begin{bmatrix} new\_x_{d\_ear} \\ new\_y_{d\_ear} \\ new\_z_{d\_ear} \end{bmatrix} = \begin{bmatrix} -1 & 0 & 0 \\ 0 & 0 & 1 \\ 0 & 1 & 0 \end{bmatrix} \begin{bmatrix} x_d \\ y_d \\ z_d \end{bmatrix}
\tag{5.40}
$$

$$
\begin{bmatrix} new\_x_{d\_belt} \\ new\_y_{d\_belt} \\ new\_z_{d\_belt} \end{bmatrix} = \begin{bmatrix} 0 & -1 & 0 \\ 0 & 0 & 1 \\ -1 & 0 & 0 \end{bmatrix} \begin{bmatrix} x_d \\ y_d \\ z_d \end{bmatrix}
\tag{5.41}
$$

Figure 5.9 shows an example of mode switching where the device orientation changes from compass to ear taking and belt tethering. As shown in the figure, the sensor axes changed according to the orientation of the device. This change produced different values for the gravity vector axes other than the z-axis. Also, the forward axis should have been redefined to match the new orientation of the device. However, the axis transformation based on Equations (5.40) and (5.41) returned the device to the normal orientation to be matched with the original frame definition as x is the forward axis and axis z represents the gravity vector.
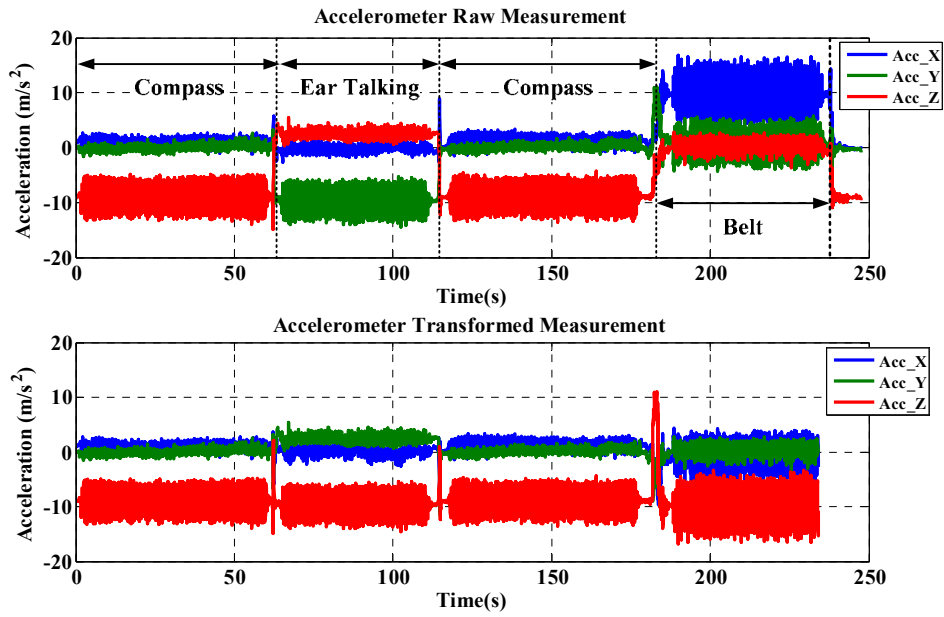
(a) Accelerometers data
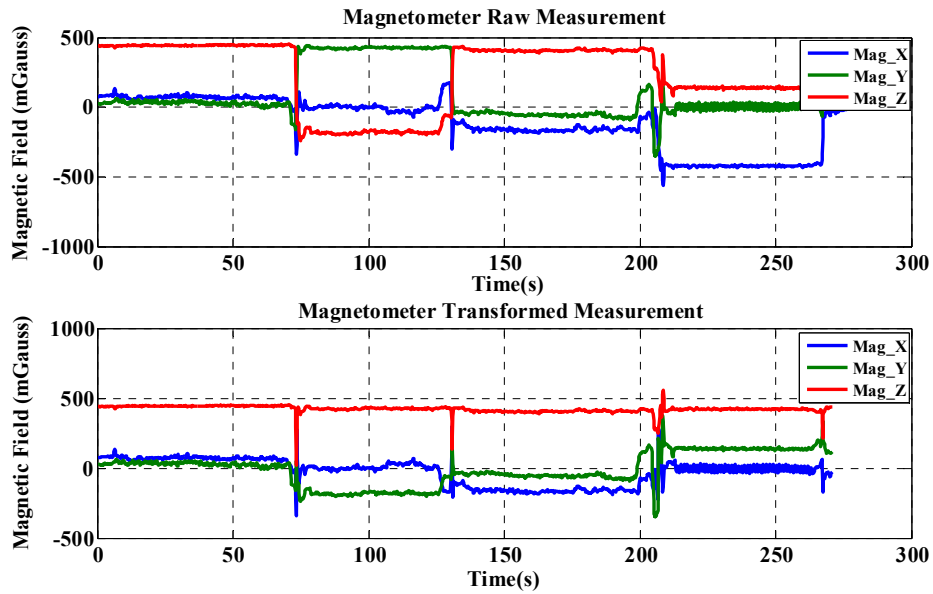
(b) Magnetometers data

Figure 5.9: Sensors data before and after axes transformation

Chapter Six: Proposed PDR Technique: Performance and Assessment

The purpose of this chapter is to test and assess the proposed PDR technique. The chapter begins with the description of the platform and sensors used in the field tests. The sensor specs are illustrated with the accuracy of the measured data and the associated rates. The chapter also includes the possible ways to initialize the PDR algorithm and the criteria for selecting the different field tests and environments. Finally, the overall performance of the proposed PDR algorithm is presented.

6.1 Sensors Specifications and Selection

Two main terms used in this thesis should be defined: the platform and the navigation device. The navigation device is defined as the integrated sensors necessary for estimating the platform navigation parameters. Most smartphones and tablets nowadays are the typical navigation device since they contain many navigation sensors. In general, the device is commonly tethered to the platform. An example of these platforms may be the pedestrian, a vehicle or an aircraft. For the purpose of this research, the platform refers to the pedestrian.

Recently, MEMS technology has allowed for the production of low-cost, small size, and lightweight inertial sensors that consume very little making them appropriate for mobile navigation devices. However, MEMS sensors exhibit very high noise and large error drifts. Therefore, they have not been widely used for navigation applications. In order to reduce the deterministic and the stochastic errors of MEMS sensors, compensation techniques must be

developed and implemented. The previous chapters described various calibration techniques for the output of the sensors. The concept of gyroscope calibration is illustrated in Chapter 5 while Chapters 3 and 4 describe in detail the process of magnetometer calibration and the necessary conditions to improve its overall performance.

Some sensors manufacturers provide stochastic information for the error sources, which can be exploited in the sensors calibration process. Therefore, this information can be used as a starting point for any further calibrations or as rough estimates about the performance of the sensors since they represent averages for the hardware performances of thousands or millions of similar units. On average, some individual units might perform better or worse than what is stated by the manufacturers depending on the accuracy of individual calibrations. Therefore, estimating the required parameters not only depends on the calibration algorithm but also on the selection of the necessary information sources for navigation (sensors).

Several tests were conducted in order to validate the proposed PDR technique. The tests included different trajectories, specifically normal human walking behaviour using a low-cost mobile navigation device. The device used in the test was a Samsung Galaxy Nexus smartphone, depicted in Figure 6.1. It was equipped with sensors such as GPS receiver, a triad magnetometer (M), a triad gyroscope (G), a triad accelerometer (A), a barometer, and a temperature sensor. The focus however, will be on the sensor trio (M-G-A) since they can provide all the necessary navigation parameters in the absence of GPS information.

Figure 6.1: Samsung Galaxy Nexus smartphone

In order to show the performance of the M-G-A sensors, the GPS satellites were used in some tests to obtain a reference trajectory; however this data is not included in the solution. The manufactures and the ranges of the main sensors are listed below in Table 6.1.

Table 6.1: The main operating characteristics of the used sensors

Sensor	Manufacture	Parameter	Typical
Gyroscope	InvenSense MPU-3050	Dynamic Range	±250, ±500, ±1000, ±2000 $°/sec$
		Word Length	16-bit
		Zero-Rate Output	±20 $°/s$
		Total RMS Noise	0.1 $°/s$
		Operating Temperature	-40 : +85 $^o C$
		Practical Data Rate	20 Hz
Accelerometer	BOSCH BMA250	Sensitivity	±2, ±4, ±8, ±16 g
		Word Length	8-bit
		Zero-g Output	±80 mg
		Total RMS Noise	0.8 $mg/\sqrt{Hz}$
		Operating Temperature	-40 : +85 $^o C$
		Practical Data Rate	20 Hz
Magnetometer	YAMAHA YAS530	Magnetic Field Range	±800 μT
		Operating Temperature	-40 : +95 $^o C$
		Practical Data Rate	20 Hz

6.2 Test Preparation

This section explains the criteria for selecting the test environments. It also discusses the possible ways for initializing the various parameters of the PDR algorithm (namely position, heading, and orientation).

6.2.1 How to Select the Test Environment

The environment has a great impact on all navigation solution components such as the technique and methodology, the accuracy of the navigation solution and the sensors involved in the solution. In order to assess the proposed PDR algorithm, different tests were conducted in common environments. These environments were selected to cover a variety of areas that are important to pedestrians. The University of Calgary (UofC) Campus is one example for the test environment where students are moving from building to building, walking in high buildings or going to the food court via tunnels. In addition, some tests were conducted in the downtown quadrant of Calgary where many commercial and business attractions are located.

A group of tests are started outdoors and switched indoors while another group started indoors and switched outdoor. The 2nd floor of the CCIT building at UofC is an example of a steel structured environment (as shown in Figure 6.2) representative of a harsh environment appropriate for testing the performance of magnetometers. This environment was considered a good test area to evaluate the attitude estimation technique developed herein because it includes numerous magnetic field perturbation sources.

144
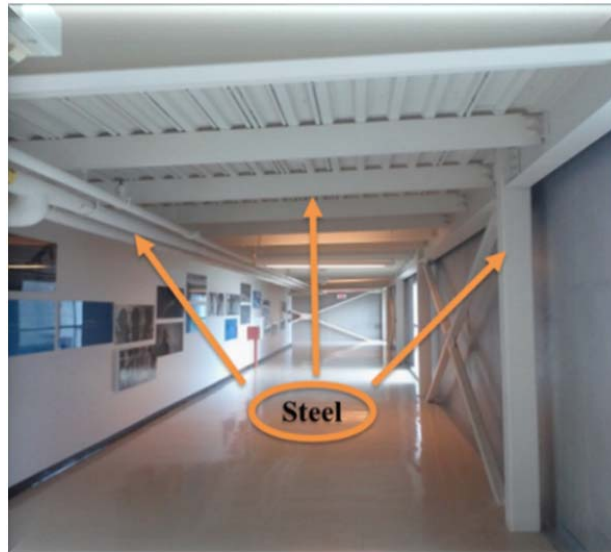
Figure 6.2: The structure at the CCIT 2nd floor

The Kinesiology Complex at the UofC is another test area that was selected as an indoor environment. It is an attractive area for students since it houses all sporting activities. The test track began outside the Olympic Oval where there is a big metal sculpture - the Spire (Figure 6.3) - made out of metal which effectively contributed to the magnetic field perturbations in this region.

Figure 6.3: The Spire

6.2.2 How to Initialize the PDR Algorithm

A large part of the tests was conducted outdoors due to the presence of a reference solution from GPS satellites. As the inertial sensors provide a relative solution, it is necessary to initialize the PDR solution. There were three main parameters required for the initial value prior to beginning the algorithm: initial position, initial heading, and initial orientation. (1) For the initial position, the GPS is used in outdoor scenarios while the position is initialized manually by the user in the absence of the GPS (e.g. if the test starts indoor). Also, Wi-Fi can be used to initialize the position by detecting the closest access point position. (2) The initial values for the roll and pitch angles can be determined from accelerometer data. For this purpose, stationary data acquired over approximately 30 s is collected at the beginning of the test. Alternatively, these values can be set manually by the user. (3) The initial heading can be determined according to the magnetometer data at the start of the test or manually by the user.

6.3 Step Detection and Length Estimation Accuracy

This section discusses the performance of the step detection algorithm and its accuracy. It shows the technique's efficiency in estimating the correct step length.

6.3.1 Step Detection Performance

Several data sets are collected to assess the proposed step detection algorithm. In these tests, the actual number of steps were counted by the user and used as a reference. For this purpose, the

step events are detected where the device is held in compass mode with normal walking. Different users are involved in the test to obtain different walking behaviours. The tracks are chosen based on turns and doors to simulate real walking conditions.

The results of this analysis are summarized in

Table 6.2 provides the comparison for the detected number of steps and reference number of steps. The number of un-detected steps appears with (-) sign and the number of over-detected steps appears with (+) sign. Also, the percentage accuracy of the step detection algorithm is calculated according to Equation (6.1).

$$Acurracy = (\frac{Detected\_Steps - Actual\_Steps}{Actual\_Steps}) \cdot 100\%$$
(6.1)

Table 6.2: Performance analysis of the step detection algorithm

Test	Steps		Wrong Steps	Error
	Ref.	Detected		
Test1	60	60	0	0 %
Test2	60	60	0	0 %
Test3	65	64	-1	-1.54 %
Test4	65	65	0	0 %
Test5	97	97	0	0 %
Test6	105	105	0	0 %
Test7	114	114	0	0 %
Test8	120	121	1	0.83 %
Test9	1032	1031	-1	-0.10 %
Test10	394	393	-1	-0.26 %
Total	2112	2108	4	0.19 %

It can be seen that the total accuracy of the step detection algorithm is higher than 99%. Among the ten tests, six tests have 100 % accuracy where only four contain errors. The maximum error

was one step up or under the correct number of steps. Finally, it is worth mentioning that the performance of the algorithm is high regardless of the type of activity performed by the pedestrian such that the algorithm successfully avoid the stationary periods, as indicated in Figure 6.4.
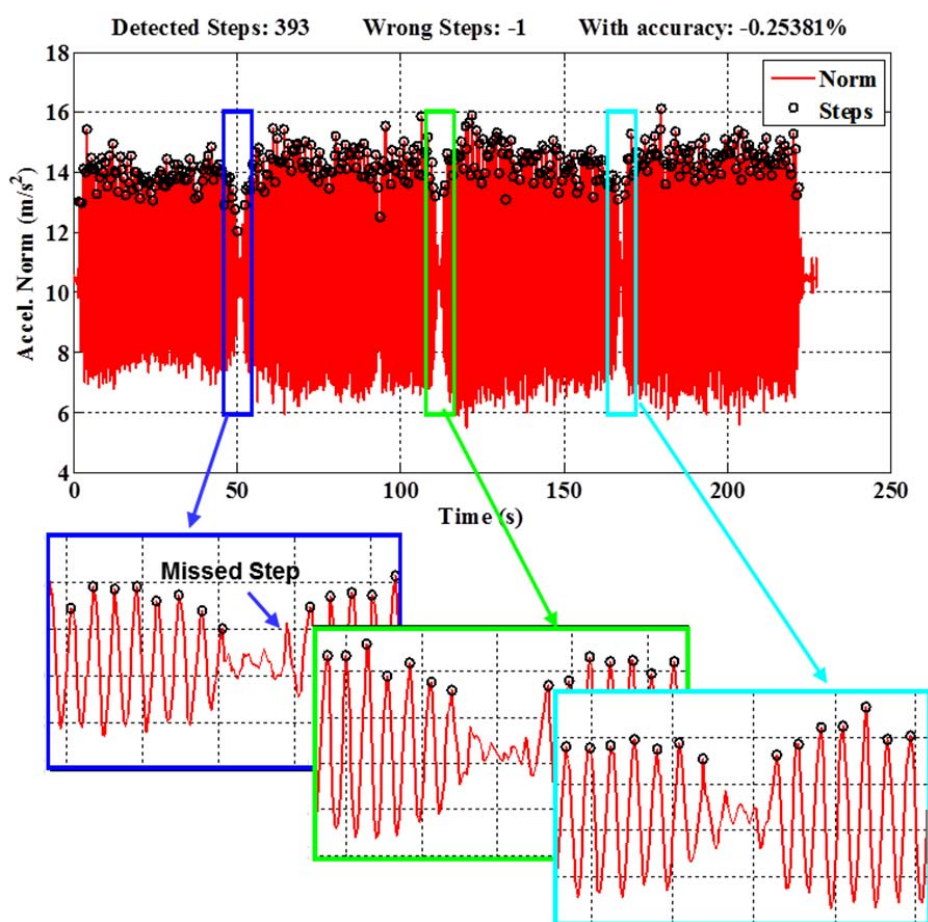

Figure 6.4: Example for step detection performance with turns

6.3.2 Step Length Estimation

Because the step length is not a constant value and changes with user's speed and walking behaviour, its value must be determined continuously during the walk to increase the PDR

148

algorithm's efficiency. The step length depends on the acceleration magnitude and the walking frequency. To evaluate the performance of the step length estimation technique, a group of tests were conducted with a pre-determined path.

Two trajectories were selected one with a 60 m length and another with a 120 m length. Each trajectory was repeated twice at slight difference in the walking speed. The true number of steps for the first trajectory was 79 in the first round and 83 steps in the second. For the second set, the true number of steps was 162 for both rounds.

The step length was determined as described in Chapter 2. Table 6.3 summarize the results for the step length estimation. The maximum error in the estimated distance is 2.87 m which is equivalent to 2.39% error of the total traveled distance.

Table 6.3: Performance analysis of the step length estimation technique

Normal Walking		Distance			
		Actual	Measured	Error	Ratio
Test1	Round1	60 m	60.95 m	+ 0.95 m	+ 1.58 %
	Round2	60 m	59.17 m	- 0.83 m	- 1.38 %
Test2	Round1	120 m	117.13 m	- 2.87 m	- 2.39 %
	Round2	120 m	118.36 m	- 1.64 m	- 1.37 %

Figure 6.5 shows the estimated step length. The mean estimated length is determined to be 77 cm and 71 cm for test 1 and 73 cm and 74 cm for test 2. These results verify that the proposed method can measure step length accurately.

(a) Test1

(b) Test2
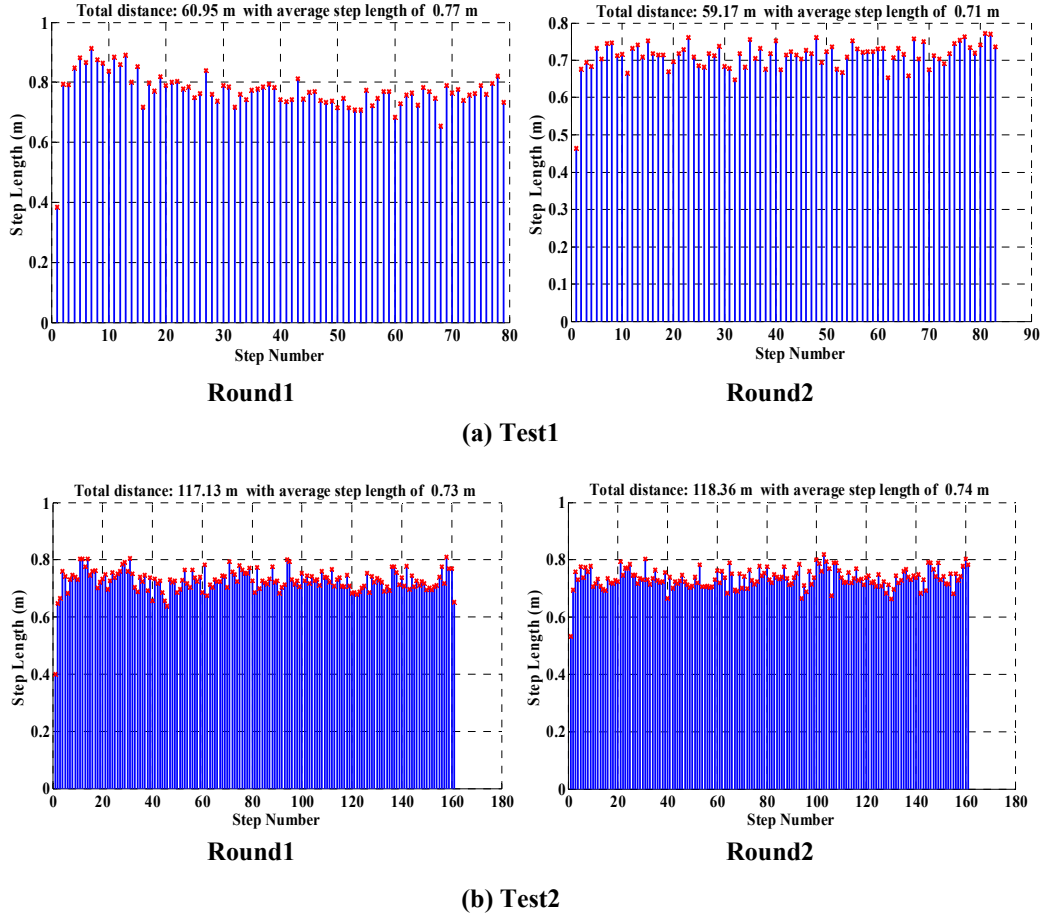
Figure 6.5: Estimated step length

6.4 PDR Algorithm Performance Evaluation

In this section, the performance of the proposed PDR algorithm is evaluated to demonstrate the accuracy of the orientation filter in estimating the device heading and orientation. Various tests are conducted in different environments such as indoor locations or parking lots full of cars. The user position was propagated based on the detected steps, estimated step length, and the heading. During all tests the device was held in the texting mode except in the switching mode test where the device was held in an ear talking and belt mode. Similar steps were followed at the beginning

150

of all tests; beginning with an approximately 30-second stationary period to calibrate for the gyroscope bias and when coordinated manoeuvring was performed to help in the magnetometer calibration process. For indoor and downtown tests, the initial position was defined by the user since GPS was practically unavailable in these areas. However, some GPS data was used to provide the user's initial position for the tests that were done in clear sky areas.

6.4.1 Indoor Test

The scenario for the indoor test is discussed to show the performance of the proposed PDR in the absence of the GPS update and to show the effect of the different infrastructures on the performance of the magnetometer. The test was conducted on the 2nd floor of the CCIT building, the University of Calgary. The device was held in the compass mode and the user moved freely throughout the second floor to reach the main office of the Department of Geomatics Engineering at building E. The total distance travelled was 231 m. The track was selected based on the following criteria:

- Long corridor with many turns to help assess the performance of the gyroscope.
- Majority of the building, particularly CCIT, composed of steel, which affects the performance of the magnetometer.
- Many doors to be opened in different areas of the track which forced the user to change his speed and step length simulating a real scenario of a walking person.

Due to the harsh conditions at the start of the test - absence of GPS and the presence of magnetic field perturbation—the PDR solution was initialized manually by the user for the position and heading.

The estimated heading from the magnetometer and the orientation filter are shown in Figure 6.6. The figure indicates that the magnetometer heading is strongly affected by the steel structures of the building and dense walls throughout many areas of the test. The distortion in the magnetic field was present for more than 40% of the total test time resulting in incorrect magnetometer-based heading estimation. As a result, the filter is propagated using the gyroscopes' measurements where the filter shows a strong performance during these intervals.
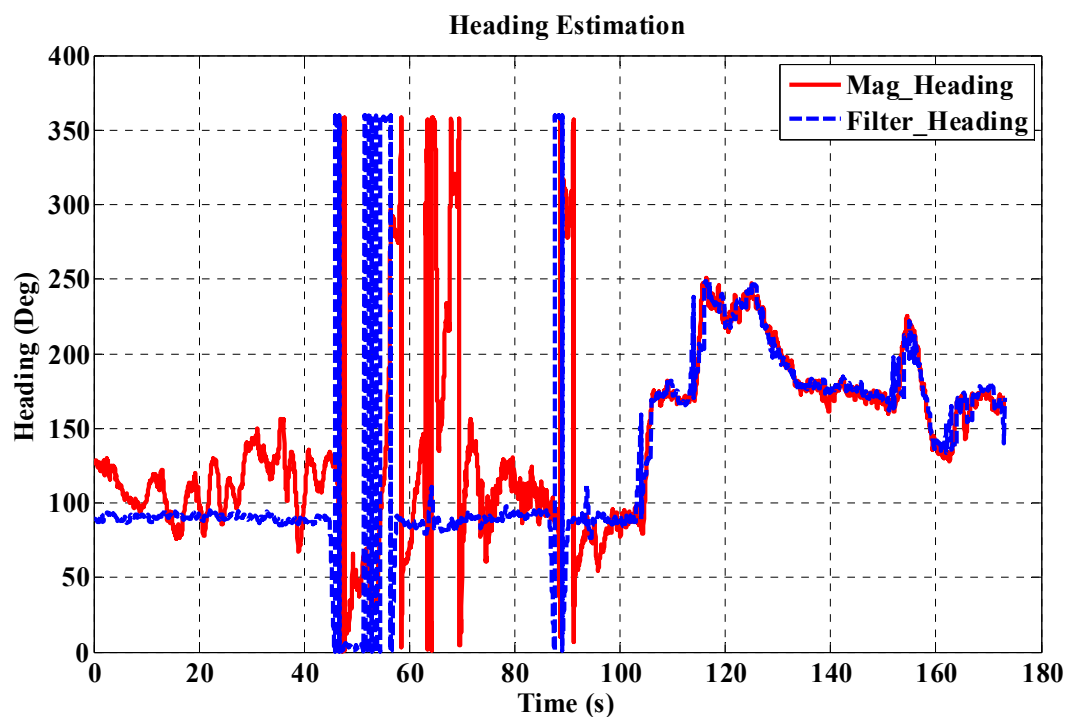

Figure 6.6: Heading estimation

Figure 6.7 shows a vector plot for a trajectory based on the filter and magnetometer stand-alone heading. The magnified portion establishes that the heading in the perturbation area is not uniform and is diverted due to the distortion in the magnetic field.
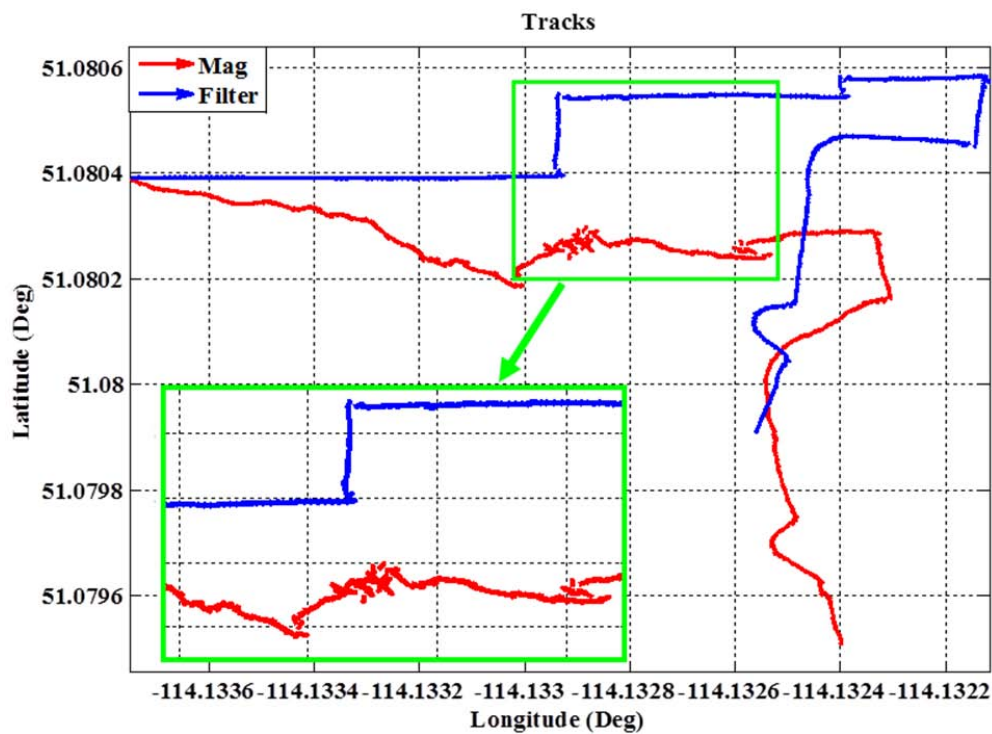
Figure 6.7: Magnetometer heading direction during perturbation area

Figure 6.8 shows a comparison between the PDR solution using the orientation filter and to the same solution based on the heading from the magnetometer stand-alone. The solution is plotted on a Google map to show the actual track travelled by the user during the test. The results on the figure suggest that the magnetometer-based PDR solution (in red) is inappropriate during movement in the steel structure while the orientation filter-based PDR solution (in blue) is propagated correctly in the same area.

153
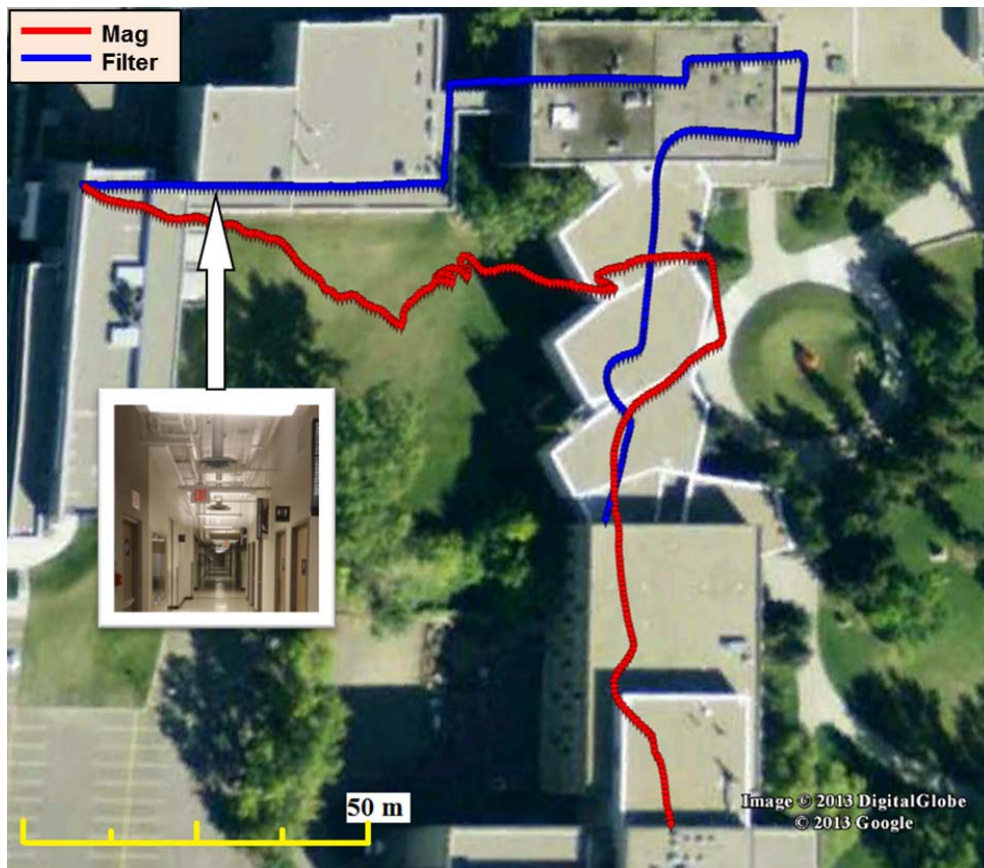
Figure 6.8: PDR solution using filter and magnetometer based heading plotted on Google map

The overall accuracy of the PDR solution is estimated by comparing it with a reference trajectory for the test track. The University of Calgary's interactive map is used to show the 2nd floor of the Schulich School of Engineering building In Figure 6.9, the trajectory ends with a position drift of about 12 m and the error in the distance is approximately 5.2 % of the total travelled distance. The error is high as a result of the harsh environment, which made the magnetometer data too unreliable for consistent use.

154
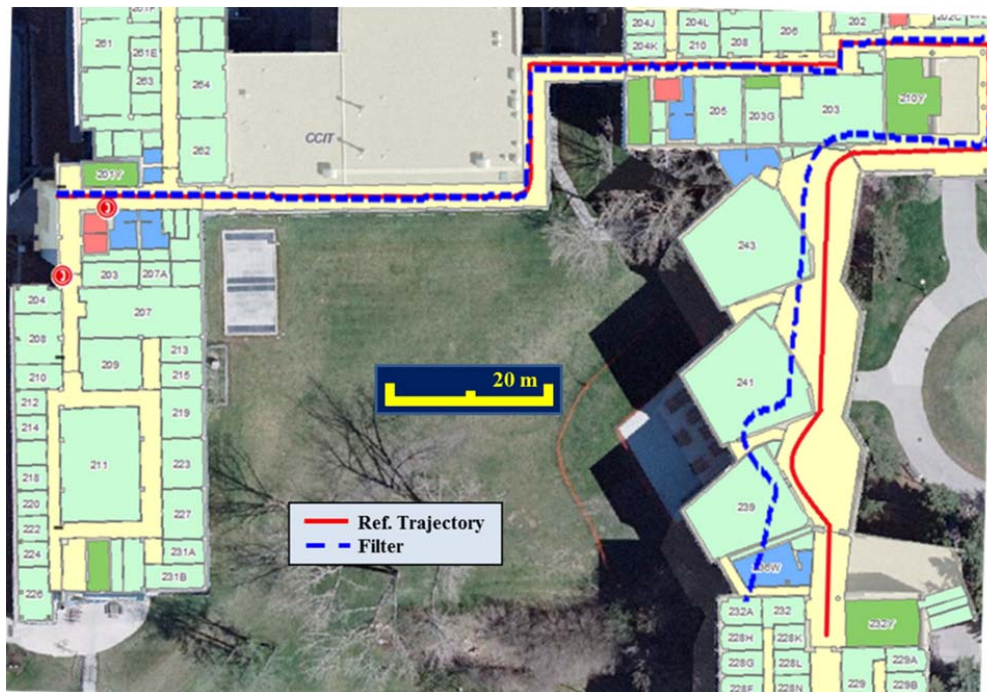
Figure 6.9: PDR trajectory compared to a reference trajectory

6.4.2 Environment Changing Test (from outdoor to indoor)

For the outdoor to indoor test, the scenario began close to the Olympic Oval at the University of Calgary. The PDR solution was initialized using an initial position from GPS and initial heading from the magnetometer. The device was held stationary at the beginning of the test for about 40 seconds to calibrate for the gyroscope deterministic bias and to estimate the initial orientation, roll, and pitch of the device. The user held the device in compass mode and moved through the first floor with a long corridor inside the building. The trajectory ended outside the McEwan Student Center in front of the Taylor Family Digital Library (TDFL). The time for this trajectory was about 5.5 minutes with 594 steps for a total travelled distance of 461 m. Several conditions made this location an ideal test candidate:

- It is a popular and attractive place for student activities.

- It has a long corridor, which is a challenging area for magnetometer.

- At the start of the test track, in front of the building, there is a huge metal structure that can affect the magnetometer's performance.

- The building is full of students and simulates a normal walking scenario of a smartphone user.

Figure 6.10 shows the detected steps during the test. The figure also shows the successful detection of the user steps at the entrance of the building where there were two consecutive doors. The maximized view in the figure demonstrates the performance of the step detection algorithm during a transition area between two doors. There two static intervals for the opening of the doors and four steps in between to move from the first to the second.
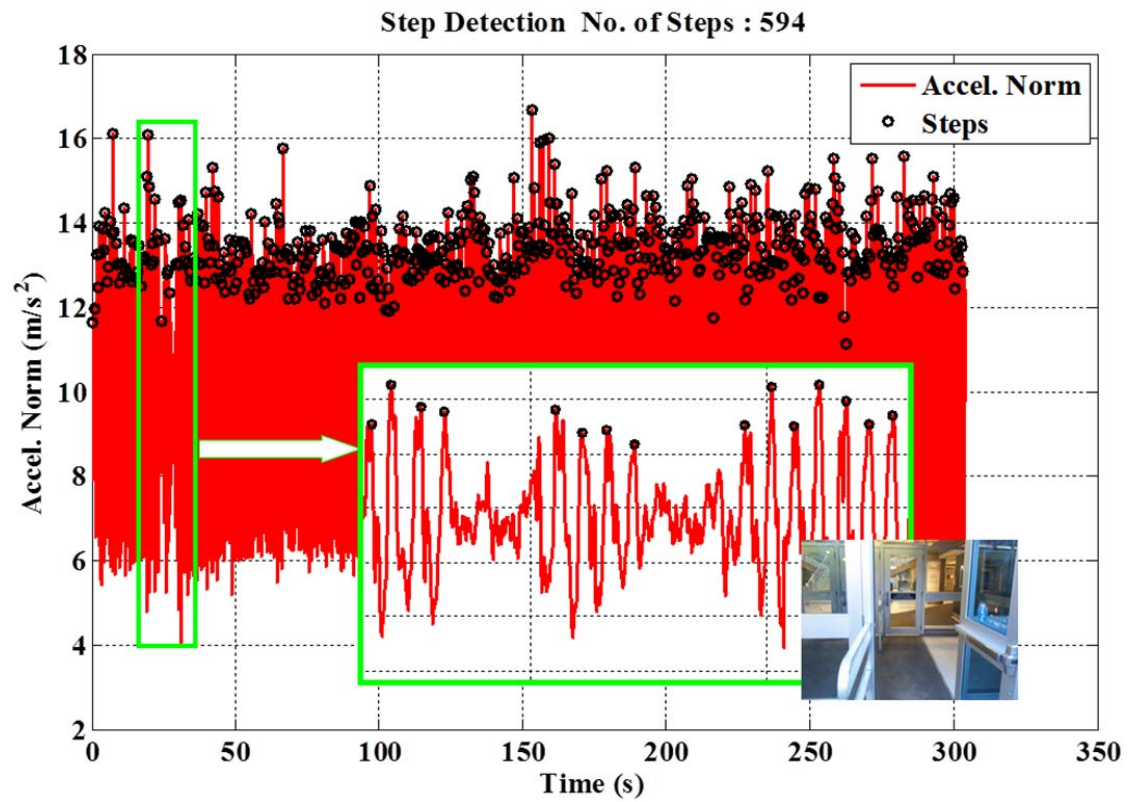
Figure 6.10: Steps detection

The step length varied with user speed as seen in Figure 6.11. At the entrance of the building it can be observed that the length the step is relatively small compared to the normal walking step length that occurred throughout the test. The average estimated step length was 78 cm for the overall test.
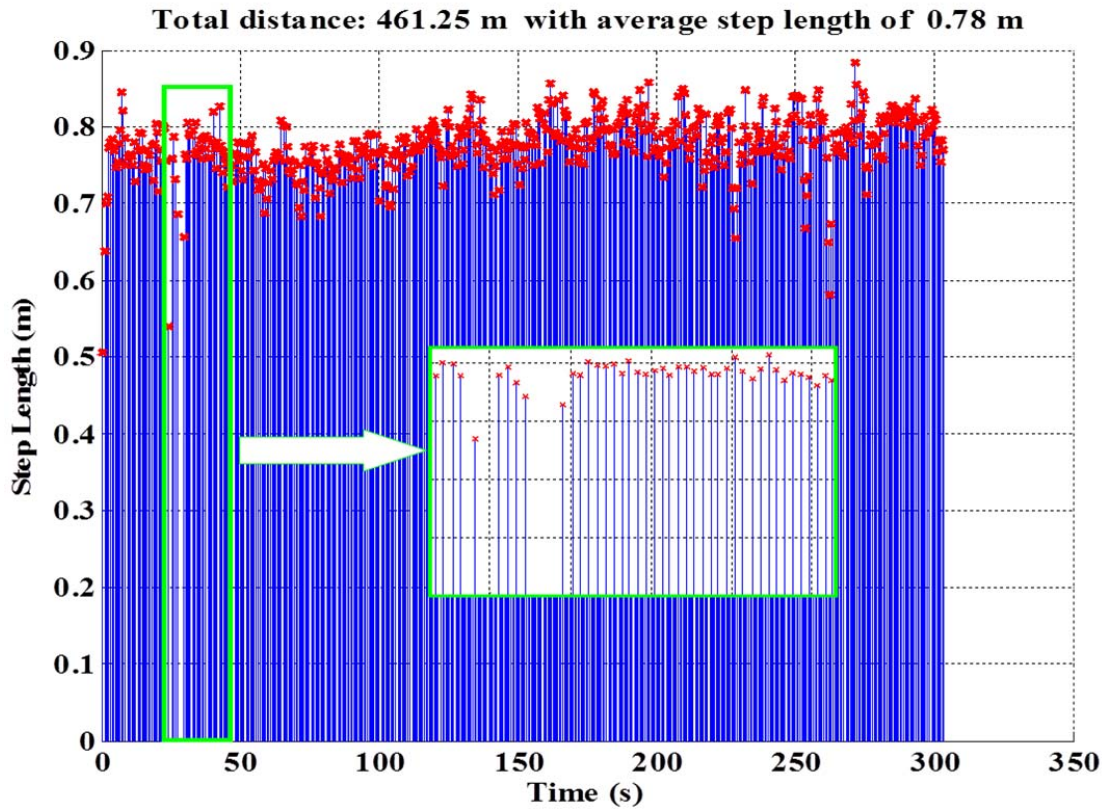
Figure 6.11: Step length estimation

The derived heading from the magnetometer was entirely affected at the beginning due to the presence of a huge metal object in the surrounding area. The total magnetic field was distorted yielding incorrect heading estimation from the magnetometer during the first 40 seconds of the test. In addition, the calibration process was performed according to data gathered from outside the building, so that once the user moved indoors the distribution of the magnetic field differed from what existed outside as shown in Figure 6.12. Therefore, magnetometer-based heading remained inaccurate. However, after approximately 2 minutes the heading from the magnetometer begins to act as main source of update for the orientation filter attitude. As a

result, during the perturbation interval the orientation filter does not perform the update stage and continues propagating the orientation of the device based on the gyroscopes' measurements.

Heading Estimation
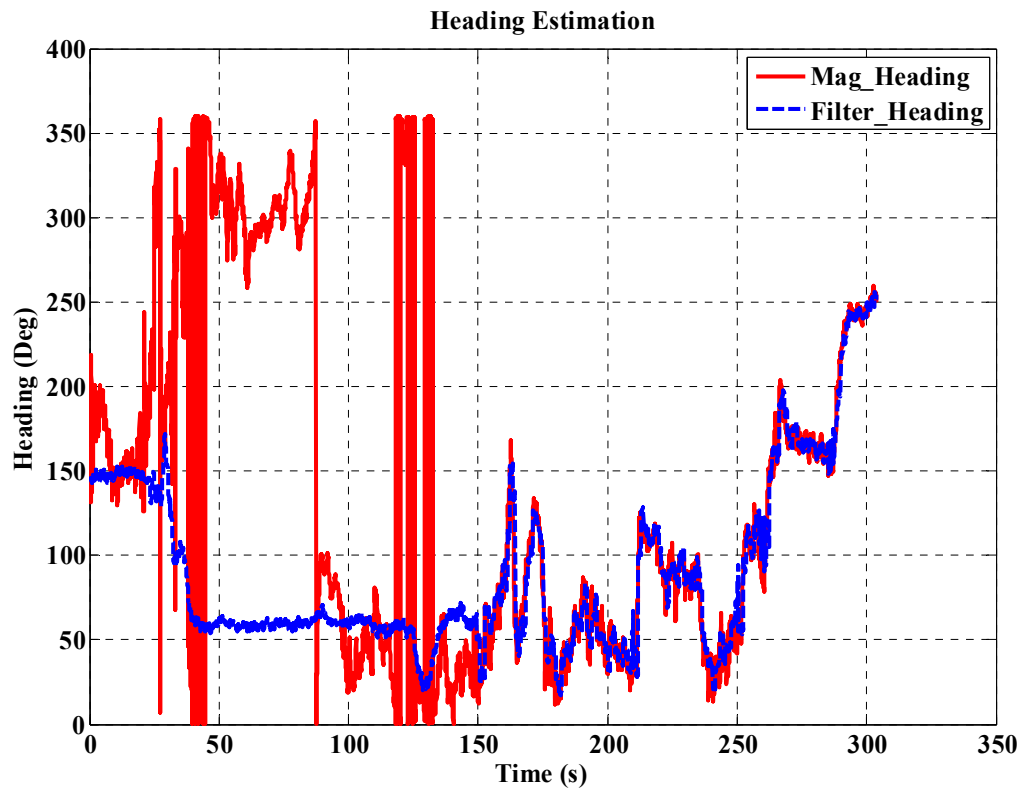
Figure 6.12: Heading estimation

The magnified portion of Figure 6.13 represents the magnetometer heading during the perturbation area. The figure shows that the heading is diverted and scattered when the magnetic field is distorted in contrast to the orientation filter heading during the same interval.
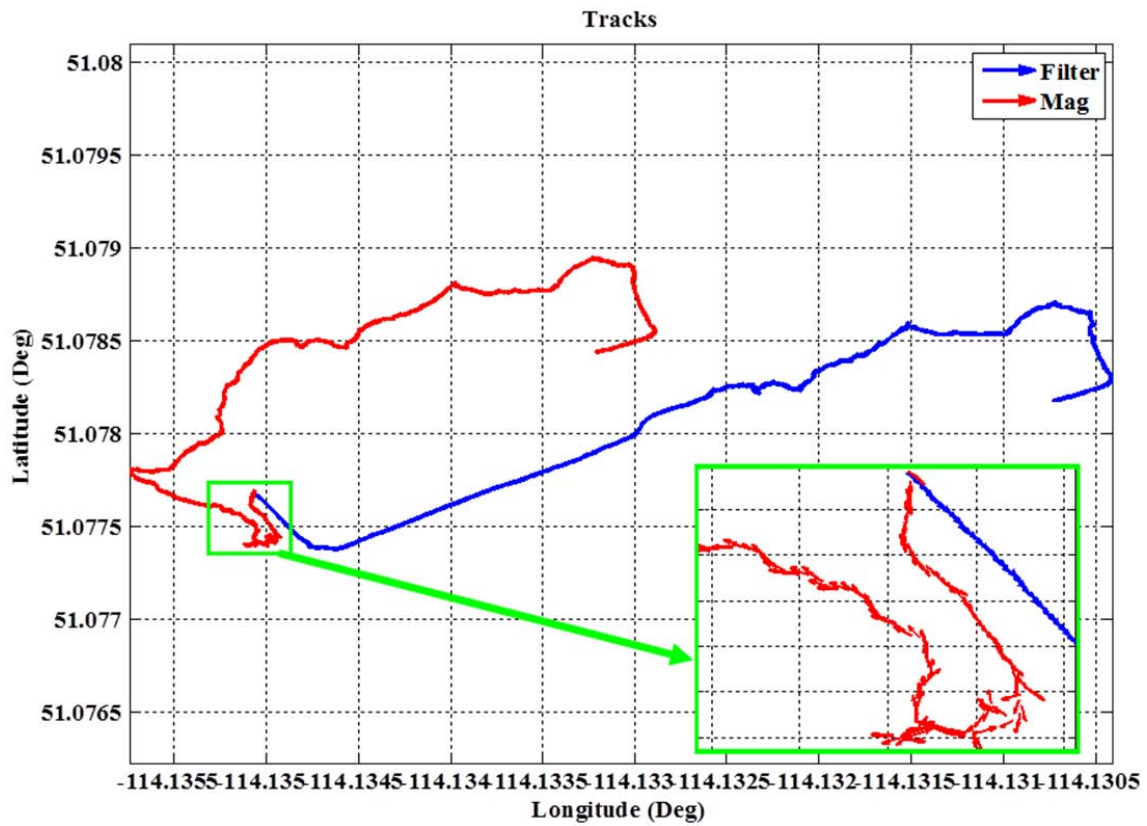
Figure 6.13: Magnetometer heading direction during perturbation area

The propagated user's position using the PDR technique is plotted on a Google map to show the real test track. Figure 6.14 shows the PDR solution using the orientation filter compared to the same solution based on the heading from the magnetometer stand-alone. It is clear that the trajectory at the beginning was messy and went in the wrong direction. However, the performance improved during time when no perturbations were present, as expected. In contrast, the filter performed well in tracking the correct direction of the user through the test.
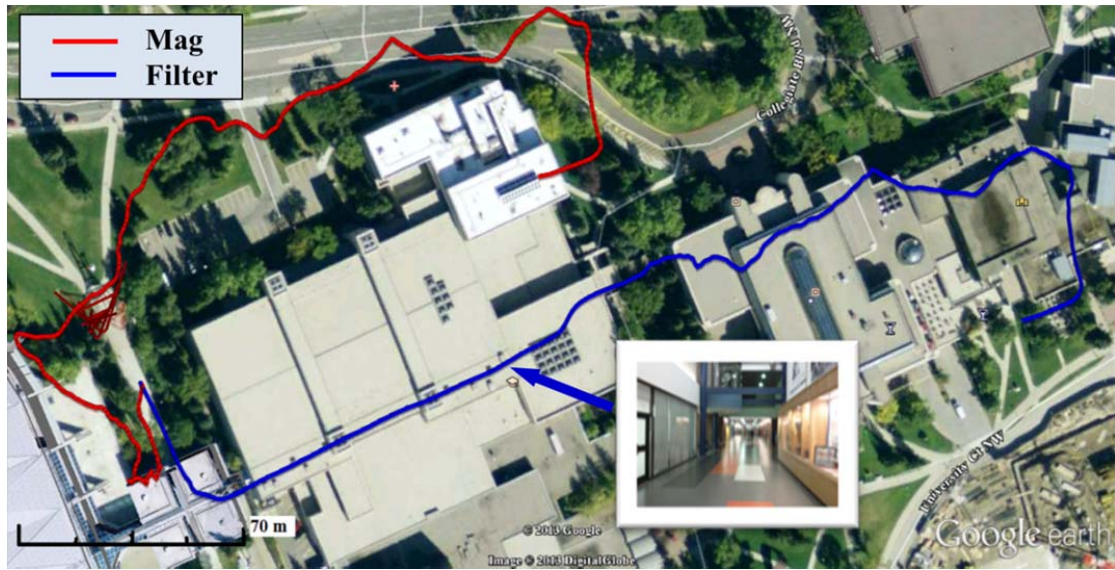
Figure 6.14: PDR solution using filter and magnetometer based heading on Google map

To evaluate the overall accuracy of the PDR algorithm, the reference trajectory was plotted on the map of the test site. The reference trajectory for the actual direction of the test is plotted on the map of the first floor of the University of Calgary. As shown in Figure 6.15, the maximum error is less than 5 m during the test. Furthermore, the trajectory ended at the correct point with a position drift of less than 4 m. The error in the distance was approximately 1.1 % of the total distance travelled.

161

Figure 6.15: PDR trajectory compared to a reference trajectory

6.4.3 Parking lot Test

Parking lots are often places of that produce the most confusion and disorientation for many users parking their cars, or locating their parked car. The large number of vehicles found in a shopping mall parking lot can be considered an obstacle for the magnetometer performance. To perform the test, the parking lot of Alastair Ross Technology Centre (ARTC) building is selected. As the location had clear sky, the GPS solution was used as reference.

The main challenge for this test is the presence of a large number of cars where the test was conducted. The presence of cars near the user can affect the performance of the magnetometer. Consequently, the magnetometer based heading was diverted and lead to error in the position during the west side of the trajectory. Figure 6.16 shows the magnetometer heading during a perturbation area where the user was moving beside cars.
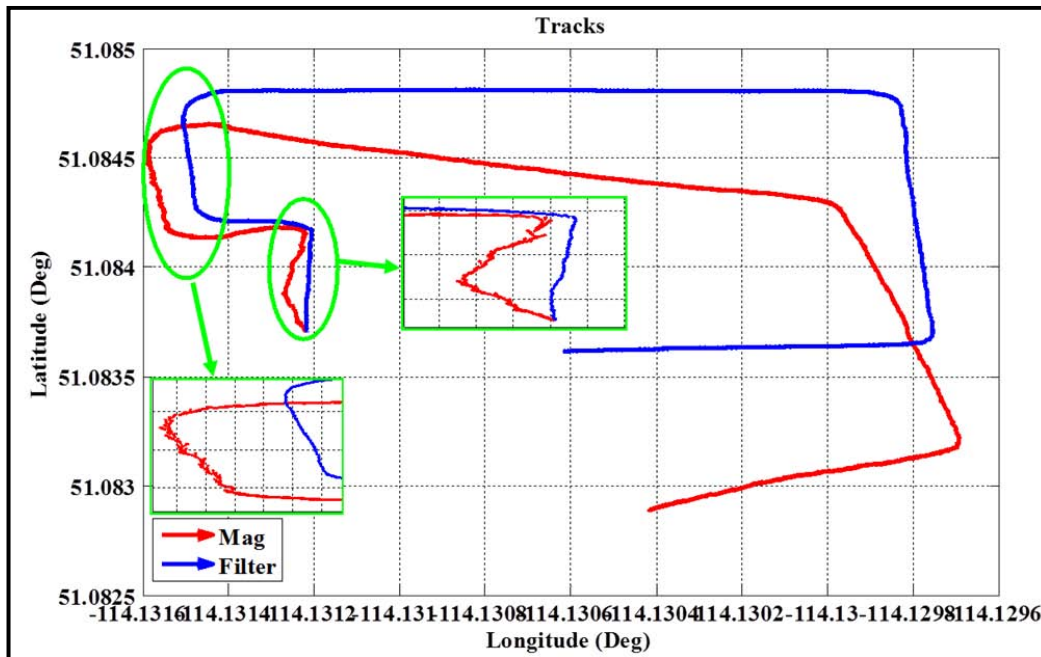
Figure 6.16: Magnetometer heading direction during perturbation area

In Figure 6.17 the PDR solution is compared to the GPS solution on a Google map. It is clear that the PDR trajectory follows the correct direction of the GPS reference solution. The magnetometer anomaly detection technique sets the perturbation flag ON when the user is moving through a perturbation area. This flag prevents the orientation filter from updating the solution and keeps propagating the solution based on gyroscope data. In this test, there is a good opportunity for magnetometer performance improving as the test is conducted in an open area. The error of the PDR solution during the test did not exceed 2 m with respect to the reference trajectory from GPS as shown in Figure 6.17. However, the GPS solution was affected when the user moved near the building. The results conclude that the overall performance of the PDR algorithm can be improved in case the magnetometer is performing well.
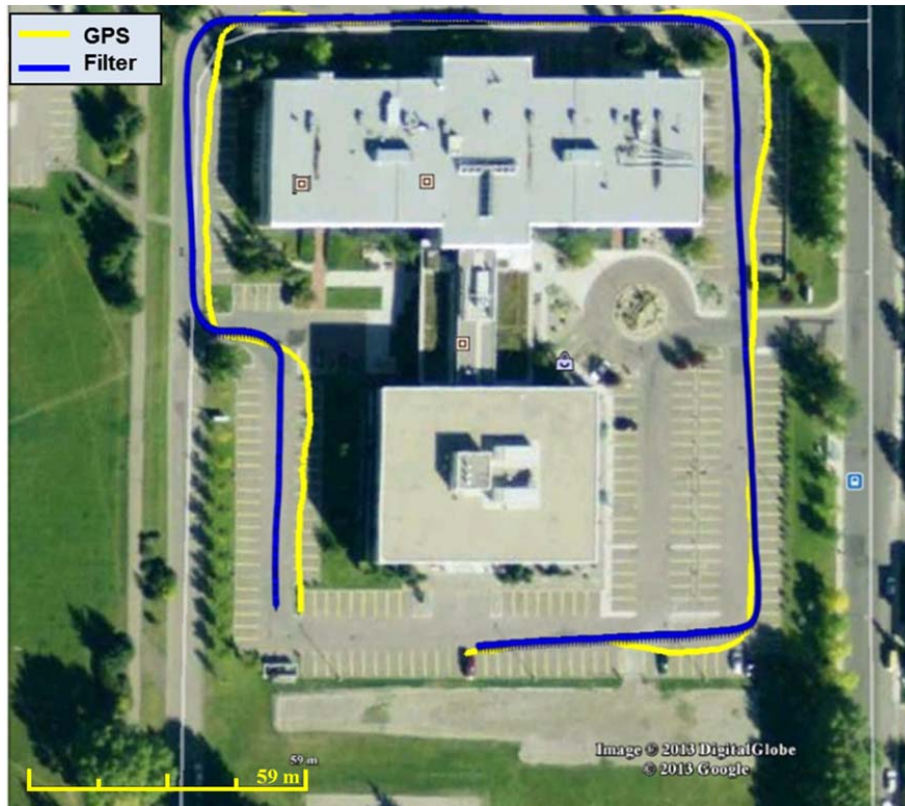
Figure 6.17: PDR solution using filter and magnetometer based heading plotted on Google map

6.4.4 Downtown Test

Downtown is attractive place for tourists in addition to many Calgarians. It has several major attraction sites such as shopping centers, business offices, museums, restaurants, cafes, and theaters. So, it is important to have a navigation system that is able to help pedestrians find their destinations in a heavily congested environment. This test was conducted in downtown Calgary to assess the performance of the proposed algorithm in GPS-denied or signal outage environments. The performance of the magnetometer was totally affected by the distortion of the

magnetic field in the downtown area. The high buildings, cars, and traffic signals added significantly more complications for the heading estimation based on the magnetometer.

The test is started at the intersection of the 7th street and 8th Avenue SW in the downtown quadrant of Calgary (Figure 6.18.) The selected trajectory was a square starting at an East direction followed by North, West, and South directions. The length of the trajectory due 490 m requiring about 6 minutes of walking.

Figure 6.18: Test starting point

Although the magnetometer had good manoeuvring at the start of the test, the presence of a strong perturbation source affected the heading estimation. As shown in Figure 6.19, the estimated heading from the magnetometer is not useful for the majority of the test due to the

distortion in the magnetic field. It shows that the heading update is available for only two minutes during the interval of 140 s to 260 s.
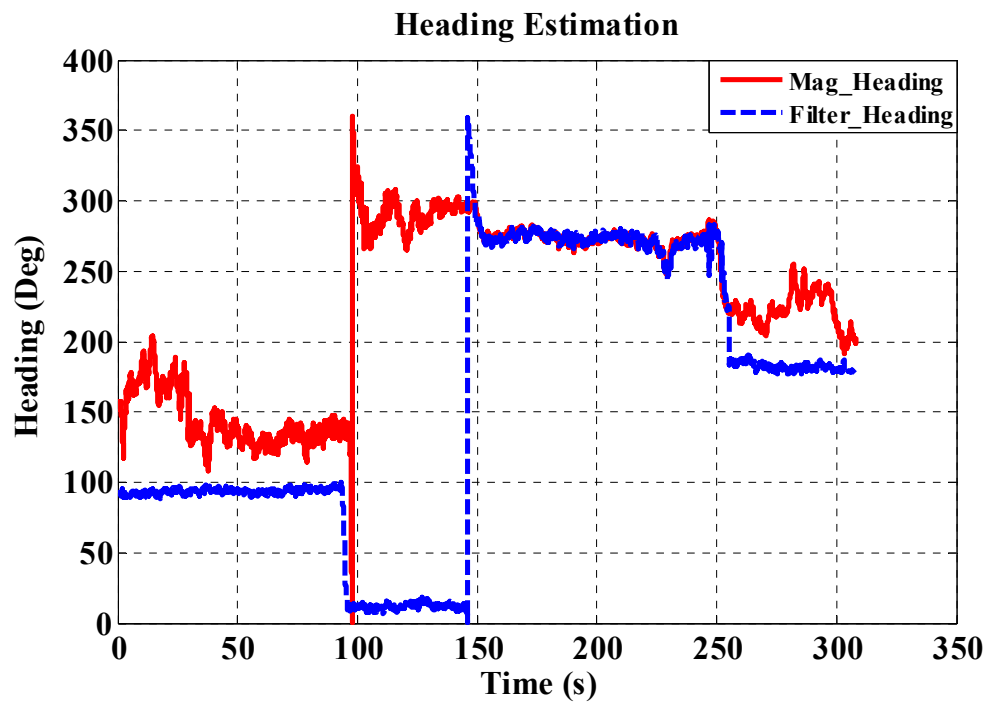
Figure 6.19: Heading estimation

Figure 6.20 shows the PDR solution using the orientation filter compared to the same solution based on the heading from the magnetometer stand-alone, gyroscope heading stand-alone, and GPS solution. As shown in the figure, there is no accurate stand-alone solution for the test trajectory.

- The gyroscope stand-alone solution provides accurate direction but its derived position drifted because of the gyroscope's uncompensated bias.

- The magnetometer stand-alone solution is diverted in many parts of the test. However, in certain parts it did perform well and provided the correct heading.

166

- The GPS technique is considered the poorest solution as it failed to provide any correct information at all during the test due to the satellite's unavailability.

The PDR algorithm based on the orientation filter, in cooperation with the magnetometer anomaly detection technique, provides an acceptable solution.
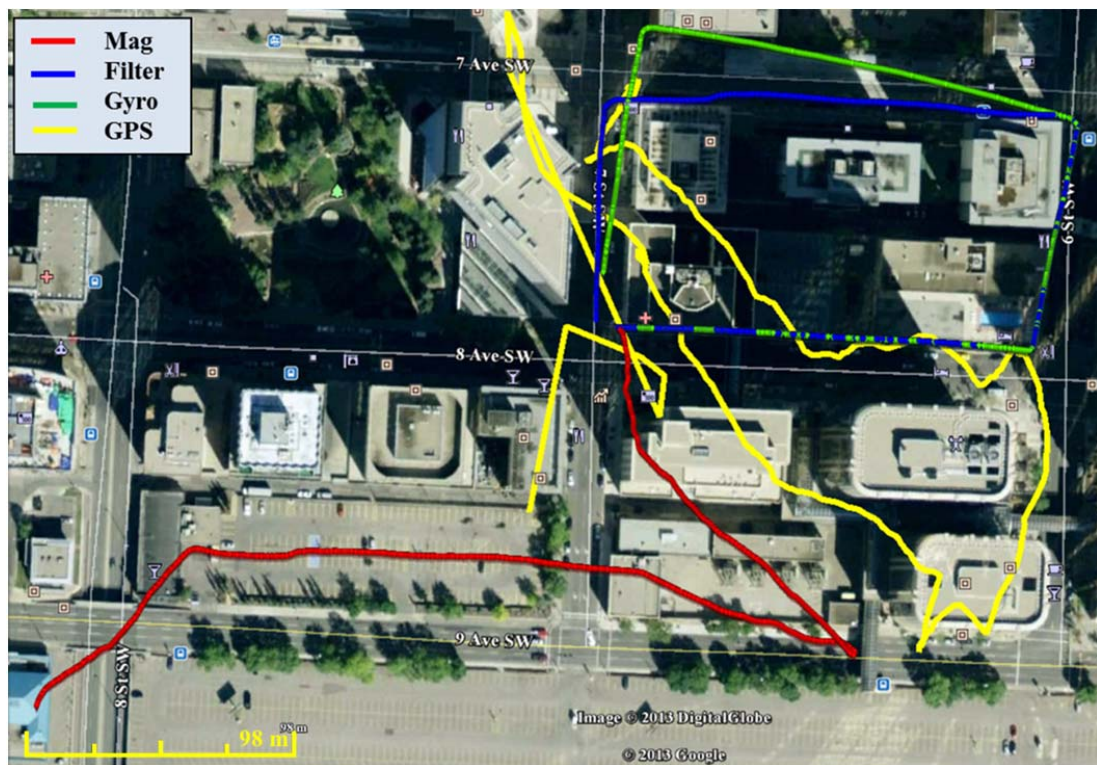
Figure 6.20: PDR solution using filter, magnetometer, and gyroscope based heading compared to GPS solution plotted on Google map

The overall accuracy of the PDR algorithm is evaluated by comparing the PDR solution with a reference trajectory on a Google map. As shown in Figure 6.21, the maximum error in position occurs at the North side of the trajectory where no update was yet available, which lasted for approximately 10 m. Despite these errors, the trajectory ends at the correct place with position drift of less than 7 m. The overall error in distance is about 2 % of the total travelled distance.
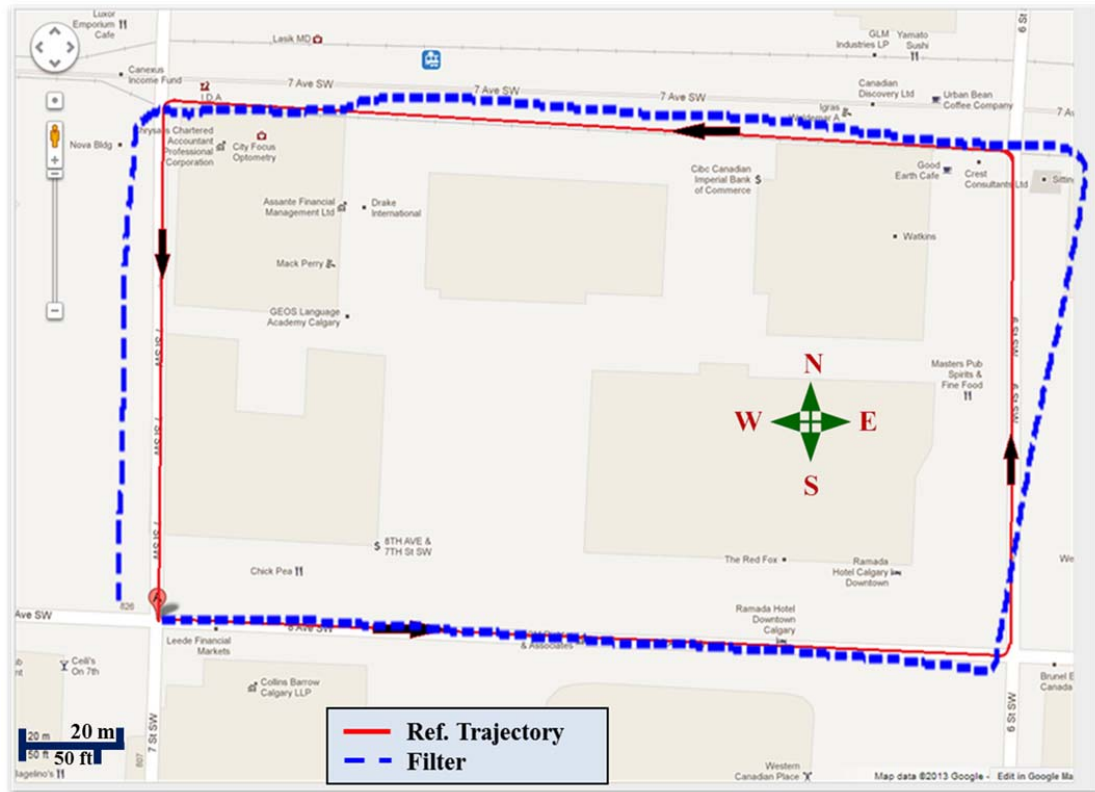
Figure 6.21: PDR trajectory compared to a reference trajectory

6.4.5 Switching Mode Test

This test was conducted to verify the proposed algorithm in a situation where the device mode (orientation) is changed during the navigation process. The mode changes mean that the orientation of the device is changed from one orientation to another such as from texting to ear talking or belt tethering. In these scenarios, the roll and pitch angles are changed. Two main problems were raised in this case: sudden change in the device orientation leading to problems in the estimated heading and misalignment where the device was not aligned with the user's direction. An outdoor environment is selected due to the presence of a reference solution from

168

GPS. Figure 6.22 shows the original raw measurements form the sensors. It is observed that the gravity, and vertical axis is changed according to the device orientation.
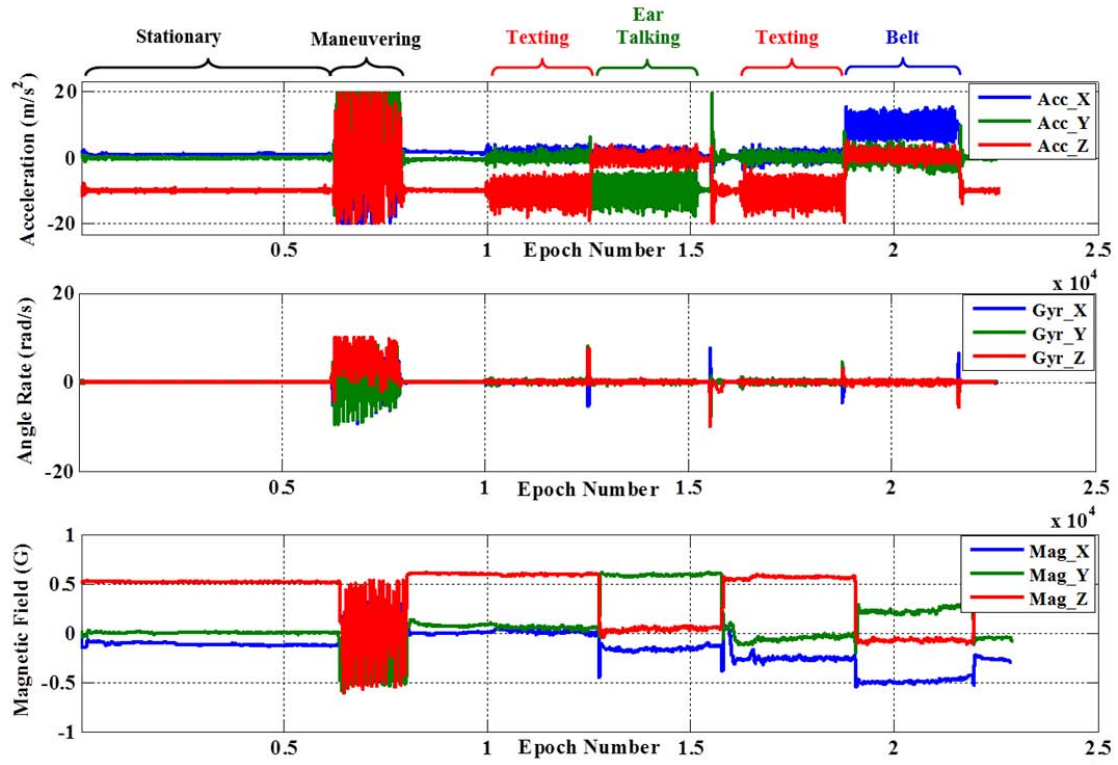
Figure 6.22: Sensors' raw measurements

A new finding to emerge in the results is that slow walking turns are hardly picked up by the gyroscope, while they are picked up by the magnetometer. During the test, there were four different consecutive intervals with three mode changes:

- Texting to ear talking.

- Ear talking to texting.

- Texting to belt.

The raw measurements are transformed, as described in Chapter 5, to the correct frame matching the navigation frame definition. Consequently, the sensor frame axes are flipped to compensate

for the expected misalignment in each orientation. Figure 6.23 shows the vertical axis after it has been transformed to be the z axis for all orientations.
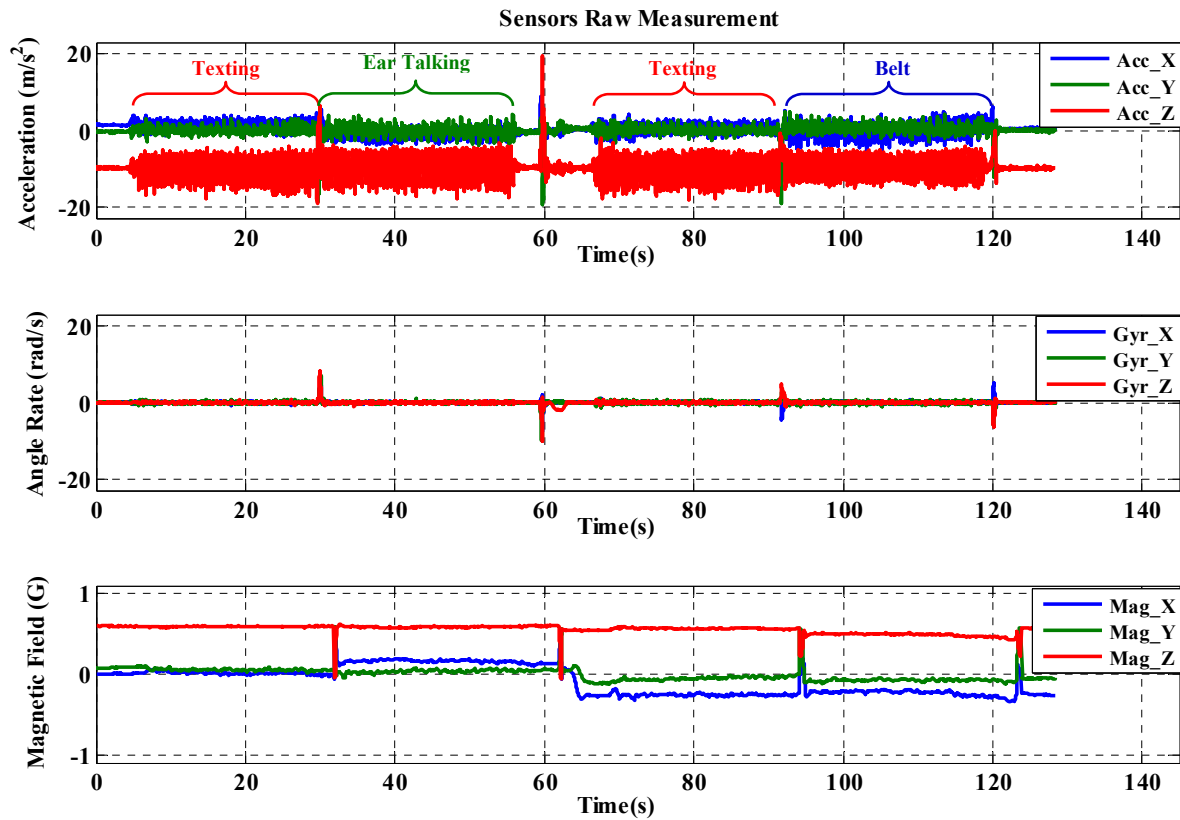
Figure 6.23: Sensors' transformed data

The transformation is executed using two steps; the levelling step and the misalignment correction step. A window of one second of sensor data is verified to detect the vertical axis in order to identify the device orientation. A combination of roll angle, pitch angle, and the gravity axis values is used to determine the device orientation.

As shown in Figure 6.24, the values of the roll and pitch are changed according to the device orientation. For example, during the ear talking orientation, the roll angle values are -90° while the pitch angle values are 90° during the belt orientation.

Device Roll
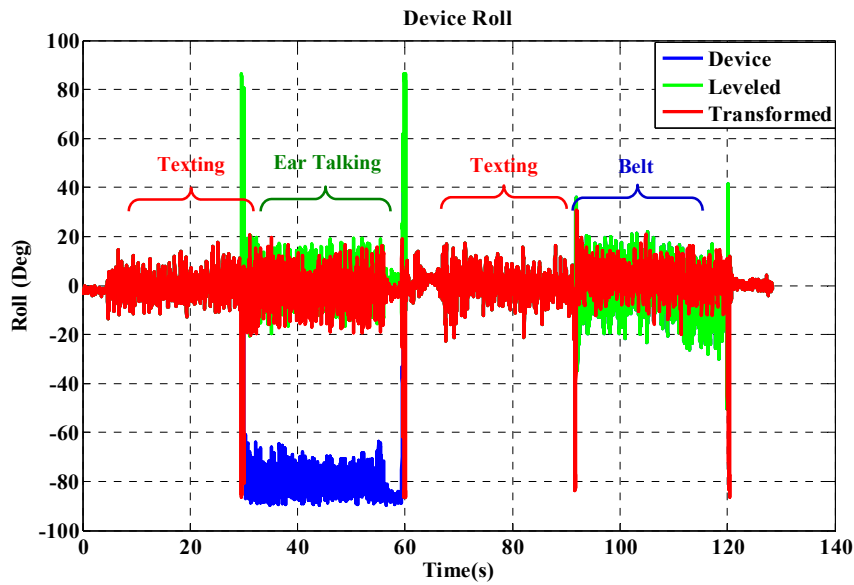
(a) Roll angle
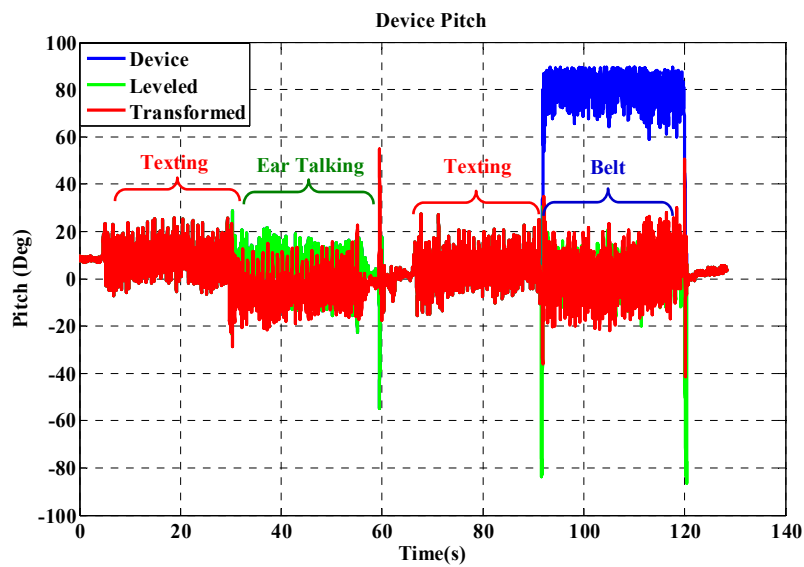
Device Pitch

(b) Pitch angle

Figure 6.24: The device orientation

171

There is no misalignment between the user and device if the device is held in the texting mode during the test. However, a misalignment angle is created between the user and the device if the device orientation is changed. Figure 6.25 presents the estimated values for the heading of the device compared to the heading of the user. It is clear that there is a difference between the user heading and the device heading due to the misalignment. For example, at the beginning the user is heading north holding the device in the same direction with zero heading expected for both user and device. During ear talking, the user is still heading north but the device orientation is changed to be in the forward axis heading south. In this scenario, the expected heading for the user is zero while the device heading is 180°. The situation required a compensation of 180° to provide the user's correct direction.
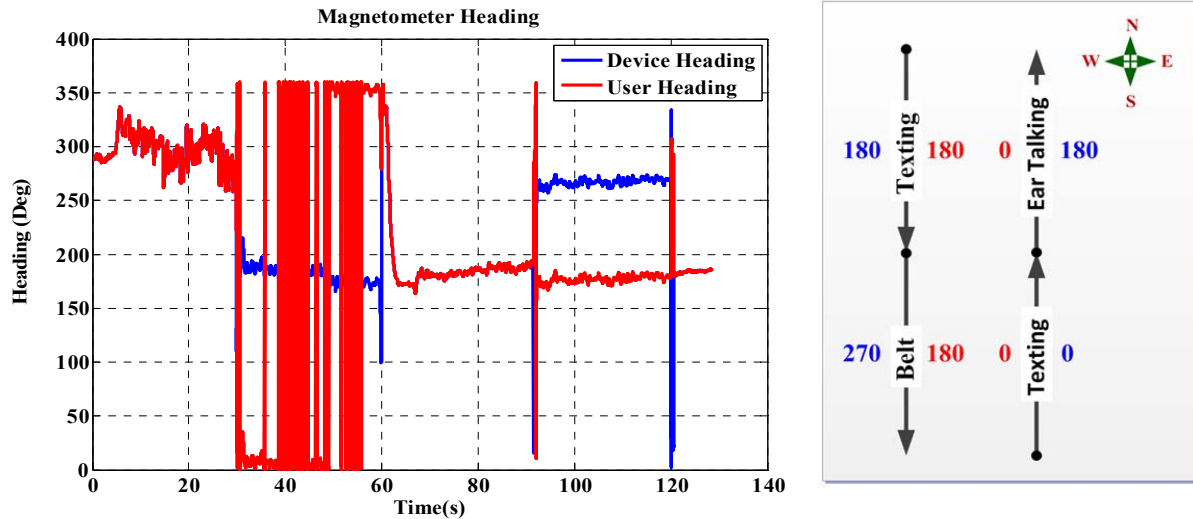
Figure 6.25: The device and user estimated heading

Figure 6.26 shows the user heading compared to the magnetometer heading. As previously, if the magnetometer is used in stand-alone mode then the results are not reliable, and a gyroscope

172

alone is insufficient. Therefore, the orientation filter is updated along with the magnetometer heading to assist in seamless navigation. It many areas, the filter heading in the figure does not match the magnetometer heading. The orientation filter update process is done only when a step stance occurs, so at the beginning and at the end of the test there are no detected steps as the user is stationary. The plotted heading from the orientation filter only represents the values when the step occurs, while the magnetometer heading is plotted for the whole duration of the test.
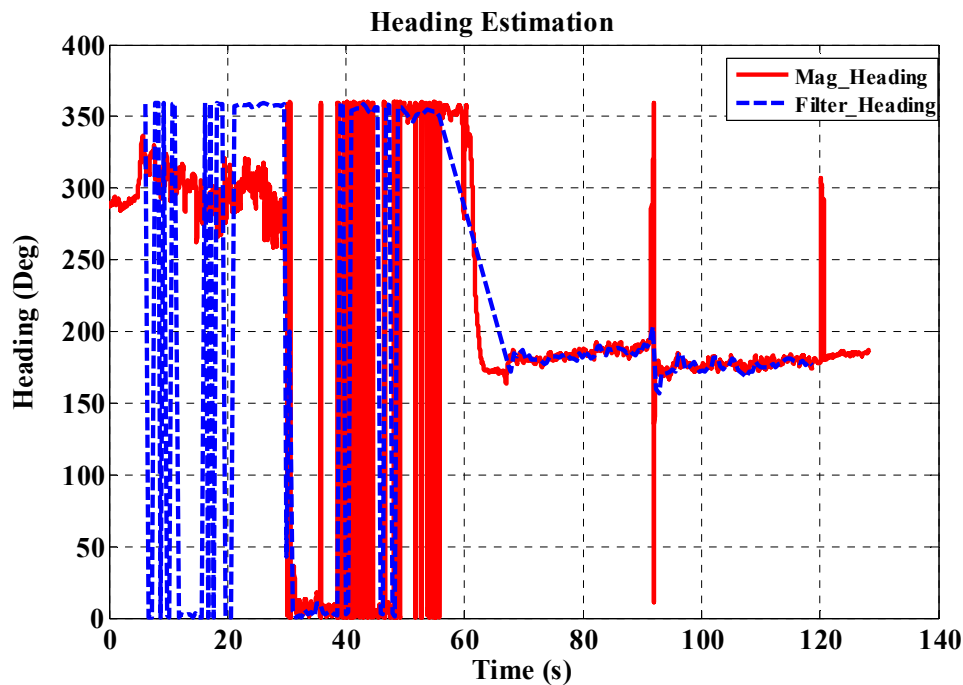
Figure 6.26: The estimated heading

Figure 6.27 shows the magnetometer heading during a transition interval from one orientation to another. The figure shows that the heading is diverted due to the sudden change in the device orientation. This confirms the importance and the need for using different sources of navigation information to match the requirements of seamless navigation.

173
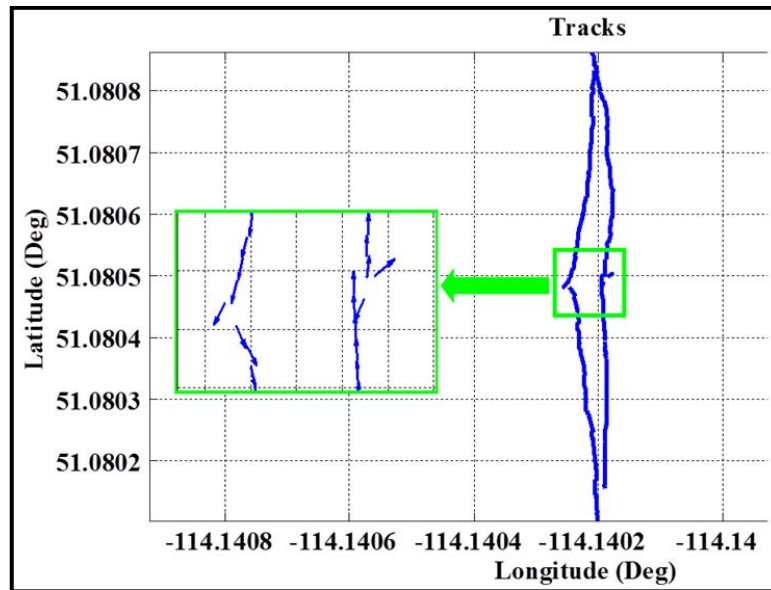
Figure 6.27: Magnetometer heading direction during perturbation area

The result of the detection step is shown in Figure 6.28. The figure shows that the algorithm is able to detect the user steps regardless the device orientation.
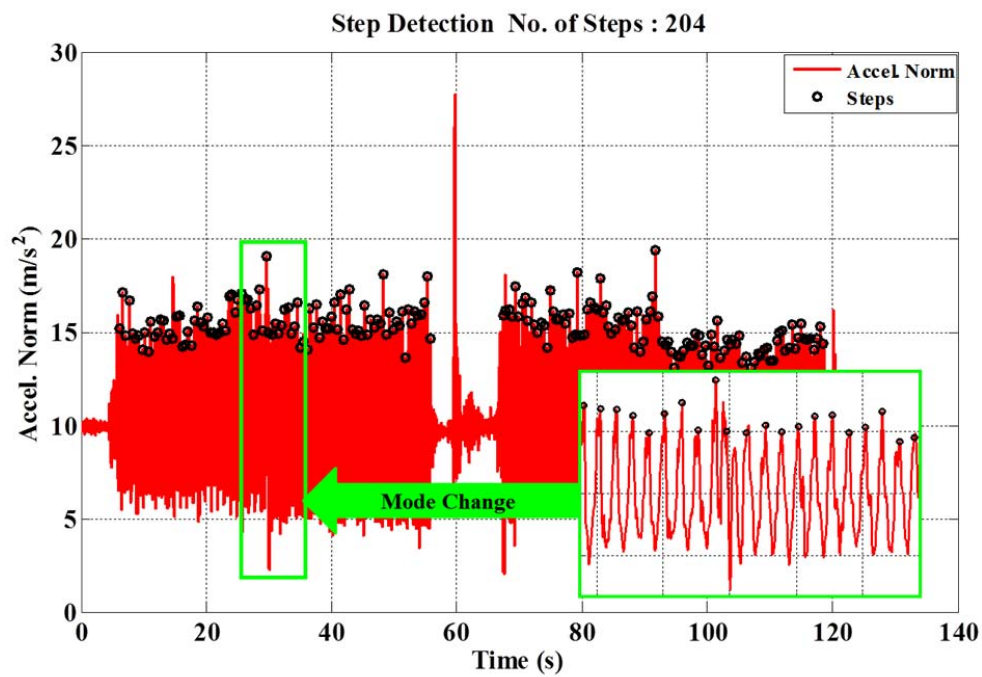
Figure 6.28: Step detection

174

In Figure 6.29, PDR solution is compared with GPS for the switching mode scenario. The resulted PDR solution produces a position error in the range of 2 m compared to the GPS trajectory. It is also observed that the solution is diverted somehow after the transition period due to unstable sensors' measurements.
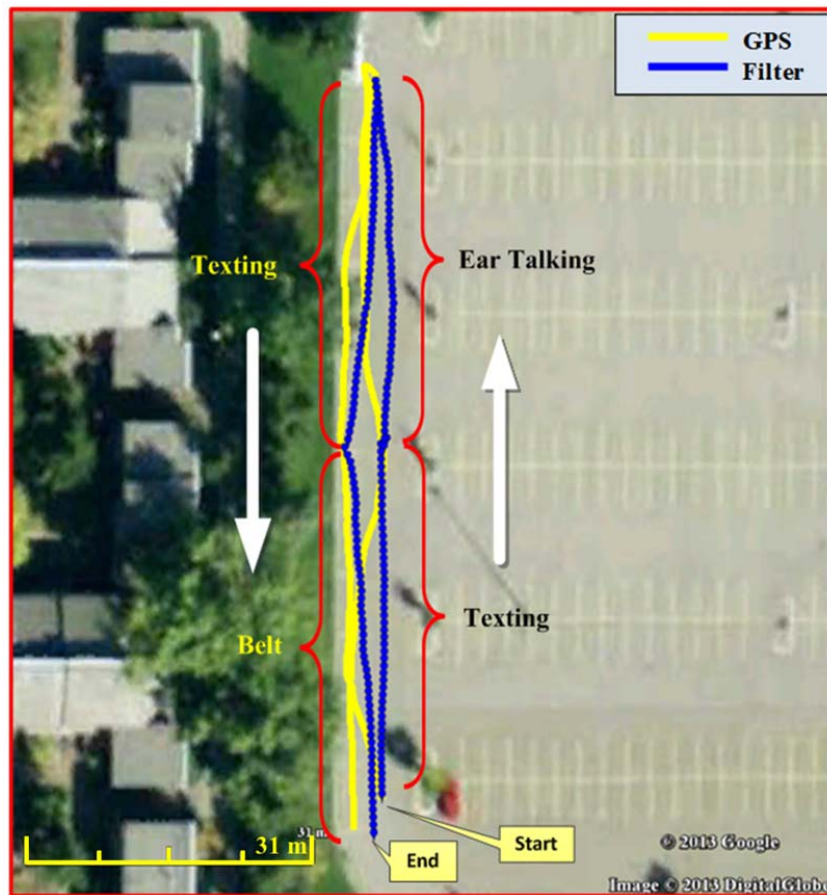
Figure 6.29: PDR solution compared to GPS solution plotted on Google map

175

Chapter Seven: Conclusion and Recommendations

In this thesis, the use of the low cost sensors in the pedestrian navigation is investigated. The proposed work targeted the embedded sensors in different portable devices such as smartphones, tablets, and any other handheld devices. Step detection, step length estimation, and device attitude errors strongly affect the performance of the PDR algorithm. As a result, the proposed research focuses on improving the performance of the PDR in both normal and manoeuvring environments. This chapter summarizes the main contributions of the proposed work and provides. Lastly, recommendations are made for future work based on this research that will help develop of a seamless pedestrian navigation system.

7.1 Thesis Conclusions and Contributions

The main focus of this research work is on pedestrian navigation in GPS-denied areas. The overall objective of this thesis was to develop and test algorithms for pedestrian navigation with enhanced step detection, step length estimation, and heading estimation techniques. A special focus on the device attitude was undertaken for improving the efficiency of the PDR algorithm. The overall conclusion of the thesis is listed below:

1. Different tests were conducted using Samsung Galaxy Nexus smartphone as an example of current mobile devices in use by pedestrians. The device is suitable for personal use since it is lightweight and small. Furthermore, since this device has an open source operating system (Android), it is easier than ever to develop applications. The major advantage of these devices is that most of them are embedded with the necessary sensors for the navigation

process. However, these sensors are consumer (MEMS) grade, which mean that it is very low cost and inaccurate. This calls for the investigation of the possible ways to improve the performance of the different sensors. This requires a detailed analysis for the different terms of error to be handled.

2. As discussed in the literature, the magnetometer performance is determined to be totally subject to the quality of the measured magnetic field, which can be affected by any ferromagnetic materials in the vicinity. Different methods and techniques are investigated to improve the performance of the magnetometer in harsh environments to achieve the best accuracy of the sensed magnetic field:

   ### I. Magnetometer Calibration

   ➢ A robust magnetometer calibration method is implemented based on the PSO technique to estimate the bias and scale factor values. The proposed technique is found to have many advantages over other conventional methods where it does not require any error modeling or awareness of the nonlinearity.

   ➢ RIST technique is proposed to reduce the required number of samples for the calibration algorithm by using a window of the measurement. This reduces the processing time to 40% compared to using the entire dataset.

   ➢ The PSO technique, as described in Chapter 3, is an iterative process and occasionally requires longer times to converge for the bias and scale factor values. Thus, MPSOT is implemented to decrease the overall processing time to 35% of the consumed time by the basic PSO.

- The fusion of the RIST and MPSOT techniques with the basic PSO algorithm decreased the required time for the calibration process. This extends the opportunity to apply the proposed algorithm in real-time applications.

- Additionally, the proposed calibration technique is implemented in the magnetic field domain rather than the heading domain. This makes it applicable for different applications that include the magnetometer in their operations, not only navigation applications.

II. *Different Manoeuvring Modes:*

- Three different manoeuvring modes, coordinated, 3D Figure-Eight, and random, are investigated to assess the impact of each on the magnetometer calibration process. Among the three manoeuvring modes, the coordinated mode is found to be the most effective one in terms of residual error distribution, the constancy of the estimated magnetic field, and error mean and standard deviation ranges. Thus, it is recommended to move the navigation device around the different axes to cover a wide range of the expected movements of the pedestrian as in the coordinated manoeuvring mode.

III. *Magnetometer Anomaly Detection:*

- Characterizing the magnetic field perturbations through various pedestrian navigation environments was determined to be effective at providing detailed insight into the strength, occurrence as well as the distribution of perturbations. Thus, investigation and recommendation for perturbation detection technique is found necessary as the quality of the used magnetometer is not high.

➢ A perturbation detection scheme is developed utilizing the different magnetic field parameters to avoid using incorrect magnetometer based heading information.

➢ In addition, the anomaly detection technique is found to be important to request a recalibration process in case the user moves from outdoors to indoors as the magnetic field is candidate to have different distribution or in case the change in the magnetic field due to an external factor is very high for long time.

3. For future generations of Smartphones and other handheld devices, this investigation adds to the pre-existing knowledge of calibration, and to reap maximum benefit from low cost magnetometers. In this thesis, gyroscope is used as main source for attitude information where accelerometer provides the roll and pitch update and magnetometer is used for heading update.

- A KF-based fusion technique is used to estimate the device attitude and gyroscope bias as well as combine these with the magnetic field perturbation detection technique. The Proposed technique exploits two different attitude sensors, gyroscope and magnetometer, as a complementary fusion scheme.

- Due to the noisy data of accelerometers and magnetometers, both data are averaging over the update interval meaning a one-step occurrence. The proposed technique improves the accuracy of the device attitude estimation leading to improved PDR results where it can bridge the GPS gaps.

- The limitation of magnetometer measurements caused a position error up to 3% in the downtown area and 5% indoors of the total traveled distance. This suggests that the accuracy of the PDR algorithm that uses a magnetometer is unexpected when subjected to certain environmental conditions.

4. Step detection, step length estimation, and false step mitigation techniques are implemented to estimate the total travelled distance. The proposed schemes achieved an accuracy of about 97% for step detection and 95% for the step length estimation.

5. Different areas for field tests are selected, namely downtown and parking lot areas, to provide a perturbed magnetic field outdoor environment. The Kinesiology Complex and lecture theaters building offered a perturbed magnetic field indoor environment. The selection of such environments for assessing the proposed PDR offered a true example of the sensors' data for detailed and realistic investigation for the technique.

6. The investigation into the device mode leads to the derivation of a correct heading for the user during the change between the different modes of usage.

7.2 Recommendations and Future Work

Improving the performance of the PDR requires not only better modeling of the different error sources but also more benefits from different forms of navigation information. Such changes and additions would improve the overall performance and accuracy of a PDR device. Several recommendations for ongoing future work are listed below:

- For better results from the calibration process, it is recommended that the device be moved in the entire 3D space to obtain maximum change in all directions.

- The magnetic field is sensitive to the surrounding environment contents and structure. In order to achieve better performance from the geomagnetic field sensor, it is recommended to perform the magnetometer calibration at each change in the environment, such as switching from outdoor to indoor.

- The perturbation detection technique can be improved by utilizing a Knowledge Based System (KBS). The system can incorporate the available information for the different magnetic field components which improve the algorithm's robustness.

- Use of all possible CUPT techniques to update the position of the user. This can be achieved using GPS when available or landmarks (RFID tags). The tags should be installed at noticeable points for the pedestrian. For example, they could be set at the entrance of buildings, main doors, stairs, or elevators. Also, Wi-Fi access points can be used for position updates in indoor environments once the infrastructure allows for that. In addition, A ZUPT technique can be used for updating the attitude filter during a stationary interval of the user when entering elevators or opening a door.

- Modeling the 3D positioning instead of 2D positioning can improve the accuracy of the PDR algorithm. This leads to accurate estimates for the traveled distance in cases where stairs are encountered. Moreover, the use of additional sensors, such as a barometer, is recommended to increase the ability to detect the floor change.

- A significant amount of research is required to the device more user friendly and convenient. Since the pedestrian is expected to carry or hold the device in different orientations, the misalignment angle must be estimated to obtain an accurate heading.

- The proposed PDR algorithm deals only with a normal walking case. However, different user activities must be further investigated such as running, jogging, or slow walking.

- The performance of the PDR algorithm can be improved by including the GPS solution wherever is available as the proposed technique is fully built for completely GPS-denied environments.

References

Afzal, M. H. (2011). Use of Earth's Magnetic Field for Pedestrian Navigation, Ph. D. Thesis, University of Calgary, Calgary, AB, Canada.

Ali, A. S., S. Siddharth, Z. Syed and N. El-Sheimy (2012a). An Improved Personal Dead-Reckoning Algorithm for Dynamically Changing Smartphone User Modes. Proceedings of the 25rd International Technical Meeting of The Satellite Division of the Institute of Navigation (ION GNSS 2012). Nashville, TN, USA.

Ali, A. S., S. Siddharth, Z. Syed and N. El-Sheimy (2012b). "Swarm Optimization-Based Magnetometer Calibration for Personal Handheld Devices." Sensors **12**(9): 12455-12472.

Ali, A. S., S. Siddharth, Z. Syed, C. L. Goodall and N. El-Sheimy (2013). "An efficient and robust maneuvering mode to calibrate low cost magnetometer for improved heading estimation for pedestrian navigation." Journal of Applied Geodesy **7**(1): 65–73.

Ali, A. S., S. Siddharth, Z. F. Syed and N. El-Sheimy (2011). "Particle Swarm Optimization Algorithm Based Low Cost Magnetometer Calibration." Archives of Photogrammetry, Cartography and Remote Sensing edited by Polish Society for Photogrammetry and Remote Sensing **22**: 9-23.

Alonso, R. and M. D. Shuster (2002). "TWOSTEP: a fast robust algorithm for attitude-independent magnetometer-bias determination." Journal of Astronautical Sciences **50**(4): 433-451.

Alonso, R. and M. D. Shuster (2003). "Complete linear attitude-independent magnetometer calibration." Journal of the Astronautical Sciences **50**(4): 477-490.

Altmann, S. L. (1986). Rotations, quaternions, and double groups, Clarendon, Oxford.

Aparicio, C. (2004). Implementation of a quaternion-based Kalman filter for human body motion tracking using MARG sensors, Monterey, California Naval Postgraduate School.

Bachmann, E. R., X. Yun and C. W. Peterson (2004). An investigation of the effects of magnetic variations on inertial/magnetic orientation sensors. Robotics and Automation, 2004. Proceedings. ICRA'04. 2004 IEEE International Conference on, IEEE. **2:** 1115-1122.

Bageshwar, V. L. (2008). Quantifying performance limitations of Kalman filters in state vector estimation problems, ProQuest.

Bai, Q. (2010). "Analysis of particle swarm optimization algorithm." Journal of Computer and Information Science **3**(1): 180-184.

Barbour, N. M. (2004). "Inertial navigation sensors." NATO RTO Lecture Series **232**(5): 5.2.

Beauregard, S. (2007). Omnidirectional pedestrian navigation for first responders. Positioning, Navigation and Communication, 2007. WPNC'07. 4th Workshop on, IEEE**:** 33-36.

Bekir, E. (2007). Introduction to modern navigation systems, World Scientific.

Blodget, H., P. Gobry and A. Cocotas. (2012). "The Future of Mobile." Business Insider, http://www.businessinsider.com/the-future-of-mobile-deck-2012-3.

Blum, C. and X. Li (2008). "Swarm intelligence in optimization." Swarm Intelligence: 43-85.

Boulic, R., N. M. Thalmann and D. Thalmann (1990). "A global human walking model with real-time kinematic personification." The visual computer **6**(6): 344-358.

Brown, R. G. and P. Y. Hwang (1992). Introduction to random signals and applied Kalman filtering, Wiley New York.

Caruso, M. J. (1997). "Applications of magnetoresistive sensors in navigation systems." SAE transactions **106**: 1092-1098.

Chen, B. (1996). Efficient communication over additive white Gaussian noise and intersymbol interference channels using chaotic sequences, Massachusetts Institute of Technology, Dept. of Electrical Engineering and Computer Science.

Cho, S. Y., K. W. Lee, C. G. Park and J. G. Lee (2003). A personal navigation system using low-cost MEMS/GPS/Fluxgate. Proceedings of the 59th Annual Meeting of The Institute of Navigation and CIGTF 22nd Guidance Test Symposium, Albuquerque, NM.

Cooke, J. M., M. J. Zyda, D. R. Pratt and R. B. McGhee (1992). NPSNET: Flight simulation dynamic modeling using quaternions, Naval Postgraduate School.

Crassidis, J. L., K. L. Lai and R. R. Harman (2005). "Real-time attitude-independent three-axis magnetometer calibration." Journal of Guidance Control and Dynamics **28**(1): 115-120.

Crocker, E. and L. Rabins (1970). Applications of Kalman Filtering Techniques to strap-down system Initial Alignment. . Theory and applications on Kalman Filters, Dr. Nebot, E. M. by Leondes, C.T., DTIC Document.

De Agostino, M., A. M. Manzino and M. Piras (2010). Performances comparison of different MEMS-based IMUs. Position Location and Navigation Symposium (PLANS), 2010 IEEE/ION, IEEE**:** 187-201.

Dian, P. R., M. S. Siti and S. Y. Siti (2011). "Particle Swarm Optimization: Technique, System and Challenges." International Journal of Computer Applications **14**(1): 19-27.

Dorveaux, E., D. Vissière, A. P. Martin and N. Petit (2009). Iterative calibration method for inertial and magnetic sensors. Decision and Control, 2009 held jointly with the 2009 28th Chinese Control Conference. CDC/CCC 2009. Proceedings of the 48th IEEE Conference on, IEEE**:** 8296-8303.

El-Sheimy, N. (1996). "A mobile multi-sensor system for GIS applications in urban centers." International Archives of Photogrammetry and Remote Sensing **31**: 95-100.

El-Sheimy, N. (2012). "Inertial techniques and INS/DGPS Integration." Lecture Notes ENGO 623. Department of Geomatics Engineering, the University of Calgary, Canada.

El-Sheimy, N., H. Hou and X. Niu (2008). "Analysis and modeling of inertial sensors using allan variance." Instrumentation and Measurement, IEEE Transactions on **57**(1): 140-149.

Elbeltagi, E., T. Hegazy and D. Grierson (2005). "Comparison among five evolutionary-based optimization algorithms." Advanced engineering informatics **19**(1): 43-53.

Elkaim, G. H. and C. C. Foster (2006). Development of the metasensor: A low-cost attitude heading reference system for use in autonomous vehicles. Proceedings of the ION Global Navigation Satellite Systems Conference, Fort Worth, TX, USA.

Emura, S. and S. Tachi (1994). Compensation of time lag between actual and virtual spaces by multi-sensor integration. Multisensor Fusion and Integration for Intelligent Systems, 1994. IEEE International Conference on MFI'94., IEEE**:** 463-469.

Faulkner, W. T., R. Alwood, D. W. A. Taylor and J. Bohlin (2010). GPS-denied pedestrian tracking in indoor environments using an IMU and magnetic compass. Proceedings of the 2010 International Technical Meeting of the Institute of Navigation (ION-ITM 2010)**:** 198-204.

Feliz Alonso, R., E. Zalama Casanova and J. Gómez García-Bermejo (2009). "Pedestrian tracking using inertial sensors." Journal of Physical Agents **3**(1): 35 - 42.

Finlay, C. C., S. Maus, C. D. Beggan, T. N. Bondar, A. Chambodut, T. A. Chernova, A. Chulliat, V. P. Golovkov, B. Hamilton and M. Hamoudi (2010). "International geomagnetic

reference field: the eleventh generation." Geophysical Journal International **183**(3): 1216-1230.

Foster, C. C. and G. H. Elkaim (2008). "Extension of a Two-Step Calibration Methodology to Include Nonorthogonal Sensor Axes." Ieee Transactions on Aerospace and Electronic Systems **44**(3): 1070-1078.

Foxlin, E. (1996). Inertial head-tracker sensor fusion by a complementary separate-bias Kalman filter. Virtual Reality Annual International Symposium, 1996., Proceedings of the IEEE 1996, IEEE**:** 185-194, 267.

Foxlin, E. (2005). "Pedestrian tracking with shoe-mounted inertial sensors." Computer Graphics and Applications, IEEE **25**(6): 38-46.

Gädeke, T., J. Schmid, W. Stork and K. D. Müller-Glaser (2011). "Pedestrian Dead Reckoning for Person Localization in a Wireless Sensor Network." energy (a) **2**: 1.

Gebre-Egziabher, D., G. H. Elkaim, J. D. Powel and B. W. Parkinson (2006). "Calibration of strapdown magnetometers in magnetic field domain." Journal of Aerospace Engineering **19**(2): 87-102.

Gelb, A. (1974). Applied optimal estimation, MIT press.

Giardina, C., J. Heckathorn and D. Krasnjanski (1981). A comparative study of strapdown algorithms. (Institute of Navigation, National Aerospace Meeting, Warminster, Pa., Apr. 8-10, 1981.) Navigation, vol. 28, Summer 1981, p. 101-106. **28:** 101-106.

Godha, S. and G. Lachapelle (2008). "Foot mounted inertial system for pedestrian navigation." Measurement Science and Technology **19**(7): 075202.

Granziera Jr, F. (2006). Simulation and implementation of a real time attitude determinator using micro-manufactured sensors, Universidade Estadual de Londrina.

Grewal, M. S. and A. P. Andrews (2001). "Kalman Filter: Theory and Practice Using MATLAB." Wieley-Interscience, Canada.

Groves, P. D., G. W. Pulford, C. A. Littlefield, D. L. Nash and C. J. Mather (2007). Inertial navigation versus pedestrian dead reckoning: Optimizing the integration. Proc. ION GNSS**:** 2043-2055.

Grubin, C. (1970). "Derivation of Quaternion Scheme via Euler Axis and Angle,." J. Spacecr. Rockets, **7**(10).

Han, S. and J. Wang (2011). "A novel method to integrate IMU and magnetometers in attitude and heading reference systems." Journal of Navigation **64**(04): 727-738.

Havangi, R., M. A. Nekoui and M. Teshnehlab (2010). "A multi swarm particle filter for mobile robot localization." International Journal of Computer Science Issues **7**(3): 15-22.

Hernane, Y., S. Hernane and M. Benyettou (2010). "PFPSO: An Optimised Filtering Approach Based on Sampling." Journal of Applied Sciences **10**(6): 494-499.

Honeywell. (2009). "DRM™4000 Dead Reckoning Module."   Retrieved Sep. 2012, from http://www51.honeywell.com/aero/common/documents/myaerospacecatalog-documents/Missiles-Munitions/DRM4000.pdf.

Hou, H. and N. El-Sheimy (2003). Inertial sensors errors modeling using Allan variance. Proceedings of the 16th International Technical Meeting of the Satellite Division of The Institute of Navigation (ION GPS/GNSS 2003)**:** 2860-2867.

Jirawimut, R., P. Ptasinski, V. Garaj, F. Cecelja and W. Balachandran (2003). "A method for dead reckoning parameter correction in pedestrian navigation system." Instrumentation and Measurement, IEEE Transactions on **52**(1): 209-215.

184

Kaniewski, P. and J. Kazubek (2009). Design and Prototype of Heading Reference System. ENC-GNSS' 09. Naples, Italy.

Kennedy, J. and R. Eberhart (1995). Particle swarm optimization. Neural Networks, 1995. Proceedings., IEEE International Conference on, IEEE. **4:** 1942-1948.

Kennedy, J., R. C. Eberhart and Y. Shi (2001). Swarm intelligence, Morgan and Kauffman, San Francisco.

Kim, J. W., H. J. Jang, D.-H. Hwang and C. Park (2004). "A step, stride and heading determination for the pedestrian navigation system." Journal of Global Positioning Systems **3**(1-2): 273-279.

Kotanen, A., M. Hannikainen, H. Leppakoski and T. Hamalainen (2003). Positioning with IEEE 802.11 b wireless LAN. Personal, Indoor and Mobile Radio Communications, 2003. PIMRC 2003. 14th IEEE Proceedings on, IEEE. **3:** 2218-2222.

Koyuncu, H. and S. H. Yang (2010). "A survey of indoor positioning and object locating systems." IJCSNS International Journal of Computer Science and Network Security **10**(5): 121-128.

Kuipers, J. B. (1999). Quaternions and rotation sequences, Princeton university press Princeton, NJ, USA.

Kwakkel, S., G. Lachapelle and M. Cannon (2008). GNSS aided in situ human lower limb kinematics during running. Proc. of ION GNSS.

Lachapelle, G., H. Kuusniemi, D. T. Dao, G. MacGougan and M. Cannon (2004). "HSGPS signal analysis and performance under various indoor conditions." Navigation **51**(1): 29-43.

Ladetto, Q. (2000). On foot navigation: continuous step calibration using both complementary recursive prediction and adaptive Kalman filtering. Proceedings of ION GPS. **2000:** 1735-1740.

Ladetto, Q., V. Gabaglio and B. Merminod (2001). Combining gyroscopes, magnetic compass and GPS for pedestrian navigation. Proceedings of the international symposium on kinematic systems in geodesy, geomatics, and navigation**:** 205-213.

Ladetto, Q., J. Van Seeters, S. Sokolowski, Z. Sagan and B. Merminod (2002). Digital magnetic compass and gyroscope for dismounted soldier position and navigation. NATO-RTO Meeting: Military Capabilities enabled by Advances in Navigation Sensors, Istanbul, Turkey, NATO Research and Technology Agency, Sensors & Electronics Panel.

Lapucha, D., K. P. Schwarz, M. E. Cannon and H. Martell (1990). The use of INS/GPS in a highway survey system. Position Location and Navigation Symposium, 1990. Record. The 1990's-A Decade of Excellence in the Navigation Sciences. IEEE/PLANS'90., IEEE, IEEE**:** 413-420.

Lee, S.-W. and K. Mase (2001). Recognition of walking behaviors for pedestrian navigation. Control Applications, 2001.(CCA'01). Proceedings of the 2001 IEEE International Conference on, IEEE**:** 1152-1155.

Li, Q., M. Young, V. Naing and J. Donelan (2010). "Walking speed estimation using a shank-mounted inertial measurement unit." Journal of biomechanics **43**(8): 1640-1643.

Liang, J. J., A. K. Qin, P. N. Suganthan and S. Baskar (2006). "Comprehensive learning particle swarm optimizer for global optimization of multimodal functions." IEEE Transactions on Evolutionary Computation, **10**(3): 281-295.

Liu, Y. and K. M. Passino (2000). "Swarm intelligence: Literature overview." Department of Electrical Engineering, the Ohio State University.

Lötters, J., J. Schipper, P. Veltink, W. Olthuis and P. Bergveld (1998). "Procedure for in-use calibration of triaxial accelerometers in medical applications." Sensors and Actuators A: Physical **68**(1): 221-228.

Luinge, H. and P. Veltink (2005). "Measuring orientation of human body segments using miniature gyroscopes and accelerometers." Medical and Biological Engineering and Computing **43**(2): 273-282.

MacGougan, G., G. Lachapelle, R. Klukas, K. Siu, L. Garin, J. Shewfelt and G. Cox (2002). "Performance analysis of a stand-alone high-sensitivity receiver." GPS Solutions **6**(3): 179-195.

Mandea, M., H. Lühr, M. Korte, G. Balasis, H.-J. Linthe, K. Hemant, E. Pulz, P. Ritter, M. Rother, C. Stolle, E. Thébault and I. Wardinski (2006). A comprehensive view of the Earth's magnetic field from ground and space observations. Zweijahresbericht GeoForschungsZentrum Potsdam 2004/2005**:** 14.

Marins, J. L., X. Yun, E. R. Bachmann, R. B. McGhee and M. J. Zyda (2001). An extended Kalman filter for quaternion-based orientation estimation using MARG sensors. Intelligent Robots and Systems, 2001. Proceedings. 2001 IEEE/RSJ International Conference on, IEEE. **4:** 2003-2011.

May, A., T. Ross, S. Bayer and M. Tarkiainen (2003). "Pedestrian navigation aids: information requirements and design implications." Personal and Ubiquitous Computing **7**(6): 331-338.

Morrison, A., V. Renaudin, J. B. Bancroft and G. Lachapelle (2012). "Design and testing of a multi-sensor pedestrian location and navigation platform." Sensors **12**(3): 3720-3738.

Nebot, E. and H. Durrant-Whyte (1999). "Initial calibration and alignment of low-cost inertial navigation units for land vehicle applications." Journal of Robotic Systems **16**(2): 81-92.

Ojeda, L. and J. Borenstein (2007). Personal dead-reckoning system for gps-denied environments. Safety, Security and Rescue Robotics, 2007. SSRR 2007. IEEE International Workshop on, IEEE**:** 1-6.

Pan, H., L. Wang and B. Liu (2006). "Particle swarm optimization for function optimization in noisy environment." Applied Mathematics and Computation **181**(2): 908-919.

Parsopoulos, K. and M. Vrahatis (2001). "Particle swarm optimizer in noisy and continuously changing environments." methods **5**(6): 23.

Parsopoulos, K. E. and M. N. Vrahatis (2010). Particle swarm optimization and intelligence: advances and applications, Information Science Reference Hershey.

Pedersen, M. E. H. (2010). "Good parameters for particle swarm optimization." Hvass Lab., Copenhagen, Denmark, Tech. Rep. HL1001.

Rajini, A. and V. David (2010). "Constructing Models for Microarray Data with Swarm Algorithms." International Journal of Computer Science and Information Security **8**(9): 237-242.

Retscher, G. and A. Kealy (2005). Ubiquitous Positioning Technologies for Intelligent Navigation Systems. 2nd Workshop on Positioning, Navigation and Communication, University of Hannover, Germany**:** 99-108.

Rogers, R. M. (1996). Weapon IMU transfer alignment using aircraft position from actual flight tests. Position Location and Navigation Symposium, 1996., IEEE 1996, IEEE**:** 328-335.

Sabat, S. L., L. Ali and S. K. Udgata (2011). "Integrated learning particle swarm optimizer for global optimization." Applied Soft Computing **11**(1): 574-584.

Sabatini, A. M., C. Martelloni, S. Scapellato and F. Cavallo (2005). "Assessment of walking features from foot inertial sensing." Biomedical Engineering, IEEE Transactions on **52**(3): 486-494.

Sagawa, K., H. Inooka and Y. Satoh (2000). Non-restricted measurement of walking distance. Systems, Man, and Cybernetics, 2000 IEEE International Conference on, IEEE. **3:** 1847-1852.

Santana, T. A. S. (2009). Performance of algorithms for calibration of MEMS sensors applied to attitude determination. Electrical Engineering, Universidade Estadual de Londrina.

Savage, P. (2000). "Strapdown Analytics, volume 1. Strapdown Associates." Inc, Maple Plain, MA, USA.

Schiller, J., A. Voisard and F. I. Berlin (2004). "Information handling in mobile applications: A look beyond classical approaches." GeoSensor Networks: 88.

Schleppe, J. B. (1996). Development of a real-time attitude system using a quaternion parameterization and non-dedicated GPS receivers, M.Sc thesis, University of Calgary, Calgary, Canada.

Schwarz, K. P. and M. Wei (2000). "INS/GPS Integration for Geodetic Applications." Lecture Notes ENGO 623. Department of Geomatics Engineering, the University of Calgary, Canada.

Sedighizadeh, D. and E. Masehian (2009). "Particle swarm optimization: methods, taxonomy and applications." International Journal of Computer Theory and Engineering **1**(5): 1793-8201.

Setoodeh, P., A. Khayatian and E. Frajah (2004). "Attitude estimation by separate-bias Kalman filter-based data fusion." Journal of Navigation **57**(2): 261-273.

Shi, Y. and R. C. Eberhart (1998). Parameter selection in particle swarm optimization. Evolutionary Programming VII, Springer**:** 591-600.

Shin, E. H. (2005). "Estimation techniques for low-cost inertial navigation." UCGE report(20219).

Shuster, M. D. (1993). "A survey of attitude representations." Navigation **8**: 9.

Siddharth, S., A. S. Ali, N. El-Sheimy, C. L. Goodall and Z. F. Syed (2012). "A game-theoretic approach for calibration of low-cost magnetometers under noise uncertainty." Measurement Science and Technology **23**(2): 025003.

Siddharth, S., A. S. Ali, C. L. Goodall and N. El-Sheimy (2011). Investigating Aspects of Heading Estimation Error in Pedestrian Navigation. Proceedings of the 2011 International Technical Meeting of the Institute of Navigation**:** 635-642.

Stirling, R., J. Collin, K. Fyfe and G. Lachapelle (2003). An innovative shoe-mounted pedestrian navigation system. Proceedings of European Navigation Conference GNSS**:** 110-115.

Storms, W. and J. Raquet (2009). Magnetic Field Aided Vehicle Tracking. Proceedings of the 22nd International Technical Meeting of The Satellite Division of the Institute of Navigation (ION GNSS 2009)**:** 1767-1774.

Suh, Y. S. and S. Park (2009). Pedestrian inertial navigation with gait phase detection assisted zero velocity updating. Autonomous Robots and Agents, 2009. ICARA 2009. 4th International Conference on, IEEE**:** 336-341.

Syed, Z. (2009). Design and Implementation Issues of a Portable Navigation System, PHD Thesis.–Calgary, Canada: The University of Calgary, 2009.–230 p.

Takahashi, N. S., T. A. S. Santana, F. Granziera Jr and M. C. Tosin (2010). "accelerometer and magnetometer auto-calibration algorithm for attitude determination." Journal of Aerospace Engineering, Sciences and Applications **2** (3).

Tang, W., G. Howell and Y. H. Tsai (2005). "Barometric altimeter short-term accuracy analysis." Aerospace and Electronic Systems Magazine, IEEE **20**(12): 24-26.

TelecomCircle. (2009). "Introduction to Location Based Services (LBS)."   Retrieved February, 2013,   from   http://www.telecomcircle.com/2009/06/introduction-to-lbs/#ixzz2KH1rMK2o.

Thomas, J. (2011). "Infographic: The Geosocial Universe."   Retrieved February 2013, 2013, from http://jess3.com/geosocial-universe-2/.

Titterton, D. H. and J. L. Weston (2004). Strapdown Inertial Navigation Technology. , Institution of Engineering and Technology.

Vasconcelos, J. F., G. Elkaim, C. Silvestre, P. Oliveira and B. Cardeira (2011). "Geometric Approach to Strapdown Magnetometer Calibration in Sensor Frame." IEEE Transactions on Aerospace and Electronic Systems **47**(2): 1293-1306.

Wang, H., H. Lenz, A. Szabo, J. Bamberger and U. D. Hanebeck (2007). WLAN-based pedestrian tracking using particle filters and low-cost MEMS sensors. Positioning, Navigation and Communication, 2007. WPNC'07. 4th Workshop on, IEEE**:** 1-7.

Wang, Q., L. Xie, J. Liu and Z. Xiang (2006). "Enhancing particle swarm optimization based particle filter tracker." Computational Intelligence: 1216-1221.

Weinberg, H. (2002). "Using the ADXL202 in pedometer and personal navigation applications." Analog Devices AN-602 application note.

Wieser, M., B. Hofmann-Wellenhof, B. Mayerhofer and B. Pressl (2007). "A navigation concept for visually impaired pedestrians in an urban environment." Österreichische Zeitschrift für Vermessung und Geoinformation, OVG, Wien. Austrian Contributions to the XXIV General Assembly of the International Union of Geodesy and Geophysics **2**.

Xing, Z. and D. Gebre-Egziabher (2008). Modeling and bounding low cost inertial sensor errors. Position, Location and Navigation Symposium, 2008 IEEE/ION, IEEE**:** 1122-1132.

Xue, L., W. Yuan, H. Chang and C. Jiang (2009). MEMS-based multi-sensor integrated attitude estimation technology for MAV applications. Nano/Micro Engineered and Molecular Systems, 2009. NEMS 2009. 4th IEEE International Conference on, IEEE**:** 1031-1035.

Yun, X. P. and E. R. Bachmann (2006). "Design, implementation, and experimental results of a quaternion-based Kalman filter for human body motion tracking." Ieee Transactions on Robotics **22**(6): 1216-1227.

Zhang, J., B. Li, A. G. Dempster and C. Rizos (2010). "Evaluation of high sensitivity GPS receivers." Evaluation.